NASA Contractor Report 145213

Measurement of Vortex Velocities Over a Wide Range of Vortex Age, Downstream Distance and Free Stream Velocity

James B. Rorke
and
Robert C. Moffett

Sikorsky Aircraft Division
United Technologies Corporation
Stratford, Connecticut

Prepared for
National Aeronautics and Space Administration
Washington, D.C.

National Aeronautics and Space Administration

Scientific and Technical Information Office

1977

1. Report No.
NASA Contractor Report 145213

2. Government Accession No.

3. Recipient's Catalog No.

4. Title and Subtitle
MEASUREMENT OF VORTEX VELOCITIES OVER A WIDE RANGE OF VORTEX AGE, DOWNSTREAM DISTANCE AND FREE STREAM VELOCITY

5. Report Date
July 1977

6. Performing Organization Code

7. Author(s)
James B. Rorke and Robert C. Moffitt

8. Performing Organization Report No.
SER-50991

9. Performing Organization Name and Address
Sikorsky Aircraft Division
United Technologies Corporation
Stratford, CT 06602

10. Work Unit No.

11. Contract or Grant No.
NAS1-13765

12. Sponsoring Agency Name and Address
National Aeronautics and Space Administration
Washington, DC 20546

13. Type of Report and Period Covered
Contractor Report

14. Sponsoring Agency Code

15. Supplementary Notes

16. Abstract

A wind tunnel test was conducted to obtain vortex velocity signatures over a wide parameter range encompassing the data conditions of several previous researchers while maintaining a common instrumentation and test facility. The generating wing panel was configured with both a revolved airfoil tip shape and a square tip shape and had a semispan aspect ratio of 4.05/1.0 with a 121.9 cm span. Free stream velocity was varied from 6.1 m/sec to 76.2 m/sec and the vortex core velocities were measured at locations 3, 6, 12, 24 and 48 chordlengths downstream of the wing trailing edge, yielding vortex ages up to 2.0 seconds. Wing pitch angles of 6^o, 8^o, 9^o and 12^o were investigated. Detailed surface pressure distributions and wing force measurements were obtained for each wing tip configuration.

Correlation with vortex velocity data taken in previous experiments is good. During the rollup process, vortex core parameters appear to be dependent primarily on vortex age.

Trending in the plateau and decay regions is more complex and the mechanisms appear to be more unstable. In the plateau region, vortex core size increases with increasing vortex age and the scatter of the data is random in nature. Core size also increases with increasing downstream distance, but, in that case, the scatter is structured with higher free stream velocity yielding lower core size. Axial velocity ratio in the core decreases with increasing vortex age. Maximum tangential velocity ratio does not seem to be an independent function of either vortex age or downstream distance. The data suggests a dependency between maximum tangential velocity ratio and axial velocity ratio in the plateau region. This is assumed to be a part of the decay mechanism.

Vortex meander in the wind tunnel increased with both decreasing speed and increasing downstream distance. No significant differences were noted in surface pressure distributions or force measurements due to change in tip shape.

17. Key Words (Suggested by Author(s))
Vortex flow
Vortex scaling
Tip shape
Tip vortex

18. Distribution Statement
Unclassified - Unlimited

19. Security Classif. (of this report)	20. Security Classif. (of this page)	21. No. of Pages	22. Price*
Unclassified	Unclassified	119	$5.50

* For sale by the National Technical Information Service, Springfield, Virginia 22161

Page Intentionally Left Blank

TABLE OF CONTENTS

Measurement of Vortex Velocities Over a Wide Range of Vortex Age, Downstream Distance and Free Stream Velocity

By James B. Rorke and Robert C. Moffitt
Sikorsky Aircraft Division
United Technologies Corporation
Stratford, Connecticut

SUMMARY

A wind tunnel test was conducted to obtain vortex velocity signatures over a wide parameter range encompassing the data conditions of several previous researchers while maintaining a common instrumentation and test facility. The generating wing panel was configured with both a revolved airfoil tip shape and a square tip shape and had a semispan aspect ratio of 4.05/1.0 with a 121.9 cm span. Free stream velocity was varied from 6.1 m/sec to 76.2 m/sec and the vortex core velocities were measured at locations 3, 6, 12, 24 and 48 chordlengths downstream of the wing trailing edge, yielding vortex ages up to 2.0 seconds. Wing pitch angles of 6°, 8°, 9° and 12° were investigated. Detailed surface pressure distributions and wing force measurements were obtained for each wing tip configuration.

Correlation with vortex velocity data taken in previous experiments is good. During the rollup process, vortex core parameters appear to be dependent primarily on vortex age.

Trending in the plateau and decay regions is more complex and the mechanisms appear to be more unstable. In the plateau region, vortex core size increases with increasing vortex age and the scatter of the data is random in nature. Core size also increases with increasing downstream distance but, in that case, the scatter is structured with higher free stream velocity yielding lower core size. Axial velocity ratio in the core decreases with increasing vortex age. Maximum tangential velocity ratio does not seem to be an independent function of either vortex age or downstream distance. The data suggests a dependency between maximum tangential velocity ratio and axial velocity ratio in the plateau region. This is assumed to be a part of the decay mechanism.

Vortex meander in the wind tunnel increased with both decreasing speed and increasing downstream distance. No significant differences were noted in surface pressure distributions or force measurements due to changes in tip shape.

INTRODUCTION

Wing trailing vortices have been the subject of intensive research in recent years by both fixed wing and rotary wing interests. The prime concern of the fixed wing research is the reduction of the wake-turbulence hazard in airport approach patterns by dispersing the rotational energy in the trailing vortex. A summary of recent work in this area can be found in Reference 1. Rotary wing investigators are primarily concerned with the impact of the rotor blade tip vortex on the performance, dynamic and acoustic characteristics of the rotor.

Investigations aimed primarily at the fixed wing problem have concentrated on such aerodynamic schemes as spoilers, vortex generators, trailing drag devices, steady and pulsed mass injection, and span loading variations to reduce rotational energy in the tip vortex. Although a final solution is not yet in hand, the progress that has been made is most encouraging and the program is continuing[1].

Due to the nature of the helicopter rotor, most devices being examined to reduce the impact of trailing vortices on fixed wing operations are not applicable to the rotary wing problem. In hover, significant reductions in rotor efficiency are caused when the proximity of the tip vortex from a preceding rotor blade causes high induced angles of attack near the tip of subsequent blades. In forward flight, rotor performance, airloads and acoustic signature are all adversely affected by blade-vortex interactions. Analytic methods which have been developed to account for the effect of the tip vortex on helicopter forward flight performance, blade airloads and acoustic signature all require a definition of the flow field within the core of the vortex.

The ultimate success of these current research programs requires a detailed understanding of the flow field in the core of a trailing vortex. While the only cost effective way to gain this understanding is through comprehensive wind tunnel tests, techniques for scaling a tip vortex in a wind tunnel are not understood. Scaled parameters, such as peak tangential velocity, core size, etc., are often discussed using such terms as chordlengths downstream, spanlengths downstream or vortex age. Past experiments, ranging from full scale flight tests to small scale, low speed wind tunnel tests, have provided useful information but, no single test has provided enough information to determine the most important scaling parameters. Comparison of test data from separate investigations has been difficult due to differences in wing models, wind tunnels and instrumentation.

The study reported in Reference 2 was designed to investigate the effect of Mach number and Reynolds number on vortex core parameters. To accomplish this, two basic wing models, geometrically similar, with chords of 10.8 cm and 66.1 cm were tested over a wide speed range and vortex core parameters were measured at two downstream locations. The only parameter which yielded a systematic trending of that data was vortex age, and the trending with vortex age was very systematic. Due to the wide range of test conditions, trending with such parameters as distance, chordlengths or spanlengths downstream, Mach number or Reynolds number yielded only a great deal of scatter. The chief limitation of the work reported in Reference 2 is that the maximum age examined was 0.054 seconds.

In an effort to extend and verify the work of Reference 2, the study reported in Reference 3 was undertaken. Using a five hole yaw head pitot probe, Mason and Marchman surveyed the core of a tip vortex trailing from a NACA 0012 wing at angles of attack of 4, 6, and 8 degrees over a range of downstream distances from 2 to 30 chordlength and free stream speeds from approximately 15 to 35 m/sec to produce several predetermined values of vortex age. The end surface of the wing tip was flat in this study as opposed to the revolved airfoil tip used in the Reference 2 study. In general, the results of this test are in good agreement with the trends published in Reference 2 with the exception of one test condition. The peak swirl velocities measured at the highest tunnel speed (≃30.5 m/sec) and the highest angle of attack (8°) in that test were substantially greater than those measured at the same age at lower tunnel speeds. Due to the differences in instrumentation, wind tunnels, wing tip geometry and velocity ranges, it was difficult to ascertain the reason for the lack of agreement in trends at this single test condition.

The present study was designed to measure wing tip vortices over as wide a range of conditions as possible while maintaining a common instrumentation and test facility. The resulting vortex velocity and wing surface pressure data is to be used to establish vortex trending parameters and to serve as a basis of comparison for the data of previous and future investigators.

SYMBOLS

AR	aspect ratio
b	semispan, meters
C_D	drag coefficient, $D/q_\infty Sc$
C_L	lift coefficient $L/q_\infty S$
C_M	pitching moment coefficient, $PM/q_\infty Sc$
C_P	pressure coefficient, $(p_s - p_\infty)/q_\infty$
c	chord, meters
D	drag force, newtons

d_o	diameter of vortex core, meters
L	lift force, newtons
M	Mach number
PM	pitching moment, newton-meters
p_s	local static pressure, newtons/meter^2
p_∞	free stream static pressure, newtons/meter^2
q_∞	free stream dynamic pressure, $\frac{1}{2} \rho V_\infty^2$, newtons/meter^2
R_N	Reynolds number, $V_\infty c/\nu$
S	projected wing lifting area, meters^2
T_o	stagnation temperature, deg Kelvin
t	elapsed time from vortex leaving wing trailing edge, Z/V_∞, seconds
V_z	axial velocity component, positive in Z direction, meters/second
V_θ	tangential velocity component in X-Y plane, meters/second
V_∞	free stream velocity in Z direction, meters/second
X	ordinate normal to wing span, positive in direction of wing lift
Y	ordinate parallel to wing span, positive toward tip
Z	streamwise ordinate, measured from wing trailing edge, positive downstream
α	wing geometric angle of attack, deg
Γ_o	circulation strength at wing centerline
ν	kinematic viscosity, meters^2/sec

LIST OF ILLUSTRATIONS

Figure | Page

Figure		Page

Figure Page

TEST FACILITY

The United Technologies Research Center Large Subsonic Wind Tunnel is a single return, closed throat facility with interchangeable 5.49 m (18 ft) and 2.44 m (8 ft) octagonal test sections (Figure 1). Maximum velocity in the 5.49 m test section, used during this test program, is approximately 90 m/sec (175 knots). Tunnel stagnation temperature was held nearly constant in the 12° C to 20° C range during acquisition of vortex velocity data by means of air exchanger valves. A high speed static data acquisitioning system was used to record model forces, surface pressures and tunnel air properties. This system is capable of sampling 280 pressures or temperatures and transmitting these data to an on-line digital computer. Additionally, total and static pressure, temperature, wing angle, lift drag, pitching moment and rolling moment were sampled and transmitted to the on-line computer. Data transmitted to this on-line were simultaneously recorded on magnetic tape for more complete processing off-line on a larger capacity digital computer.

MODEL DESCRIPTION

The wing panel was fabricated of steel with a 25.4 cm (10.0 inch) chord, 121.9 cm (48 inch) span and a NACA 0012 airfoil section. Two tip caps were fabricated to facilitate investigation of both a revolved airfoil and flat tip surface. 236 static pressure orifices were distributed spanwise and chordwise on the wing's suction and pressure surfaces as shown in Figures 2 and 3 respectively. A windshield with an attached circular ground plane of 183 cm (72 inch) diameter enclosed the wing's support strut, with the wing extending 102.9 cm (40.5 inches) above the ground plane. The resulting semispan aspect ratio was 4.05/1.00.

Aerodynamic force, moment and surface pressure data were acquired with the model mounted on the wind tunnel balance, which was 24 chordlengths upstream of the vortex measurement position. To position the model 3.0, 6.0, 12.0 and 48.0 chordlengths upstream of the vortex measurement location, both the windshield and wing support strut were attached rigidly to the tunnel floor. Guy wires provided an extra degree of rigidity. A typical installation is shown in Figure 4.

INSTRUMENTATION

Force and Surface Pressures

The 236 static pressure orifices on both the upper and lower wing surfaces were connected to five scanivalves controlled by one driving unit. The scanivalve unit was mounted just below the wind tunnel test section. Force and surface pressure distribution data were acquired simultaneously with the wing mounted on the wind tunnel balance.

Velocity Measurement Instrumentation

The velocity data acquisition system consisted of a triaxial hot wire probe mounted on an X-Y traversing mechanism as illustrated in Figure 5. The probe measures the tunnel axial velocity component and the two cross components provided that the total velocity vector remains within a 70° cone symmetric about the tunnel axis. Probe location could be varied ± 38 cm (±15 inches) vertically or horizontally with the traverse mechanism. The control system for the traverse mechanism and the probe support hardware were located in the tunnel control room.

The traverse mechanism was driven with two 1/2 horsepower variable speed D.C. motors which were mounted directly on the traverse frame. With the variable speed drive, the traversing speed could be varied from 3.8 cm/sec (1.5 inches/sec) to .75 cm/sec (.3 inches/sec) with a demonstrated positioning repeatability of ± .03 cm (± .01 inches). Probe position was monitored by two potentiometers geared to the drive mechanism. The output voltage signals from these potentiometers were wired directly to the plotter used to record voltages proportional to on-line axial and tangential velocities as a function of probe position in the vortex. The on-line data for both axial and tangential velocities were recorded simultaneously as a function of probe position utilizing a plotter with two recording pens.

The triaxial hot wire probe was selected as the flow measurement device for this study based on the following attributes.

1. Rapid reponse characteristics allow continuous acquisition of data as the probe is swept through the flow field.

2. All three components of velocity can be measured directly with one probe of relatively small physical dimensions.

3. Axial velocity variations which occur through the core of the vortex do not affect the instrument calibration or measurement of tangential velocity.

4. Motion of the vortex in the wind tunnel or fluctuation of velocity profiles can be easily detected and monitored due to the high response rate.

The triaxial hot wire probe contains three orthogonal wire elements. Each element has a sensitive wire length of approximately 1.25 mm and a diameter of 5 microns. The sensitive wire length is limited by gold plating which covers the end of the wire support prongs and a small segment of the wire end. This plating reduces interference among the three wires, and between the support prongs and the wire, which could be experienced in the skewed flow field.

The probe wires were heated by three constant temperature anemometers. The voltages required to maintain the constant temperatures of the wires, which are a measure of the velocity normal to each wire, were passed through linearizers to a specialized analog computer. This computing circuit transferred the linearized voltages for the three wires from the probe coordinate system, to the wind tunnel coordinates system. These final voltages, along with the position voltage from the traverse mechanism potentiometers, were then used to drive the plotter. A schematic diagram of this instrumentation is shown as Figure 6. The instrumentation setup itself is shown as Figure 7.

As the probe was traversed through the center of each vortex, an on-line plot was obtained of linearized voltages proportional to tangential and axial velocity in the vortex vs probe position in the wind tunnel. The plotted data was continuously monitored for repeatability and significant trending.

TEST PROCEDURE

Probe Calibration

The following procedure was used to develop the linearized calibration for each sensor element of the triaxial probes used during the data acquisition. A 12 point detailed calibration was performed on each wire of the first probe used to establish the character of the non-linear wire response over the test velocity range. These responses were then linearized to within ± 1.3% with the on-line linearizers. Subsequent probe calibrations, required due to damaged probe replacement or performed to minimize signal drift errors were conducted for four velocities within the test range. The reduced scope of these calibrations reflected the fact that they were used only to determine bias with respect to the initial detailed calibration caused by sensor contamination or, in the case of a new probe, manufacturing tolerances. The apparent biases were minimized by adjusting the wire overheat ratios until the wire output signals agreed with the detailed calibration at a free stream velocity of 68.6 meter/sec (225 ft/sec). The magnitude of this final adjustment was in the order of 1.0% of the total signal.

Vortex Velocity Data Acquisition

Vortex location traverses and vortex signature traverse were required to obtain the tangential and axial velocity distributions for each vortex structure surveyed. During these probe sweeps, the wind tunnel air exchanger louvers were continuously adjusted to maintain a constant stagnation temperature in the test section. This eliminates probe calibration shifts due to wire overheat ratio fluctuations which could cause errors in the vortex core location determination.

The core location for a spanwise vortex signature was acquired by moving the probe parallel to the blade span, or in the Y direction, for several predetermined X locations. The X locations for each of the spanwise sweeps was displayed on a digital voltmeter and the X location corresponding to the peak tangential velocity was noted. Having located the center, between two and twelve spanwise traverses were made, depending on the amplitude of the vortex meandering, to obtain the spanwise vortex signature. As indicated by the sample on-line data plots (Figures 8 and 9) sufficient traverses were made to obtain several repeats of the peak tangential velocity with a repeatability of about ± 5%.

The core position for the normal vortex traverses was determined from the spanwise location of the core center noted during the spanwise data sweeps.

The amplitude of the vortex meander encountered at the 24 and 48 chordlength downstream positions precluded a precise core location. In these cases, however, a large number of data sweeps was employed; yielding a high number of vortex encounters which were examined to determine the maximum tangential velocity.

DATA ANALYSIS

Surface Pressures

Surface pressure data were recorded for both the revolved airfoil and the square tip wing at 236 locations on the upper and lower surfaces. The basic wing model had been fabricated for a previous test, but the location of the pressure taps fit the requirements of the present program with the majority of the taps located near the wing tip. Figures 2 and 3 illustrate the location of the pressure taps and the chordwise segments used for analysis.

The purpose of recording pressure data was to detect any differences in vortex rollup, lift or stall characteristics between the square and revolved airfoil tip geometry. Plots of surface pressure coefficient as a function of chordwise location are shown in Figures 10 through 13 for all angles of attack at which vortex velocity data were recorded. In general, the pressure distributions for either tip shape are nearly identical. The only difference occurs at the outermost spanwise station (segment 1) where, near the trailing edge, the pressure on the upper surface of the wing with a revolved airfoil tip shape exhibits a pronounced suction which is not present on the square tip wing. This is best illustrated by the chordwise pressure coefficient plot for segment 1 in Figure 13 for the 12° wing angle, but Figures 10, 11 and 12 show that the difference persists at lower wing angles. This probably indicates that the tip vortex generated by a wing with a revolved airfoil tip shape tends to roll up over a larger portion of the wing surface than a vortex generated by a square tip wing. At an angle of attack of 12°, no stall is evident on either wing tip.

Force Measurements

Aerodynamic forces and moments reduced to coefficient form are presented as a function of angle of attack in Figures 14 and 15. Wing area was identical for both the revolved airfoil and square tip configurations. These data were only acquired at a tunnel speed of 76.2 m/sec (250 ft/sec) to maintain a high degree of data accuracy.

No significant differences in lift, drag or pitching moment characteristics were observed between the two tip shapes. The lift curve slopes for both configurations were equal at $dC_L/d\alpha$ = 4.58/radian. Maximum lift coefficient was 1.09 for the revolved airfoil tip and 1.11 for the square tip configuration with the peak lift occurring at 15 degrees angle of attack for each. Both tip shapes display similar drag curves with a minimum drag coefficient of about .0085. The pitching moment curves show a positive slope for both configurations to stall (about 15 degrees) where a sharp negative gradient is established.

The spanwise center of lift on the wing is presented as a function of angle of attack in Figure 16 for the revolved airfoil and square tip shapes. Comparison of these two figures indicates that the center of lift on the wing with a revolved airfoil tip shape is consistently slightly inboard of the center of lift for the square tip configuration. The following table summarizes the comparison of force data for the two tip shapes:

	Revolved Tip	Square Tip
C_{Lmax}	1.09	1.11
Spanwise Center of Lift	more inboard	outboard
$dC_{L/d\alpha}$, $C_{d_{min}}$, etc.	equal	equal

It should be noted that, although the difference in spanwise center of lift is consistent with the force data discussed above, it is inconsistent with the surface pressure data which showed an increase in negative pressure on the upper surface, at the outboard trailing edge of the revolved airfoil configuration. The conclusion must therefore be drawn that additional small differences exist in the surface pressures of the two configurations that slightly offset the difference apparent at the trailing edge of the outboard segment 1 in Figures 10, 11, 12 and 13.

Vortex Velocity Data Corrections

The on-line vortex velocity profiles recorded directly from the anemometer instrumentation required a number of analytic corrections due to the operating characteristics of a hot wire probe. These included: (1) corrections for shifts in the static pressure and stagnation temperature encountered during the data runs and those experienced during probe calibration; and (2) correction of residual non-linearity remaining in the probe signal after passage through the on-line linearizers.

These corrections were applied in accordance with the procedures established in Reference 2. This method uses a semi-empirical heat transfer equation as a base which has been shown to be valid over a free stream Mach number from .05 to 1.9. Partial differentiation of the velocity term in this equation with respect to the stagnation temperature, static pressure, and Mach number respectively yielded error expressions. These were used to correct the velocity data for differences between the ambient test conditions and the probe calibration conditions.

The magnitude of the radial static pressure gradient within each surveyed vortex structure was evaluated by integrating the radial component of the Navier-Stokes equation with an assumed constant density. The validity of this approach for estimating swirl induced pressure distributions in axisymmetric flow has been demonstrated [4, 5]. No corrections were applied for stagnation temperature changes in the vortex since resistance thermometer sweeps through several vortex flow fields showed only insignificant temperature variations in a previous study.[2]

The linearization corrections were required since the on-line axis transfer circuits assume that the voltage inputs from the three sensor wires are linear and identically matched. In practice, perfect signal linearization and matching is impossible and small errors in the degree of approximation can cause significant errors in the indicated vortex velocities. A procedure was incorporated in the data reduction analysis which calculated the voltage sensed by each wire from the on-line velocity profiles, corrected the velocity components normal to each wire for the known nonlinearities, and then reconstructed the vortex velocities. This procedure is detailed in Appendix A of Reference 2.

The complete data analysis routine was programmed for a digital computer. The program input for each case consisted of the digitized on-line points, calibration conditions, and ambient data point conditions. The program output presents a tabular listing of the vortex velocity, vorticity, and circulation distributions in addition to plots of the corrected velocity distributions.

Vortex Stability

The vortex structures generated in the 5.5m (18 ft.)test section exhibited trajectory meander for all test conditions. This contrasts with the data obtained in the previous investigation[2] which showed no indication of vortex instability.

Although the vortex meander was apparent at all data conditions investigated in the current study, the magnitude of the instability was small for Z/c survey locations of 3 and 6 chordlengths. As the downstream position was increased beyond 6 chordlengths, the meander magnitude increased rapidly. The intensity of the vortex trajectory meander was also affected by the free stream velocity. Data acquired at a constant downstream location indicated a consistent increase in the meander amplitude as the free stream velocity was decreased from 76.2 meters/sec (250 ft/sec) to 6.1 meters/sec (20 ft/sec).

Figure 8 presents sample on-line traces of vortex signatures from the square tip wing which illustrate the effects on the vortex meander amplitudes of downstream distance at a constant free stream velocity of 20.6 meters/sec (62.4 ft/sec). Figure 9 represents data acquired at 24 chordlengths downstream at various speeds. Both sets of data were obtained with the square tip installed on the model. As indicated in the figures, the number of traverses through the vortex structures was increased as the meandering intensified in order to increase the accuracy of the peak tangential velocity measurement.

A correlation between vortex meandering amplitude and elapsed time after vortex formation is indicated by the direct intensification of the meander with increasing downstream distance and the inverse trend with free stream velocity. $t = Z/V_\infty$.

Vortex Trending Parameters

Presently, the two most widely used trending parameters for tip vortex parameters are nondimensionalized downstream distance ($Z/_c$) and vortex age. Other more general parameters have been published in an effort to correlate data from several separate sources.

References 6 and 7 present data from a wide variety of sources plotted as dimensionless maximum tangential velocity vs dimensionless downstream distance or, in the notation of this report, from Reference 7,

$$2\ V_\theta\ b/(\Gamma_0 AR)\ \text{vs}\ \frac{Z}{b}\,\frac{\Gamma_o}{2\ V_\infty b}\,(AR)^2\ f\,\frac{(\Gamma_o)}{\nu}.$$

Although these parameters collapse the data from the various sources reasonably well, the scatter in the nondimensional tangential velocity is still a factor of two at constant dimensionless downstream distance. This scatter is probably affected by such unaddressed parameters as planform shape and tip configuration. The present report, for instance, explores differences existing in tip vortices trailing from wings with a revolved airfoil tip shape as opposed to a square tip shape.

In the data from the present test, all parameters in the function introduced above are constant except Γ_o, V_θ, V_∞ and downstream distance. For the sake of simplicity, only the latter four parameters were considered in the data analysis. Normalizing by mid span circulation (or lift coefficient) did tend to collapse the data for different wing angles but, for the sake of clarity, data for separate angles are presented separately.

For each data point, vortex velocity data were recorded during probe traverses both parallel and normal to the wing span. The measured core sizes, tangential velocities and axial velocities for the two traverse have been averaged for each data point. These parameters were then nondimensionalized and plotted as a function of both vortex age and downstream distance as discussed below. All vortex velocity data are tabulated in Table I.

It should be noted that the majority of the data measured were in or very close to the plateau region where rates of change of vortex core parameters are expected to be small. The onset of vortex decay is not expected to be a simple phenomena but more analagous to the transition from laminar to turbulent flow. The size of the scatter bands therefore should not surprise the reader.

Vortex Core Size

Figures 17 through 24 present vortex core diameter, nondimensionalized by wing chord, as a function of both nondimensionalized downstream distance and vortex age for each wing angle. The vortex meander problem precluded a precise definition of the vortex core at the larger values of $Z/_c$ but, considering the meander problem, the data are quite consistent.

Both the age and distance plots seem to show consistent trends. Close examination of the $Z/_c$ plots reveals that where data are available at downstream distances of 24 chordlengths or more, the data is structured with higher free stream velocity yielding smaller core diameters at constant $Z/_c$. Figures 18 and 22 best illustrate this trend. This suggests either that age is the predominant factor or that there is a "speed effect" as suggested by Marshal and Marchman[3]. The vortex age plots seem to yield a more concise trend with the scatter of the data more random in nature.

Vortex Core Axial Velocity

The minimum axial velocity measured in the core of the vortex nondimensionalized by free stream velocity is presented in Figures 25 through 32. As in the case of the core diameter, when normalized axial velocity is plotted as a function of $Z/_c$ the scatter of the data for either wing tip is structured with low tunnel speeds (higher ages) yielding lower axial velocity ratios. This structuring indicates an age or speed function.

The plot of axial velocity ratio as a function of vortex age generally yields a systematic trend of decreasing axial velocity in the core as a function of increasing time. In addition, it can be seen that the slope of this decay curve increaes with increasing wing angle.

The large degree of scatter in the age trending of axial vortex velocities measured for the revolved tip shape is unexplained. It was noted during the test program that vortex meander seemed to be more pronounced for the revolved airfoil wing tip.

Vortex Tangential Velocity

The measured peak nondimensional tangential velocities, (V_θ/V_∞) max, are plotted in Figures 33 through 40 against the nondimensionalized downstream position, $(Z/_c)$, and vortex age (t). For clarity, the $Z/_c$ trend plot and the time trend plot for a particular tip configuration and a constant wing pitch angle are presented on adjacent facing pages.

As indicated by the figures, neither $Z/_c$ nor t produced a complete collapse of the measured tangential velocities. When plotted on a $Z/_c$ base, the nondimensionalized tangential velocities exhibit a maximum scatter of $\pm$ .05 (V_θ/V_∞) for $Z/_c$ less than 12 and $\pm$ .1 $\frac{(V_\theta)}{V_\infty}$ for $Z/_c$ locations of 24 and 48 chordlengths. The age based tangential velocity plots produced still higher data scatter with a maximum scatter band of $\pm$ .05 $\frac{(V_\theta)}{V_\infty}$ occurring for 9° angle of attack revolved tip vortex structures. In general, the age based plots increased the data scatter relative to the $Z/_c$ plot for all angles of attack tested with both the square and revolved tip configurations. A review of the tangential velocity data contained in the figures indicates that the scatter present in the $Z/_c$ and the vortex age trending plots is not completely random.

For the data plotted as a function of $Z/_c$, an effect of free stream velocity on the nondimensionalized tangential velocities is present at 24 and 48 chordlengths downstream. The measured data indicates that, at these axial positions, the nondimensional vortex tangential velocities are consistently higher for the lower tunnel speed conditions. At downstream survey positions of 3, 6, and 12 chordlengths the trend is less pronounced, and it appears that the free stream velocity effect is amplified as the tip vortex moves away from the generating wing.

Although a free stream velocity trend is not apparent in the plots of nondimensional tangential velocity as a function of vortex age, these plots do indicate a trend with axial survey position. Specifically, as illustrated in Figure 35 for the square tip at 8° pitch, reasonable but different trend lines can be faired through the data obtained at each $Z/_c$.

This type of data scatter behavior can also be seen for the remaining seven test configurations. It should also be noted that the clarity of the constant $Z/_c$ data separation does not diminish in the 24 to 48 chord-lengths survey positions despite the vortex meander problem which made accurate data acquisition difficult.

Both the presence of considerable scatter in the trend plots of $\frac{V_\theta}{V_\infty}$ with $Z/_c$ and vortex age, and the fact that the scatter is not random indicates that neither $Z/_c$ nor vortex age completely determine the vortex peak tangential velocity in the plateau region for a given wing configuration and pitch angle. Although it is possible that $Z/_c$ and vortex age interact in a manner that permits an unknown combination of these parameters to define the tangential flow field, it is more likely that additional parameters which have not been considered enter into the problem. A list of likely candidates would include the free stream turbulence level, the vortex core axial flow characteristics, Reynolds number effects at extremely low free stream velocities, and vortex stability characteristics.

Summary of Vortex Velocity Data Trends

The following table summarizes the trends discussed above for vortex core size, axial velocity ratio and tangential velocity ratio as a function of both vortex age and nondimensionalized downstream distance. These general trends apply to both the revolved and square tip wing. Exceptions to these trends can be found in may cases due to data scatter.

PARAMETER	VORTEX AGE	DOWNSTREAM DISTANCE
$d_{o/c}$	SCATTER RANDOM $d_{o/c}$ increases with increasing age no subtrend	SCATTER STRUCTURED $d_{o/c}$ increases with increasing $Z/_c$ $d_{o/c}$ increases with decreasing V_∞
V_z/V_∞	SCATTER STRUCTURED V_z/V_∞ decreases with increasing age V_z/V_∞ increases with increasing $Z/_c$ at constant age	SCATTER STRUCTURED no definite trend of V_z/V_∞ vs $Z/_c$ V_z/V_∞ increases with increasing V_∞ at constant $Z/_c$

	VORTEX AGE	DOWNSTREAM DISTANCE
$(V_\theta/V_\infty)_{max}$	SCATTER STRUCTURED V_θ/V_∞ decreases with increasing age V_θ/V_∞ increases with decreasing $Z/_c$ at constant t.	SCATTER STRUCTURED V_θ/V_∞ increases with decreasing $Z/_c$ V_θ/V_∞ increases with decreasing V_∞ at constant $Z/_c$

The nondimensionalized vortex core axial velocity (V_Z/V_∞) trends presented in Figures 25 through 32 appear to be strongly related to the trends for peak vortex tangential velocities. The ($Z/_c$) based trending plots of V_Z/V_∞) exhibit a free stream velocity effect which is opposite to the observed effect of the free stream velocity on the nondimensional peak tangential velocity. While the highest normalized tangential velocities were measured at the lowest free stream test velocities, the lowest normalized core axial velocities were measured at the low speed test condition.

These opposing effects on the vortex core axial flow velocity and the strength of the vortex tangential flow tend to suggest that a mechanism is present through which linear momentum is tranferred to angular momentum in the core flow field. A coupling between the two flow fields is not a new idea and has been demonstrated in the Reference 8 vortex stability study and the vortex core mass injection studies reported in References 9 and 10. The mass injection experiments indicated that the addition of secondary high velocity flow into the vortex core tended to diffuse the peak swirl velocities in a manner which is analogous to the trends observed in the current test data. Although the cause of the axial flow rate alterations measured in this study are currently not understood, the effect on the peak tangential velocities appears to be similar to those obtained in Reference 9 when the core axial velocity was altered by external means.

A possibility exists that the axial core velocity behavior and ultimately the resulting peak tangential velocities are related to the tendancy of the tip vortex structure to meander as large downstream axial displacements, or elapsed times after vortex formation, are encountered. As noted previously the tendency for vortex meander increased markedly as the vortex moved downstream and aged. This behavior paralleled the decrease of the axial flow in the vortex core. Unfortunately, since the exact mechanism of vortex meander in a wind tunnel is not currently explainable, the flow processes through which the vortex meander instability might affect axial flow in the vortex core cannot be evaluated. It should be noted, however, that data obtained in the Reference 2 vortex test which was conducted at short downstream survey positions of 2 to 5 chord-lengths and appreciably higher free stream velocities (Mach .2 to Mach .6) showed no evidence of either vortex meander or large axial flow deficits in the core region. The primary differences between the Reference 2 test and the current study are that, in the current study, the maximum tunnel speed was decreased by a factor of three, maximum downstream distance was increased by a factor of eight and, because of the lower speed, turbulence levels were increased.

COMPARISON WITH PREVIOUS RESULTS

Peak Tangential Velocity

Peak nondimensional tangential velocities measured during the vortex core study of Reference 2 are compared with data fairings of the current experimental results in Figures 41 and 42. Comparative results are presented in terms of both $Z/_c$ and vortex age trending for data obtained at 6^o and 9^o wing pitch angle. Although both test models employed revolved airfoil tip configurations, the 2.1:1:0 aspect ratio of the earlier wing model was considerably less than the 4.0:1:0 model used in the current program. Fairings of the current experimental data, presented earlier in this report as discreet points, are shown as bands.

The peak tangential velocity ratios obtained in the earlier study and presented in the comparisons do not correspond to the values indicated in Figure 12 of the previous report[2] because the mean of the normal and spanwise traverse results have been substituted for the spanwise traverse peak tangential velocities which were reported in Reference 2. These data were initially interpreted only in terms of the spanwise results since the close survey positions (2 and 5 chordlengths aft of the trailing edge) introduced considerable assymetry in the vortex structures which yielded different velocity distributions for normal and spanwise traverses. For comparison with the data obtained in this program, the spanwise and normal survey results have been averaged.

In general, the vortex age trending parameter yields better correlation between peak tangential velocity ratios measured in the current studies and those determined earlier at the high Mach numbers. This trend is particularly evident at the 9^o wing pitch conditions, illustrated in Figure 42, where the high Mach number data identifies the vortex rollup phase at low elapsed times and then fairs into the new data obtained at the lower tunnel velocities. Vortex age based correlation between the two data sets at 6^o pitch (Figure 41) is less pronounced, although the data consistency is still stronger than that realized with $Z/_c$ trending.

The combined peak tangential velocity ratio data obtained in the two studies suggest that vortex age may be the dominant influence on the vortex structure in the region immediately behind the generating wing panel where the viscous rollup forces govern the flow process. As previously noted, the data also suggest that at larger elapsed times, or larger downstream distances, additional parameters such as core axial flow rates may enter the picture and exert considerable influence on the tangential flow structure. It should be noted that mean fairings through the nondimensional tangential velocities measured for the square tip wing model compare favorably with those measured in Reference 3. An exception, however, occurred at the highest tunnel speed (30.5 m/secs) for which data was obtained at 8^{o} wing angle in the Reference 3 study. Nondimensional velocities measured at this condition were considerably higher than both those measured at lower tunnel speeds in the same study and those measured at all speeds in the current investigation. No explanation for the discrepancy at that one test condition could be found in the results of the current program. The trend of peak tangential velocity ratio with free stream velocity at constant $Z/_c$ derived from the current study is opposite to that indicated by the single test condition of Reference 3.

Vortex Core Size

Experimental nondimensional vortex core diameters(d_o/c) obtained in the current study and the Reference 2 program are compared in Figures 43 and 44. Results for the current study are presented as scatter bands to reflect the questionable measurement accuracy at high vortex ages and large downstream survey positions where vortex meander was significant.

As indicated by the figures, the vortex age trending yields substantially better correlation between the two experimental data sets than $Z/_c$ trending. This improvement is apparent in both the 6^{o} wing pitch data presented in Figure 43 and the 9^{o} wing pitch data shown in Figure 44. For both wing angles, vortex age trending of the combined data sets identifies a vortex rollup region which extends for approximately .05 seconds after the vortex leaves the wing trailing edge. During this formation period, the vortex core contracts as vorticity from the trailing sheet is entrained in the tip vortex structure. At larger elapsed times, this trend is reversed and the core size expands as a result of viscous shear.

The overlap between the data of the current study and of Reference 2 occurs in the juncture region between the core contraction and expansion stage. Only small core size discrepancies are apparent between the two groups of data in this region despite the vortex meander tendency which was encountered in the current program.

It should be noted that the trends of core size with free stream velocity found in the data presented in Figures 43 and 44 of Reference 2 are opposite to those found in the data of the current study. This structuring identified in the Reference 2 data, is based on very few data points. All structuring of the Reference 2 data disappears when those data are plotted as a function of vortex age. All of the Reference 2 data were acquired in the rollup region while the structuring of data from the current study occurs in or at the end of the plateau region. For these reasons, no particular significance should be attached to the structuring of the Reference 2 core size data when it is plotted as a function of $Z/_c$.

CONCLUSIONS

1. While vortex core parameters appear to be dependent primarily on vortex age during the rollup process, trending in the plateau and decay regions is much more complex.

2. The rate of change of vortex core parameters in the plateau region is often so small that trends may become masked by data scatter.

3. The data suggest a strong dependency between maximum tangential velocity ratio and axial velocity ratio in the plateau region.

4. In the plateau region, vortex core size increases with increasing vortex age.

5. In the plateau region, axial velocity ratio decreases with increasing vortex age.

6. In the plateau region, peak tangential velocity ratio decreases with increasing vortex age, but is also a function of downstream distance.

7. Trending either d_o/c or V_z/V_∞ with Z/c resulted in a subtrend with V_∞.

8. No significant differences were noted in surface pressure distributions or force data obtained with either the square tip or the revolved airfoil tip.

REFERENCES

1. Proceedings of the NASA Symposium on Wake-Vortex Minimization. (Washington, D.C.), February 1976.

2. Rorke, J. B.; and Moffitt, R.C.: Wind Tunnel Simulation of Full Scale Vortices. NASA CR 2180, March 1973.

3. Marshall, J. R.; and Marchman, J. F. III: Vortex Age as a Wake Turbulence Scaling Parameter. NASA CR 132312, August 1973. (Also available as Report VPI-AERO-0006, Virginia Polytechnic Institute and State University, Blacksburg, Virginia.

4. Chigier, N. A.: Velocity Measurements in Vortex Flows. Paper presented at the ASME Fluids Engineering Division Conference (Pittsburgh, Pennsylvania), May 11, 1971.

5. Newman, B. G.: Flow in a Viscous Trailing Vortex. Aeron. Quart., Vol. 10, February - November 1959, pp 149-162.

6. Ciffone, D. L.; and Orloff, K. L.: Application of Laser Velocimetry to Aircraft Wake-Vortex Measurements. Proceedings of NASA Symposium on Wake-Vortex Minimization (Washington, D.C.), February 25-26, 1976.

7. Inverson, James D.: Correlation of Turbulent Trailing Vortex Decay Data. AIAA J. Aircraft, Vol. 13, No. 5, May 1976.

8. Logan, A. H.: A Solution to the Vortex Breakdown Phenomenon in a Trailing Line Vortex. M.S. Thesis, Pa. State U., 1966.

9. Rinehart, S.A.; Balcerak, J. C.; and White, R. P., Jr.: An Experimental Study of Tip Vortex Modification By Mass Flow Injection. RASA Report 71-01, Rochester Applied Science Associates, Rochester, N.Y., January 1971.

10. White, R. P., Jr.; and Balcerak, J. C.: An Investigation of the Mixing of Linear and Swirling Flows. Rochester Applied Science Associates, Rochester, N.Y., February 1972.

TABLE I

TABULATED VORTEX DATA $\alpha = 6^{o}$, Square Tip

V_{∞} (m/sec)	Z/c	t (sec)	R_N x10^{-6}	$(V_{\theta}/V_{\infty})_{max}$	(d_o/c)	$(V_z/V_{\infty})_{min}$
75.7	3.0	.0100	1.273	.404	.073	.86
50.6		.0151	.859	.425	.068	.91
38.3		.0199	.670	.447	.063	.865
18.6		.0410	.330	.393	.082	.81
9.4		.0807	.167	.393	.071	.80
75.7	6.0	.0201	1.286	.353	.075	.93
50.9		.0300	.872	.386	.070	.92
38.3		.0398	.664	.380	.070	.91
18.7		.0815	.330	.386	.072	.83
9.6		.1592	.171	.400	.102	.79
76.2	12.0	.0400	1.262	.314	.082	.95
51.3		.0595	.851	.356	.083	.92
38.0		.0801	.638	.364	.073	.95
19.3		.1590	.326	.392	.089	.87
9.8		.3130	.167	.380	.121	.81
76.2	24.0	.0800	1.247	.287	.129	.91
37.7		.1618	.638	.320	.144	.88
18.6		.3284	.319	.322	.150	.91
12.4		.4920	.219	.366	.168	.76
9.6		.637	.169	.374	.172	.72
76.1	48.6	.1618	1.295	.254	--	.95
38.3		.3227	.671	.303	--	.91
19.0		.6495	.342	.272	--	.84
11.9		1.043	.215	.342	--	.84
9.1		1.351	.169	.323	--	.77
6.1		2.025	.116	.335	--	.67

TABLE I (cont.) $\alpha = 6^{o}$, Revolved Tip

V_∞	Z/c	t	R_N x10^{-6}	$(V_\theta/V_\infty)_{max}$	(d_o/c)	$(V_z/V_\infty)_{min}$
75.9	3.0	.0100	1.275	.436	.070	.91
50.7		.0150	.866	.445	.060	.95
38.3		.0199	.667	.488	.070	.91
18.8		.0400	.329	.486	.066	.87
9.6		.0798	.167	.470	.077	.74
75.7	6.0	.0201	1.287	.396	.077	.91
51.0		.0299	.876	.379	.061	.89
38.4		.0397	.665	.409	.067	.88
18.7		.0814	.330	.450	.067	.69
9.7		.1577	.172	.447	.073	.63
76.3	12.0	.0400	1.265	.324	.107	.87
76.2		.0400	1.263	.324	.078	.93
51.7		.0590	.863	.342	.056	.87
38.1		.0800	.644	.391	.078	.86
19.1		.1596	.328	.422	.068	.75
9.5		.3212	.164	.404	.093	.67
76.4	24.0	.0798	1.235	.269	--	.87
37.8		.1611	.635	.280	--	.86
18.8		.3236	.320	.294	--	.85
12.6		.4854	.215	.348	--	.73
9.7		.6270	.167	.359	--	.69
75.7	48.6	.163	1.286	.228	--	.94
38.1		.3237	.664	.299	--	.90
19.2		.644	.343	.281	--	.83
12.5		.986	.228	.361	--	.73
10.0		1.233	.184	.342	--	.72
6.1		2.025	.122	.332	--	.65

TABLE I (cont.) $\alpha = 8^{\circ}$, Square Tip

V_∞	Z/c	t	$R_N \times 10^{-6}$	$(V_\theta/V_\infty)_{max}$	(d_o/c)	$(V_z/V_\infty)_{min}$
75.6	3.0	.0101	1.265	.459	.093	1.16
50.8		.0150	.867	.498	.089	1.26
37.9		.0202	.660	.506	.081	1.05
18.7		.0406	.329	.461	.089	.89
9.6		.0793	.169	.451	.094	.81
75.7	6.0	.0201	1.287	.43	.120	1.11
51.1		.0298	.876	.487	.091	1.19
38.2		.0399	.663	.498	.072	1.00
19.0		.0800	.340	.485	.090	.86
9.9		.1534	.180	.506	.112	.83
76.0	12.0	.0401	1.279	.415	.111	.92
50.6		.0602	.859	.477	.091	1.00
38.0		.0803	.652	.519	.102	1.01
19.0		.1605	.332	.498	.101	.89
9.5		.3215	.167	.494	.111	.90
76.1	24.0	.0801	1.246	.364	.112	.88
37.6		.1620	.639	.403	--	.90
18.7		.3260	.324	.438	--	.89
12.3		.4958	.216	.447	--	.77
9.6		.6369	.169	.453	--	.74
75.7	48.6	.1635	1.270	.308	--	.94
38.4		.3213	.662	.423	--	.93
19.5		.6334	.350	.382	--	.88
11.6		1.04	.218	.439	--	.82
8.7		1.422	.160	.435	--	.80
6.1		2.025	.114	.402	--	.61

TABLE I (cont.) $\alpha = 8^{\circ}$, Revolved Tip

V_∞	Z/c	t	$R_N \times 10^{-6}$	$(V_\theta/V_\infty)_{max}$	(d_o/c)	$(V_z/V_\infty)_{min}$
76.0	3.0	.0100	1.274	.513	.093	.87
50.8		.0150	.864	.508	.076	.68
38.0		.0200	.655	.537	.094	.83
18.8		.0405	.329	.556	.070	.76
9.6		.0792	.169	.500	.075	.67
76.2	6.0	.0200	1.276	.481	.091	.75
50.7		.0300	.871	.518	.081	.59
38.2		.0399	.666	.551	.068	.71
19.0		.0803	.337	.477	.077	.67
9.7		.1567	.175	.493	.085	.60
76.0	12.0	.0401	1.282	.442	.085	.74
50.6		.0602	.858	.524	.089	.58
38.0		.0802	.651	.536	.085	.54
19.2		.1589	.334	.541	.086	.56
9.7		.3135	.171	.498	.105	.50
76.4	24.0	.0798	1.234	.318	--	.81
37.8		.1612	.637	.368	--	.78
18.9		.3226	.322	.323	--	.77
12.5		.4891	.213	.402	--	.72
9.8		.6222	.168	.435	--	.51
76.7	48.6	.161	1.300	.28	--	.91
38.3		.3222	.669	.382	--	.86
18.9		.6517	.341	.302	--	.79
12.3		1.006	.223	.454	--	.53
9.9		1.246	.182	.450	--	.72
6.1		2.025	.108	.421	--	.48

TABLE I (cont.) $\alpha = 9^{o}$, Square Tip

V_∞	Z/c	t	R_N $\times 10^{-6}$	$(V_\theta/V_\infty)_{max}$	(d_o/c)	$(V_z/V_\infty)_{min}$
75.1	3.0	.0101	1.260	.505	.109	1.07
38.2		.0200	.656	.547	.095	1.06
50.9		.0150	.861	.556	.092	1.05
18.9		.0403	.327	.523	.101	1.01
9.6		.0796	.168	.506	.111	.88
76.1	6.0	.0200	1.282	.482	.105	1.05
51.0		.0300	.864	.530	.102	1.07
38.4		.0397	.662	.541	.098	1.18
19.0		.0801	.334	.533	.085	1.13
9.8		.1554	.173	.485	.104	.85
75.9	12.0	.0402	1.290	.469	.087	1.09
50.6		.0603	.865	.528	.108	1.15
37.8		.0806	.656	.545	.092	.88
18.9		.1610	.333	.535	.104	.91
9.5		.3205	.169	.502	.116	.78
76.1	24.0	.0801	1.247	.393	.142	.87
37.6		.1620	.638	.423	.120	.90
19.1		.3192	.332	.314	.141	.89
12.1		.5014	.211	.460	.138	.81
9.6		.6359	.169	.474	.128	.73
76.3	48.6	.1618	1.287	.291	--	.965
38.4		.3213	.663	.411	--	.940
19.1		.644	.339	.310	--	.87
12.2		1.014	.217	.439	--	.82
9.0		1.38	.161	.45	--	.76
6.1		2.025	.127	.435	--	.73

TABLE I (cont.) $\alpha = 9^{o}$, Revolved Tip

V_∞	Z/c	t	R_N X 10^{-6}	$(V_\theta/V_\infty)_{max}$	(d_o/c)	$(V_z/V_\infty)_{min}$
76.2	3.0	.0100	1.283	.525	.099	.45
51.1		.0149	.871	.569	.090	.38
38.2		.0201	.652	.609	.083	.51
18.8		.0405	.329	.633	.060	.94
9.5		.0805	.168	.532	.088	.62
76.0	6.0	.0200	1.279	.474	.087	.56
50.8		.0300	.872	.526	.090	.40
38.6		.0397	.668	.552	.082	.40
19.1		.0799	.335	.550	.073	.58
9.6		.1587	.170	.500	.086	.41
75.9	12.0	.0401	1.293	.473	.112	.69
50.5		.0603	.867	.536	.091	.50
37.9		.0804	.660	.540	.091	.44
19.1		.1595	.336	.560	.098	.53
9.1		.3333	.162	.513	.133	.42
76.2	24.0	.0800	1.239	.375	.134	.67
37.9		.1610	.637	.427	.156	.74
19.0		.3205	.323	.356	.141	.75
12.4		.4902	.214	.485	.202	.60
9.5		.6410	.163	.456	.208	.55
76.4	48.6	.1615	1.292	.25	.174	.94
37.8		.3267	.656	.317	.174	.90
18.9		.6544	.335	.284	.229	.89
11.8		1.047	.212	.391	.207	.80
9.4		1.308	.171	.411	.240	.66
6.1		2.025	.112	.436	.265	.42

TABLE I (cont.) $\alpha = 12^\circ$, Square Tip

V_∞	Z/c	t	R_N x10^{-6}	$(V_\theta/V_\infty)_{max}$	(d_o/c)	$(V_z/V_\infty)_{min}$
38.1	3.0	.0200	.656	.618	.077	1.20
38.1	6.0	.0400	.654	.614	.088	1.15
37.8	12.0	.0806	.660	.641	.102	1.29
76.0	24.0	.0802	1.247	.514	.137	.91
37.6		.1623	.635	.552	--	.84
19.0		.3216	.330	.357	--	.79
11.9		.5141	.204	.580	--	.67
11.8		.5150	.205	.510	--	.73
9.5		.6420	.167	.535	--	.70
6.1		.990	.110	.567	--	.52
76.5	48.6	.1613	1.278	.455	--	.90
38.2		.3245	.652	.449	--	.86
18.7		.654	.332	.440	--	.68
12.1		1.017	.218	.444	--	.66
10.0		1.240	.180	.548	--	.55
6.1		2.025	.112	.514	--	.51

$\alpha = 12^\circ$, Revolved Tip

V_∞	Z/c	t	R_N x10^{-6}	$(V_\theta/V_\infty)_{max}$	(d_o/c)	$(V_z/V_\infty)_{min}$
38.0	3.0	.0200	.658	.606	.121	.34
38.2	6.0	.0400	.655	.592	.134	.26
37.9	12.0	.0803	.656	.611	.143	.31
76.3	24.0	.0799	1.231	.474	.165	.59
37.9		.1607	.636	.514	.202	.56
19.3		.3158	.327	.388	--	.434
12.5		.4884	.214	.535	--	.52
9.7		.6320	.167	.557	--	.34
6.1		.958	.110	.560	--	.47
76.3	48.6	.1618	1.275	.424	--	.77
38.7		.3187	.672	.481	--	.66
19.0		.6511	.339	.437	--	.60
12.2		1.012	.219	.425	--	.69
9.5		1.300	.170	.496	--	.63
6.1		2.025	.107	.504	--	.45

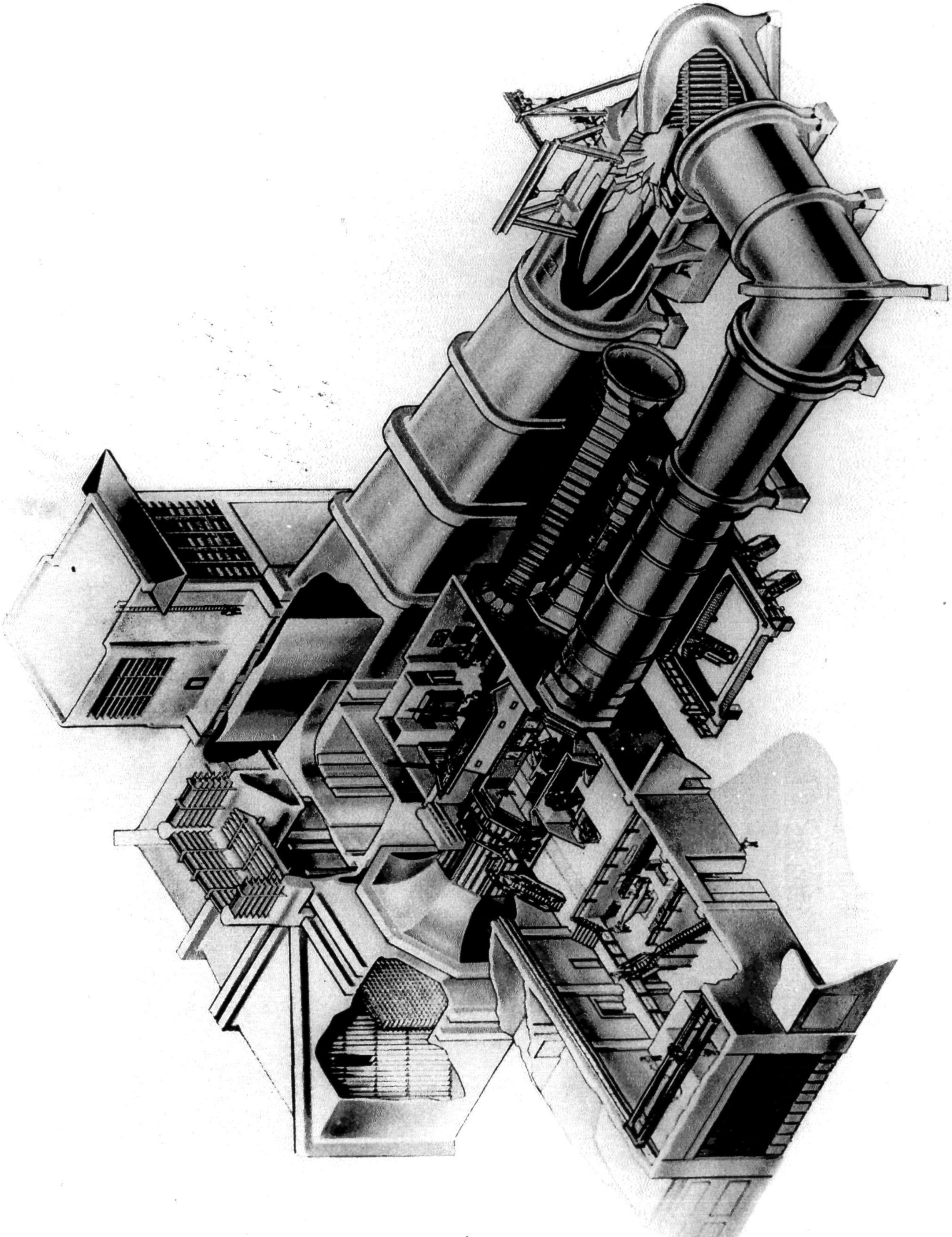

P6 29 90%

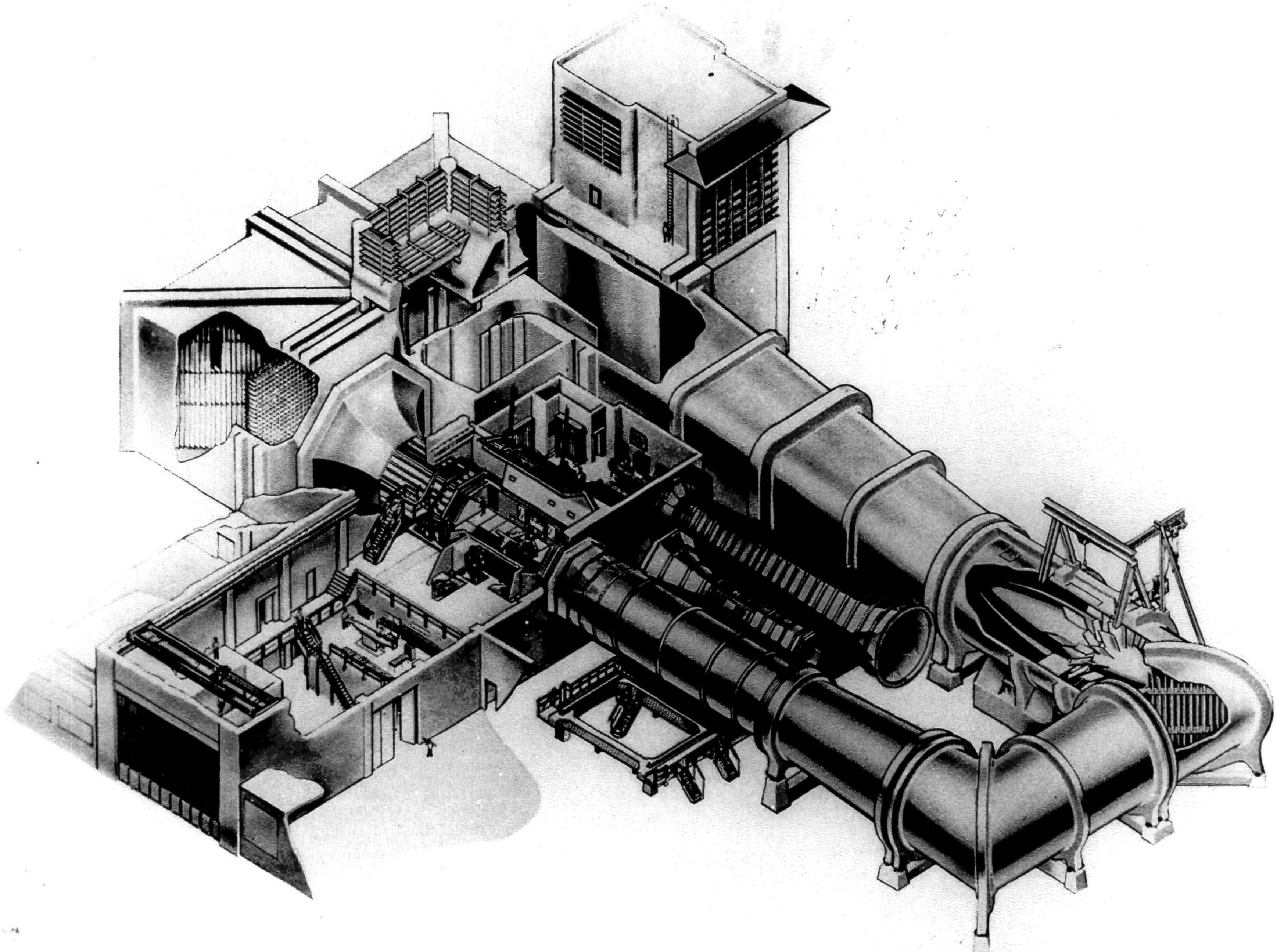

Figure 1. UTRC Large Subsonic Wind Tunnel.

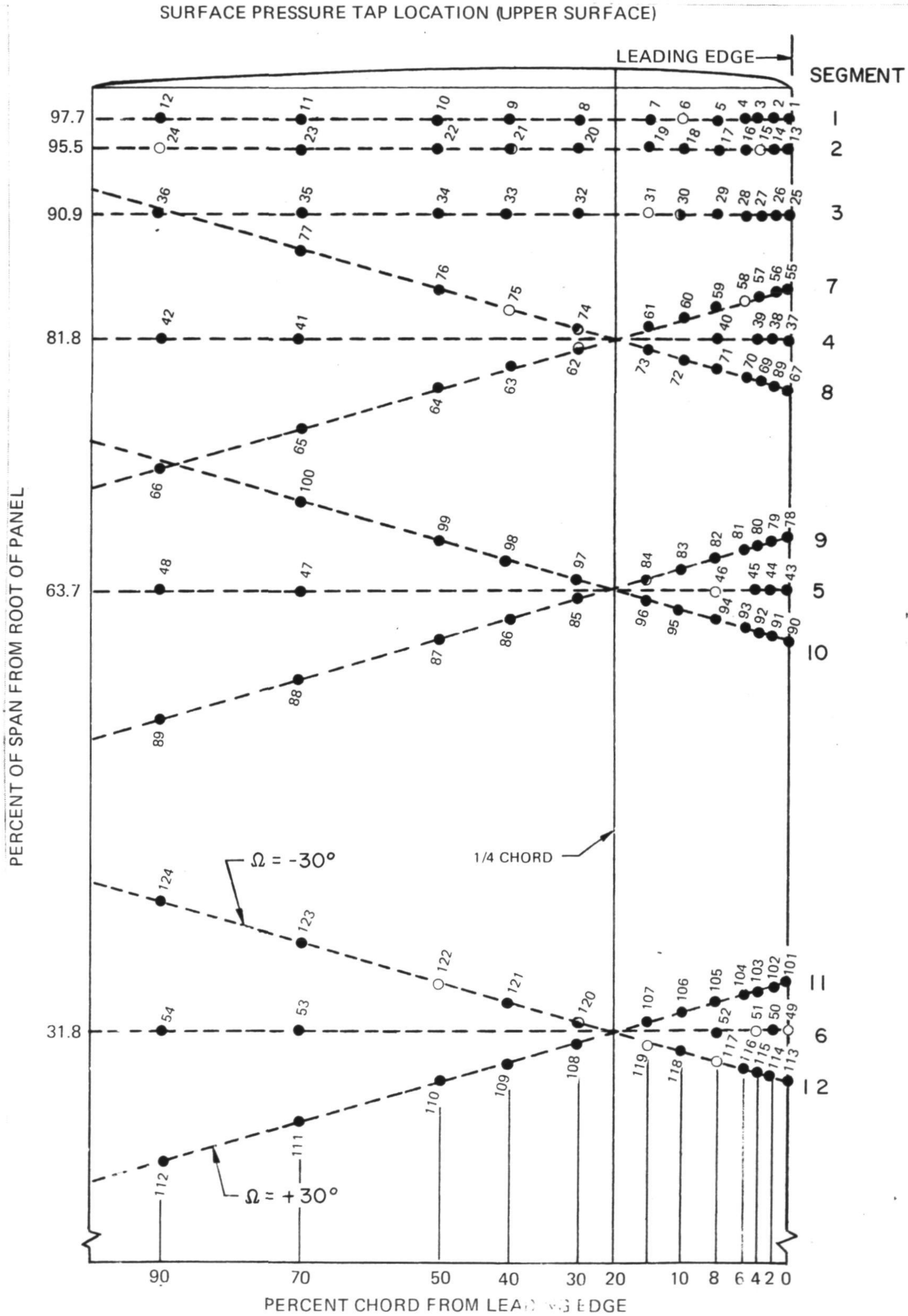

Figure 2. Upper Surface Pressure Tap Location.

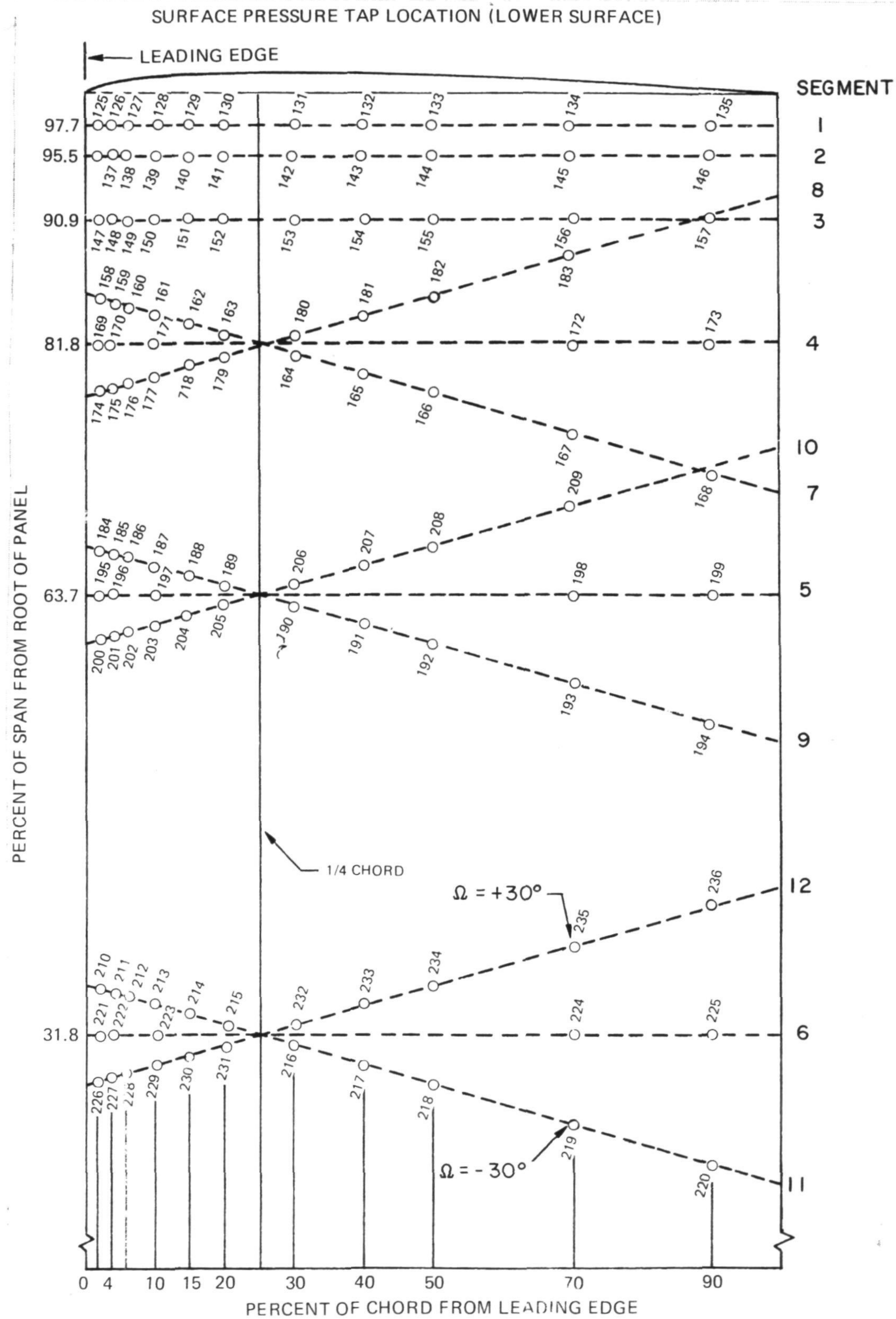

Figure 3. Lower Surface Pressure Tap Location.

Figure 4. Wing Installed in Wind Tunnel.

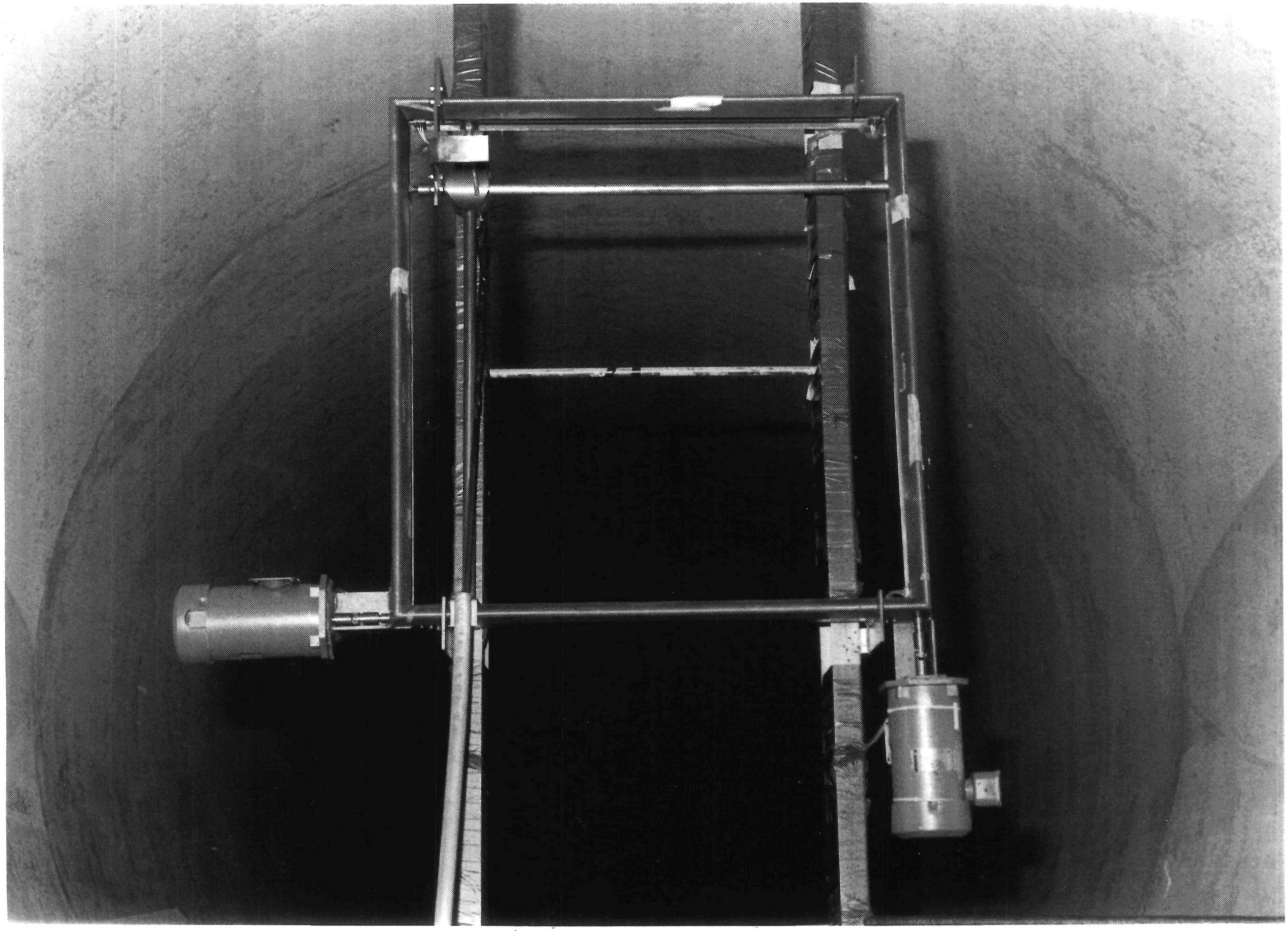

Figure 5. Hot Wire Probe and Traverse Mechanism Installed in Wind Tunnel.

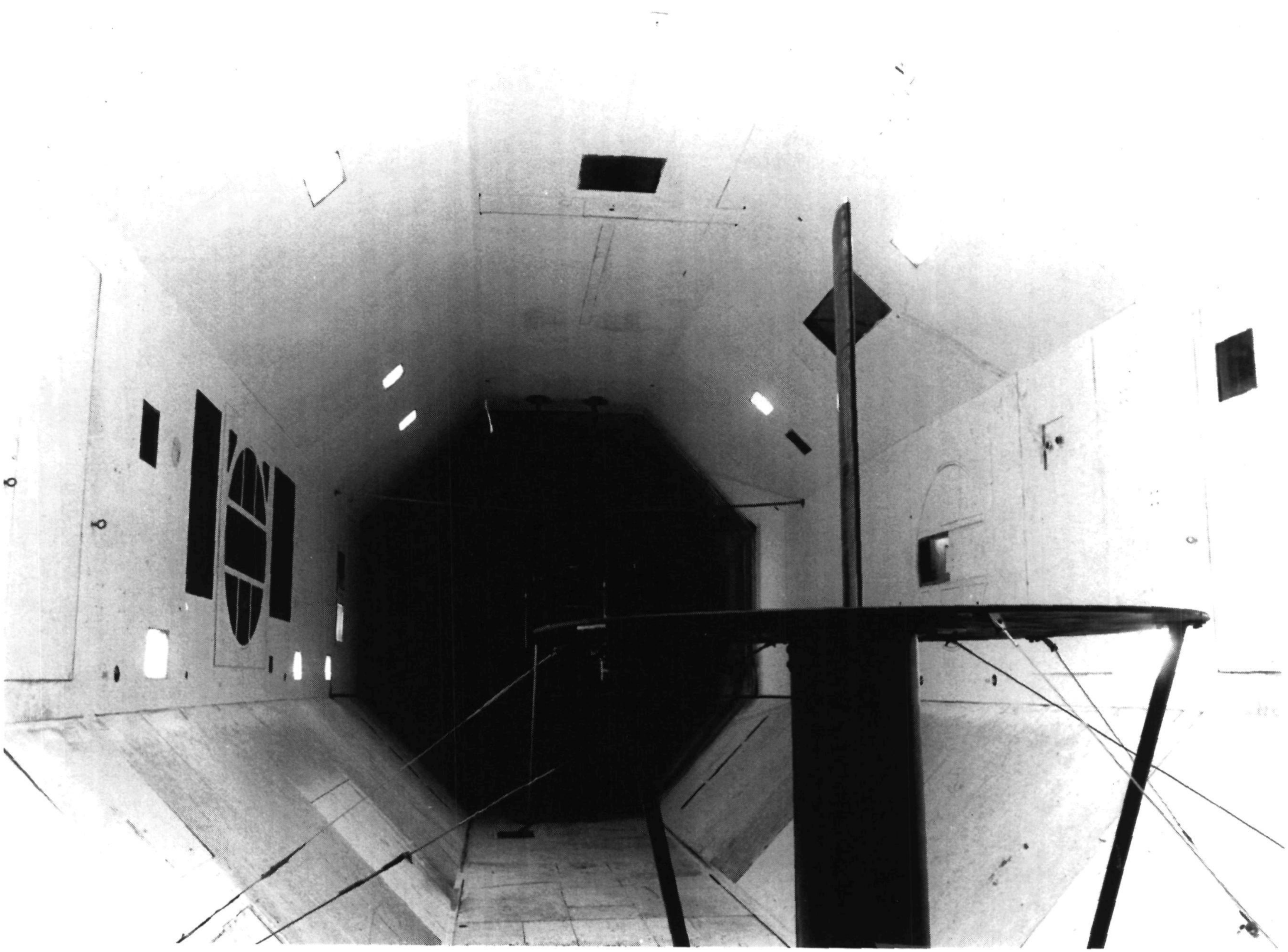

Figure 5. Concluded.

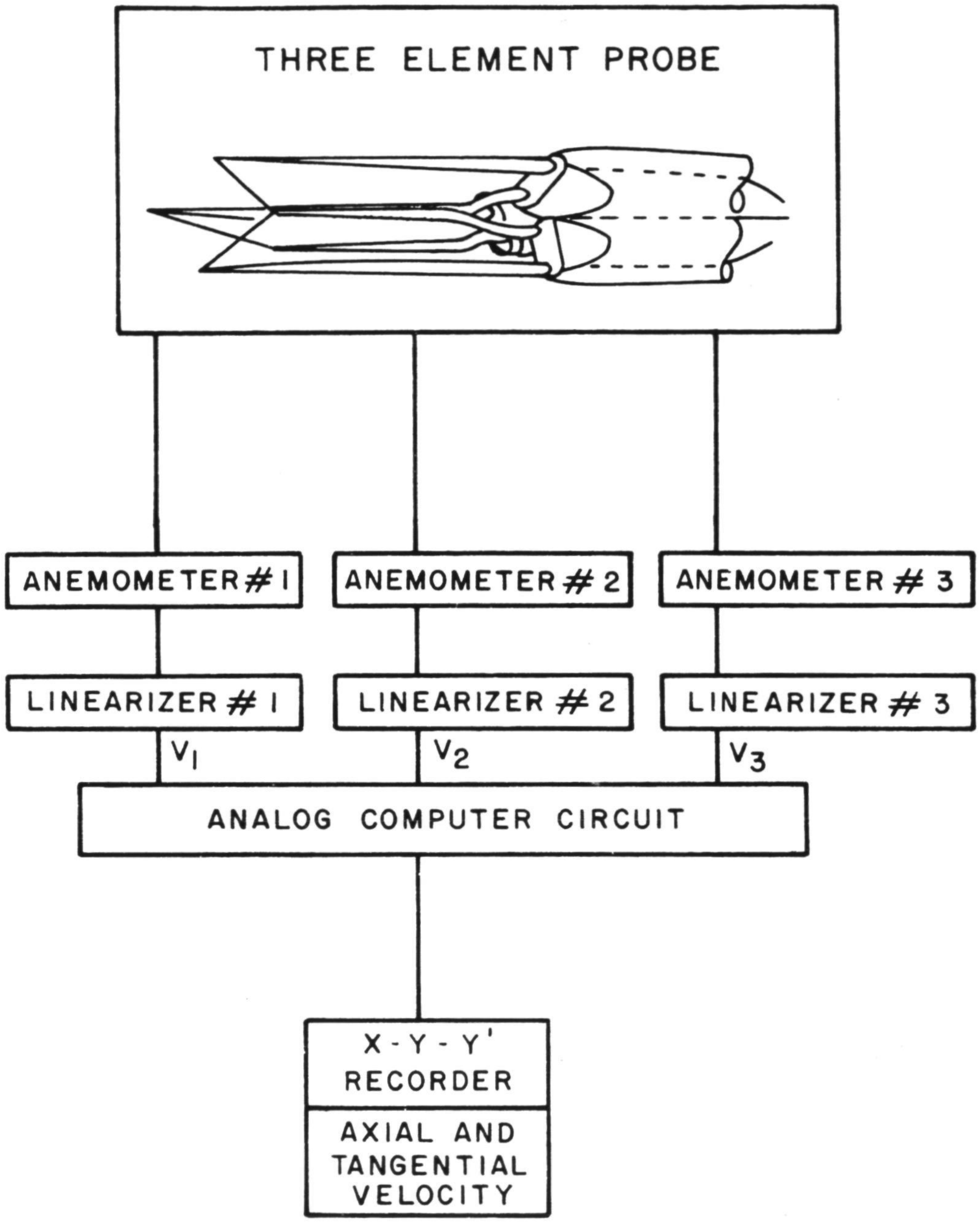

Figure 6. Schematic of Hot Wire Probe Instrumentation.

Figure 7. Hot Wire Probe Instrumentation Setup.

This page intentionally left blank.

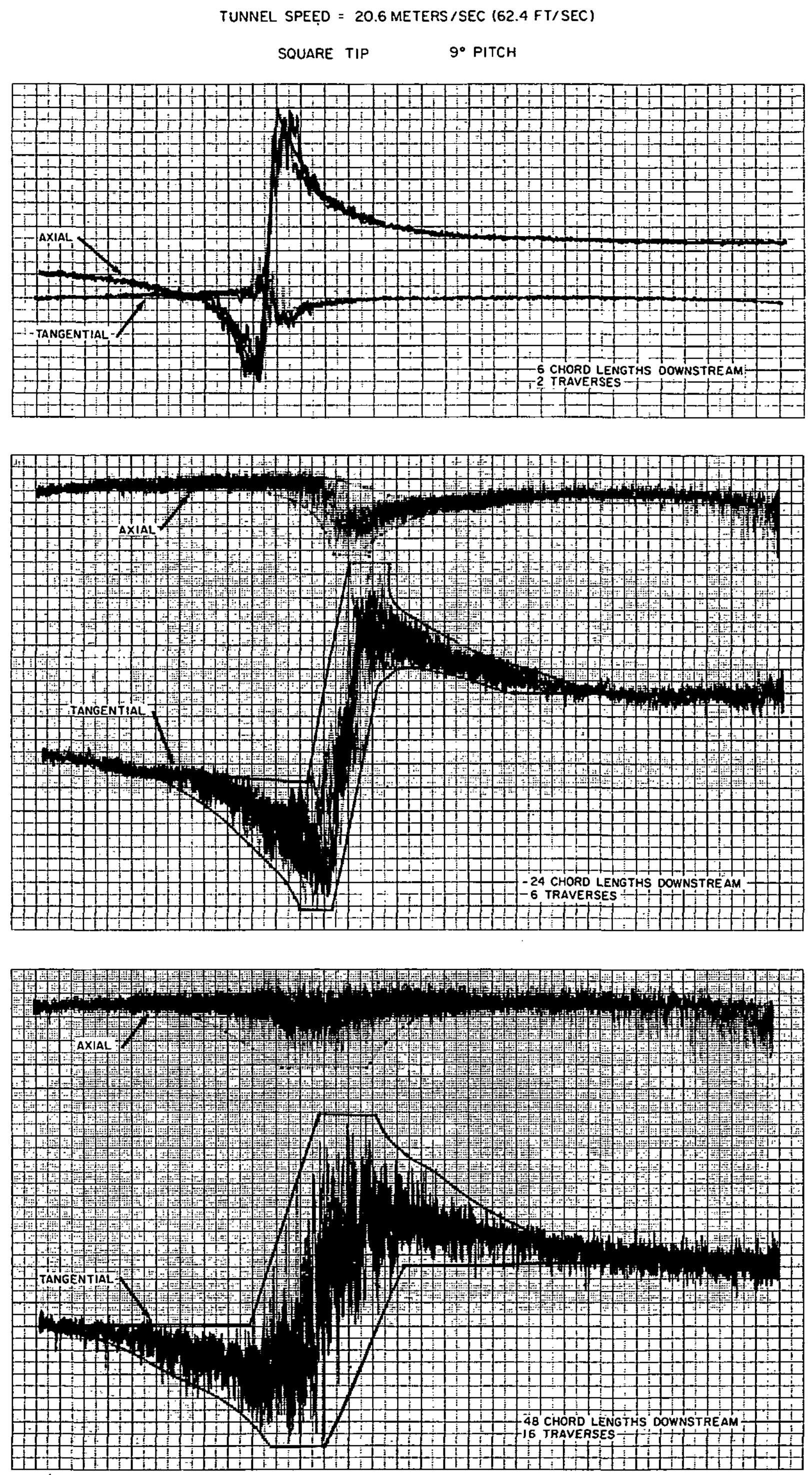

Figure 8. Effect of Downstream Location on Vortex Stability.

Z/C = 24 CHORD LENGTHS
SQUARE TIP 9° PITCH

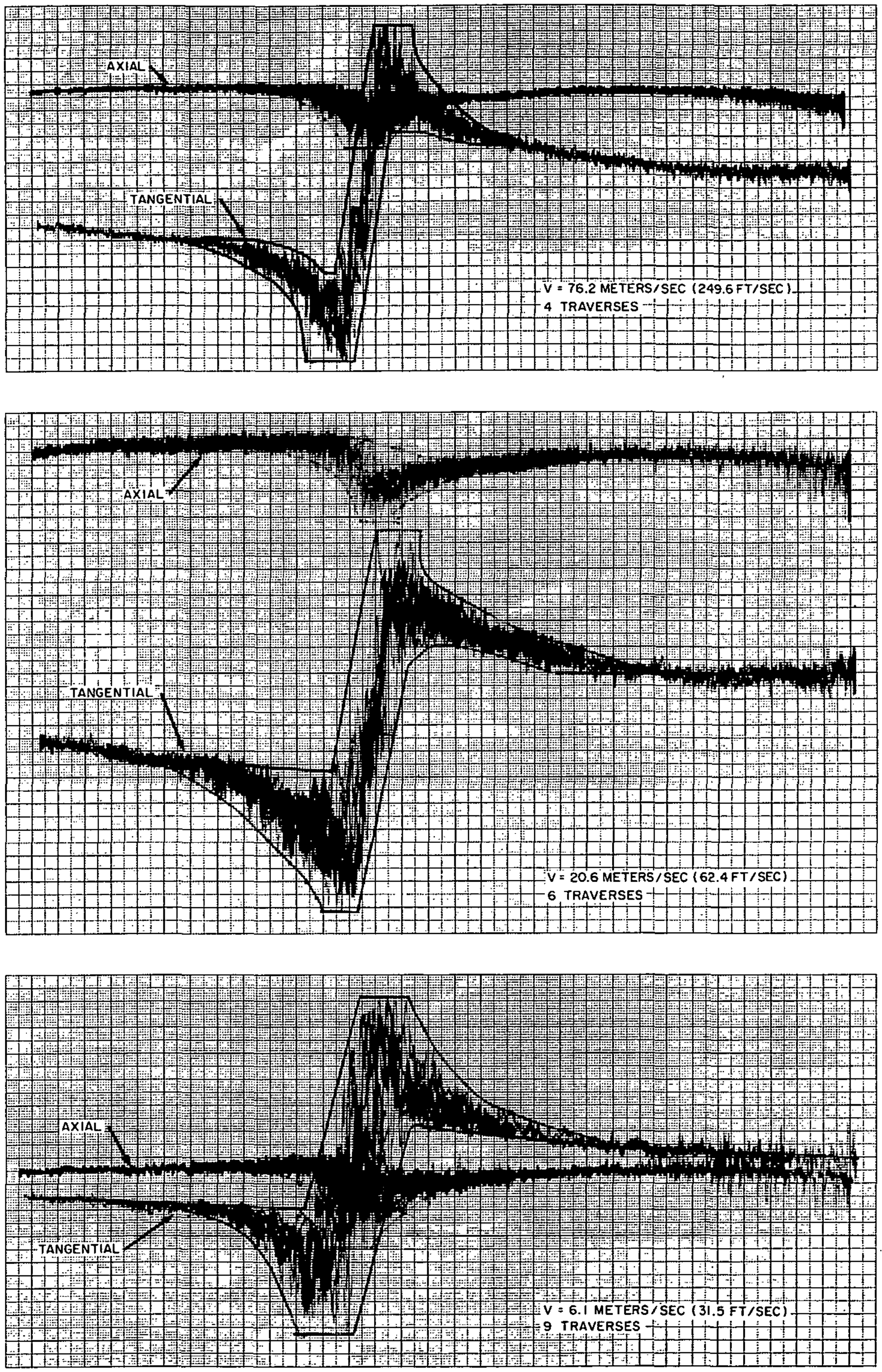

Figure 9. Effect of Free Stream Velocity on Vortex Stability.

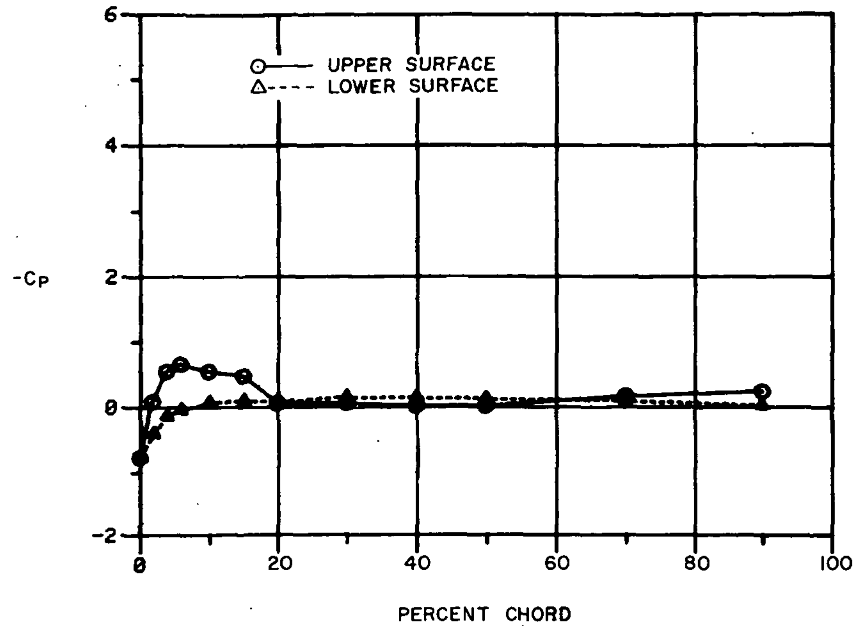

REVOLVED TIP AIRFOIL

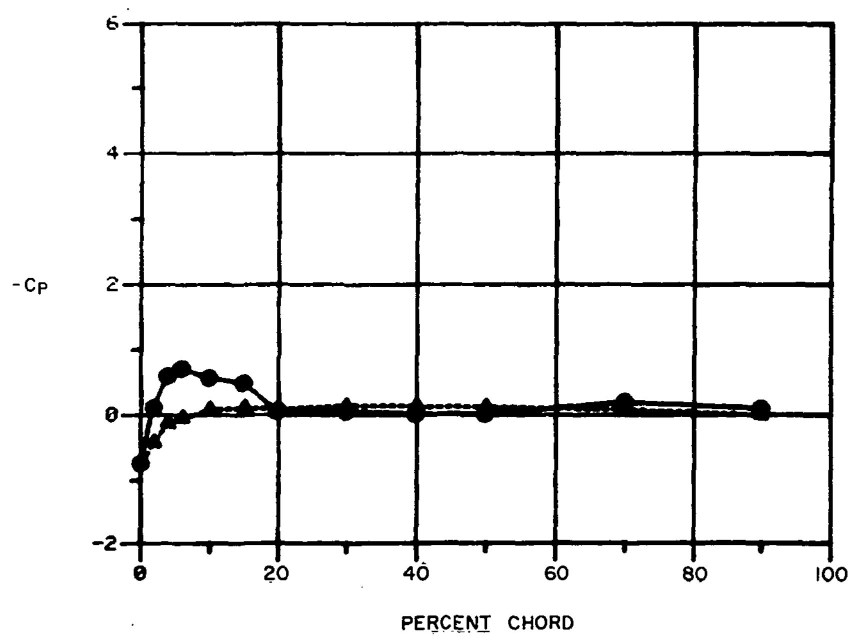

SQUARE TIP AIRFOIL

Figure 10. Surface Pressure Coefficients, 6^{o} α, Segment 1

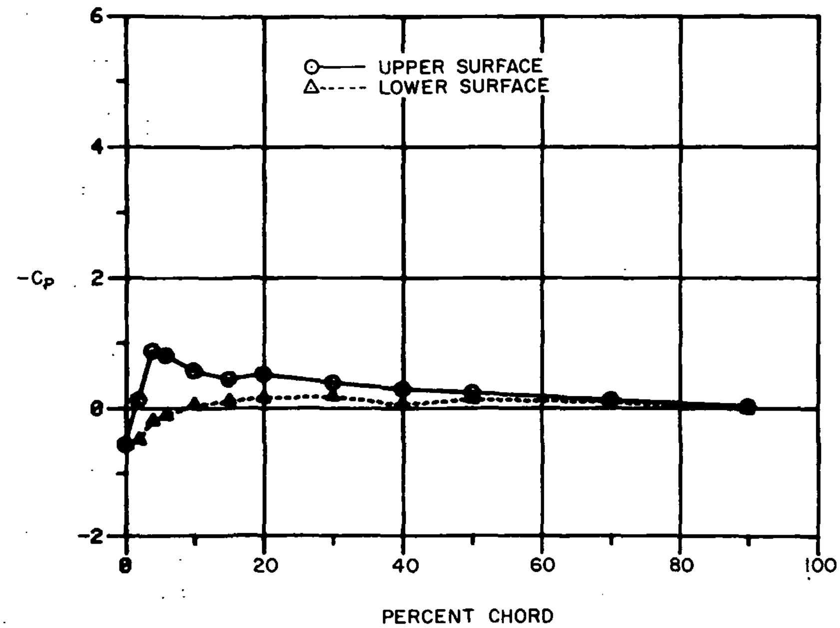

REVOLVED TIP AIRFOIL

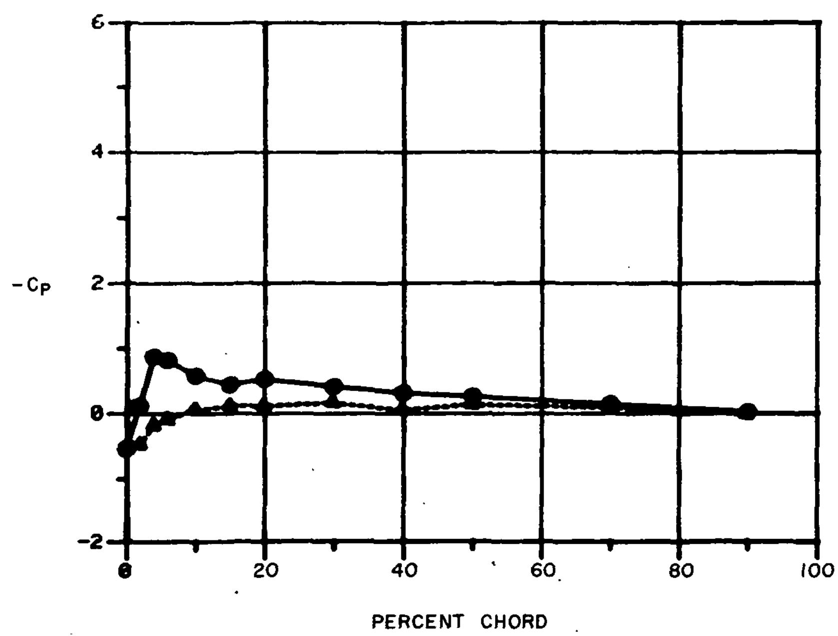

SQUARE TIP AIRFOIL

Figure 10. (Continued) Surface Pressure Coefficients, 6^{o} α, Segment 2

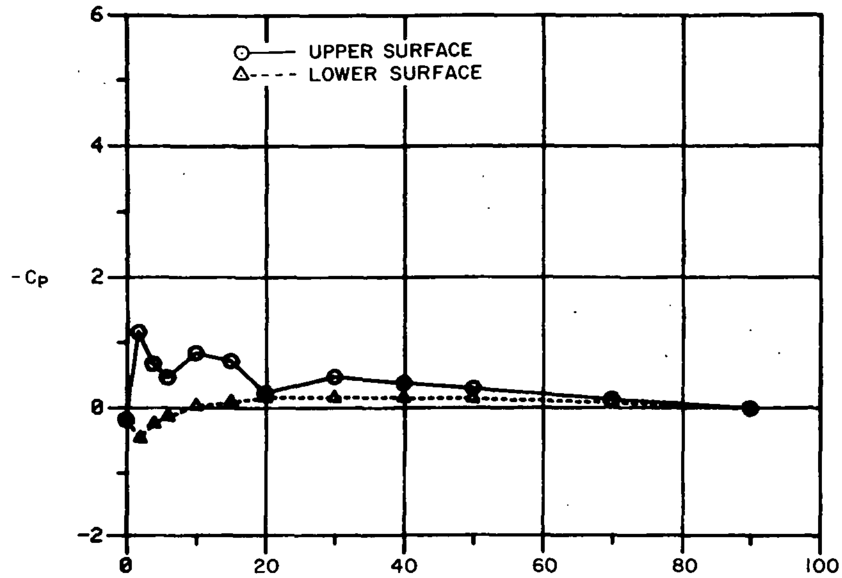

REVOLVED TIP AIRFOIL

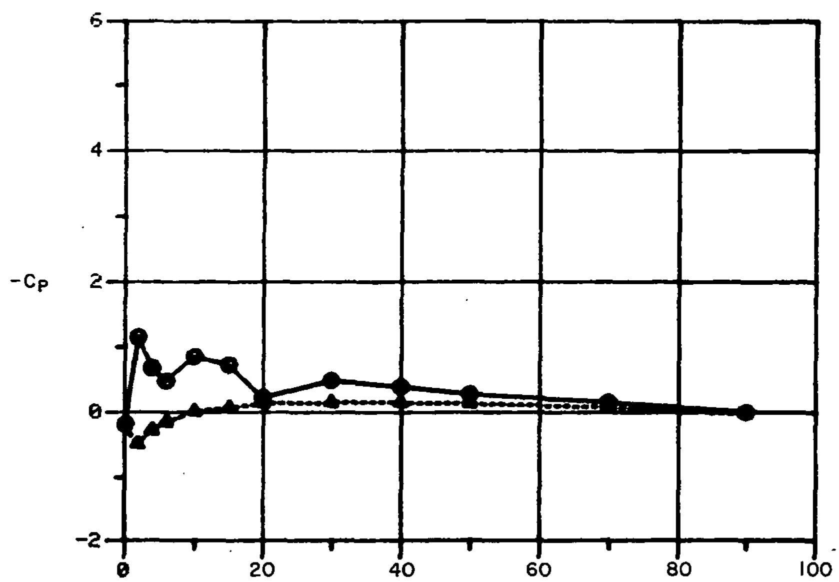

SQUARE TIP AIRFOIL

Figure 10. (Continued) Surface Pressure Coefficients, 6^{o} α, Segment 3

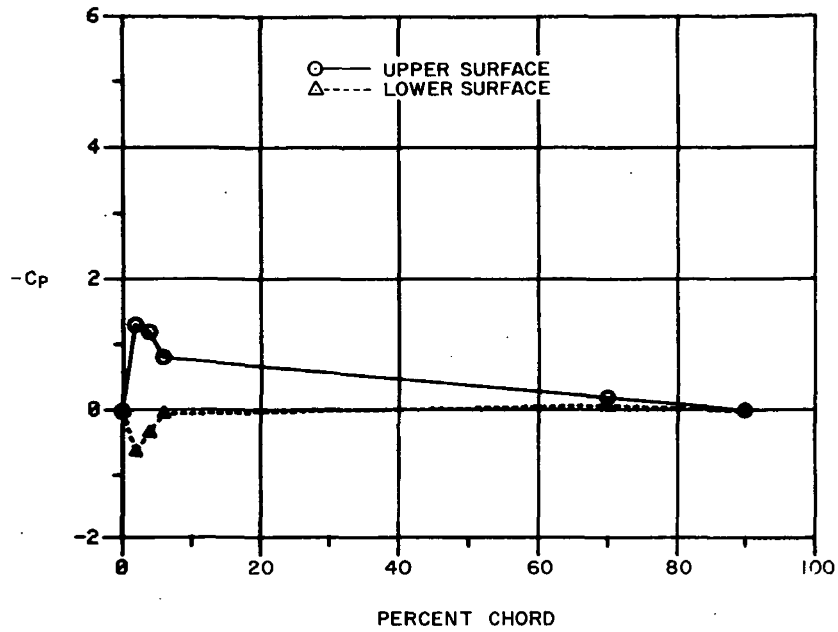

REVOLVED TIP AIRFOIL

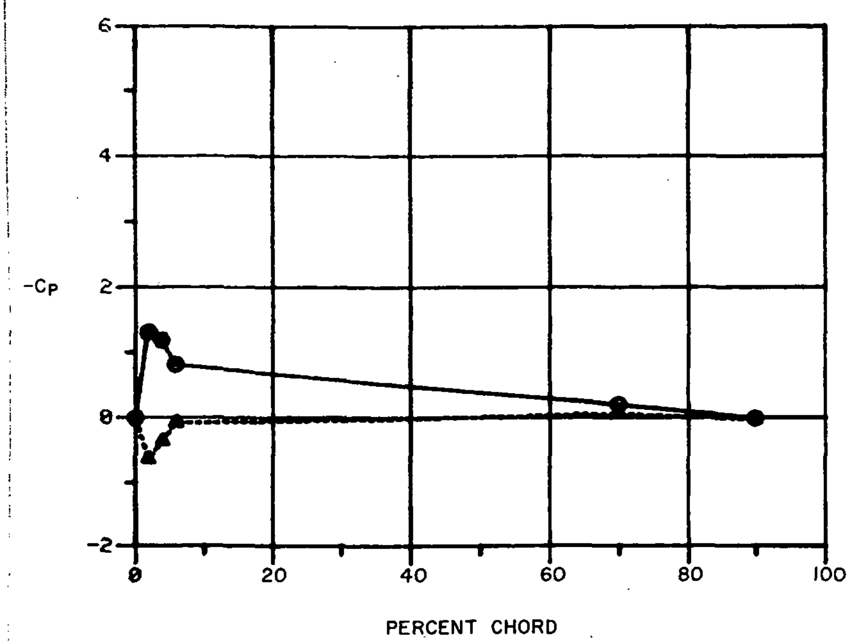

SQUARE TIP AIRFOIL

Figure 10. (Continued) Surface Pressure Coefficients, 6° α, Segment 4

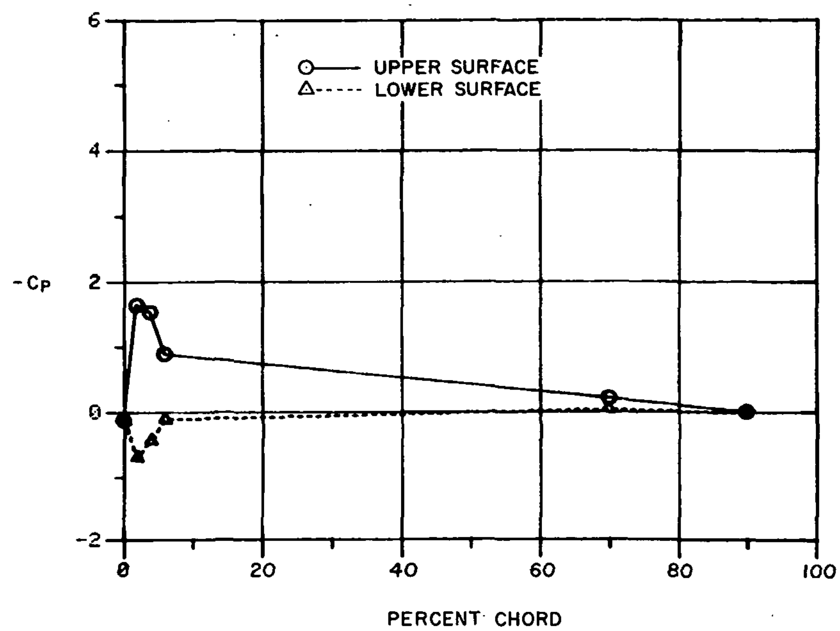

REVOLVED TIP AIRFOIL

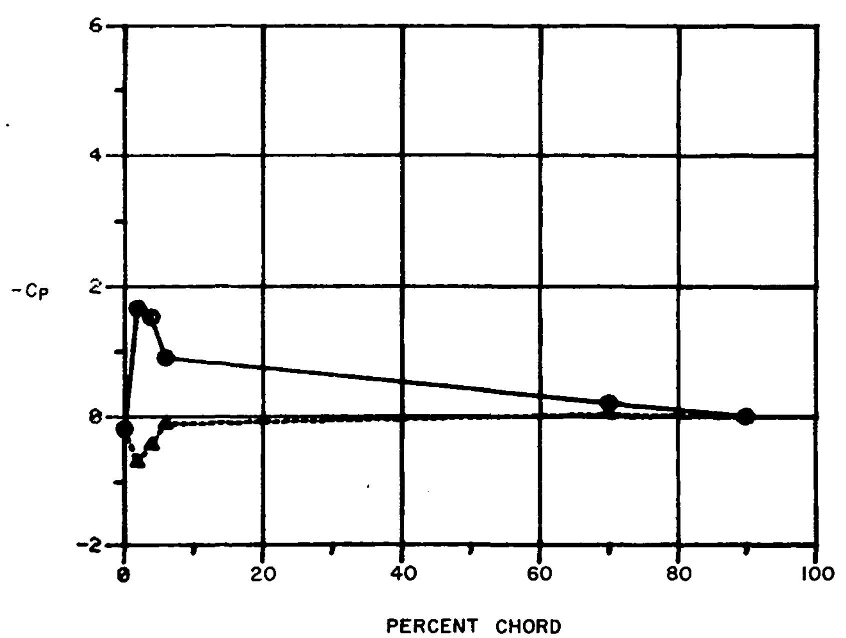

SQUARE TIP AIRFOIL

Figure 10. (Continued) Surface Pressure Coefficients, 6^{o} α, Segment 5

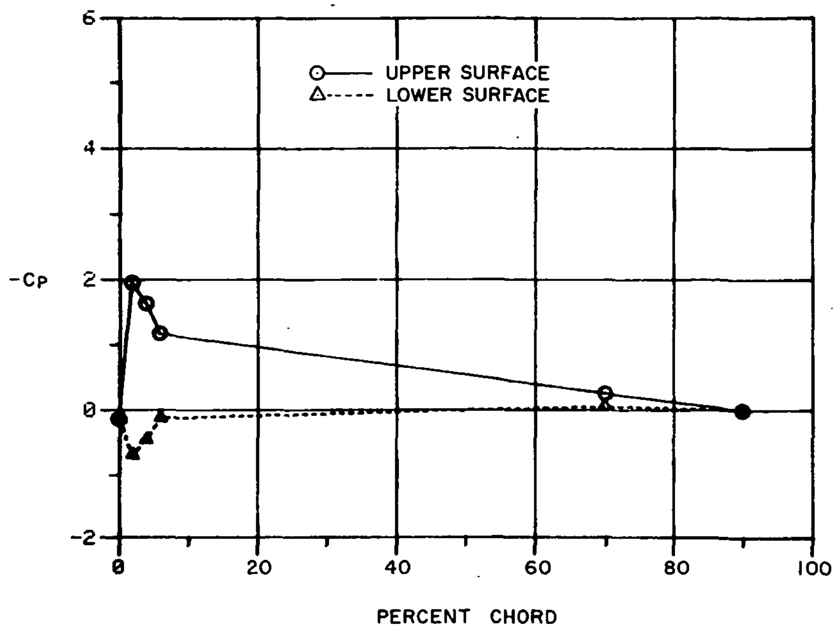

REVOLVED TIP AIRFOIL

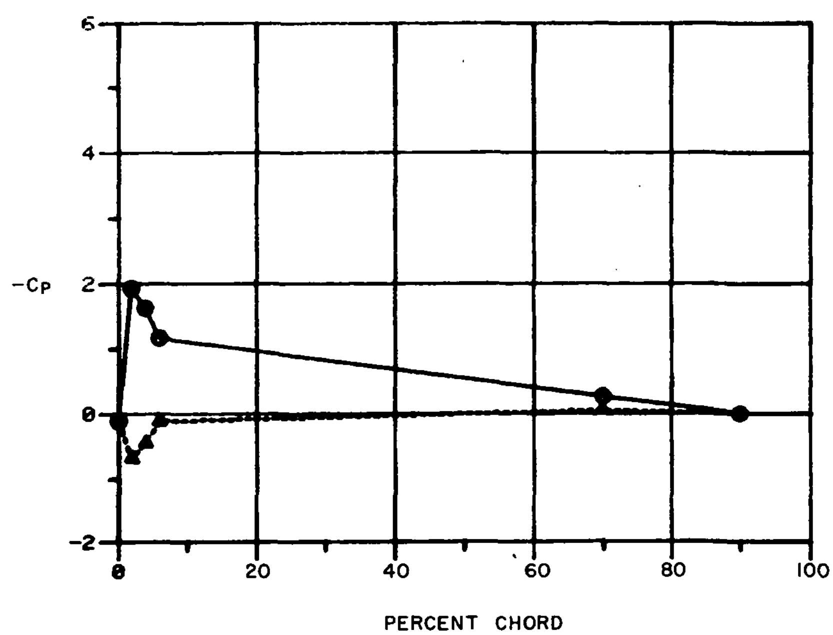

SQUARE TIP AIRFOIL

Figure 10. (Continued) Surface Pressure Coefficients, 6^{0} α, Segment 6

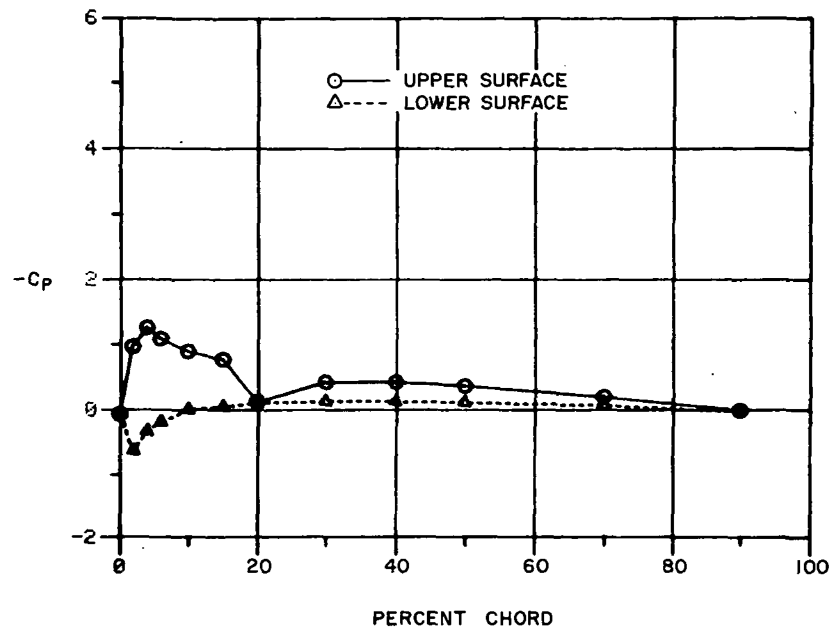

REVOLVED TIP AIRFOIL

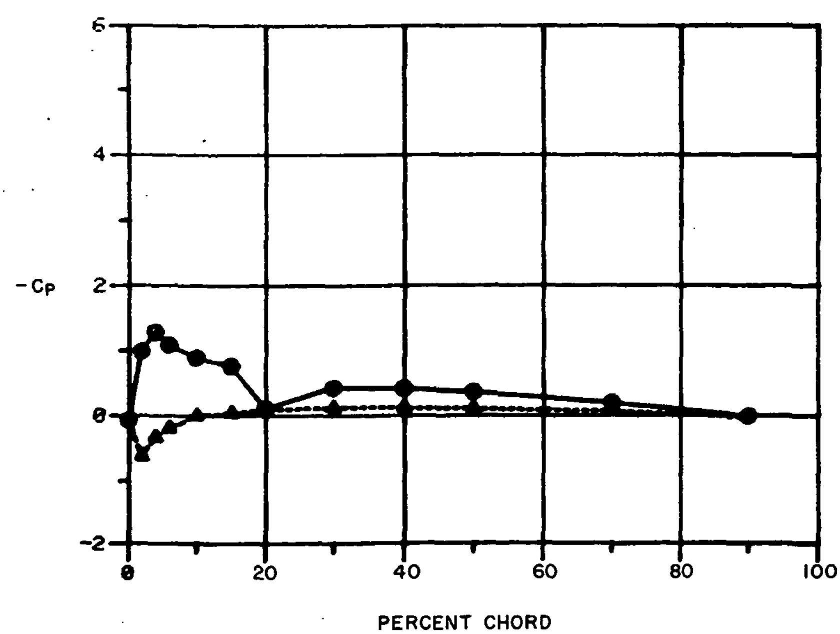

SQUARE TIP AIRFOIL

Figure 10. (Continued) Surface Pressure Coefficients, 6^{o} α, Segment 7

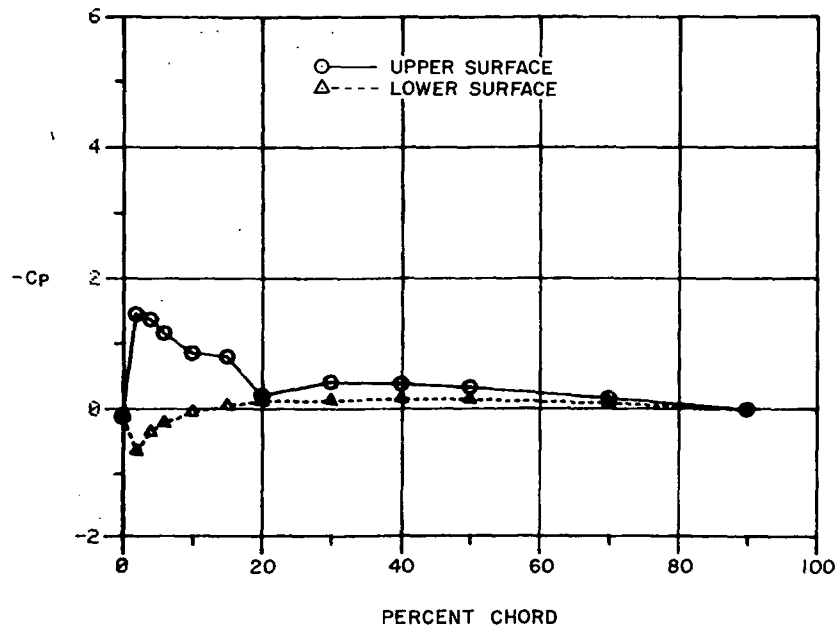

REVOLVED TIP AIRFOIL

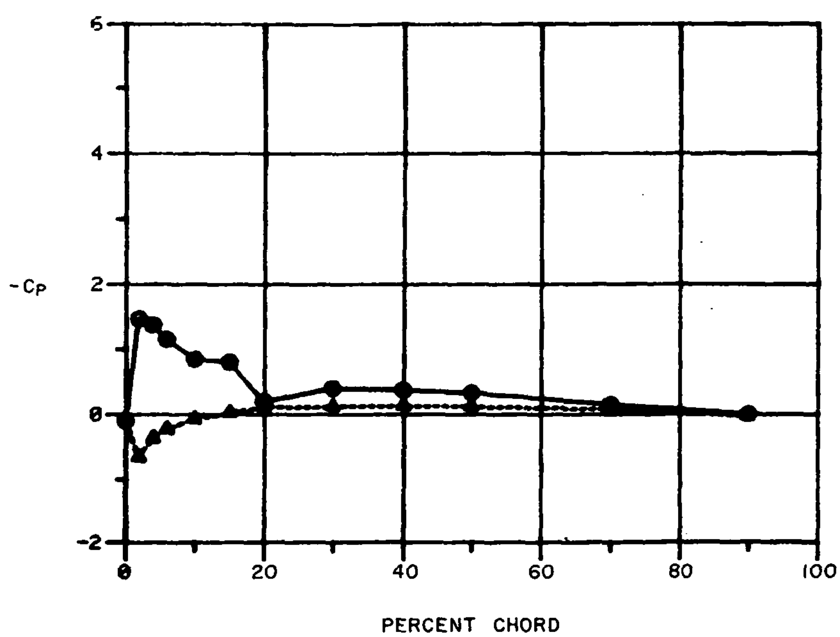

SQUARE TIP AIRFOIL

Figure 10. (Continued) Surface Pressure Coefficients, 6° α. Segment 8

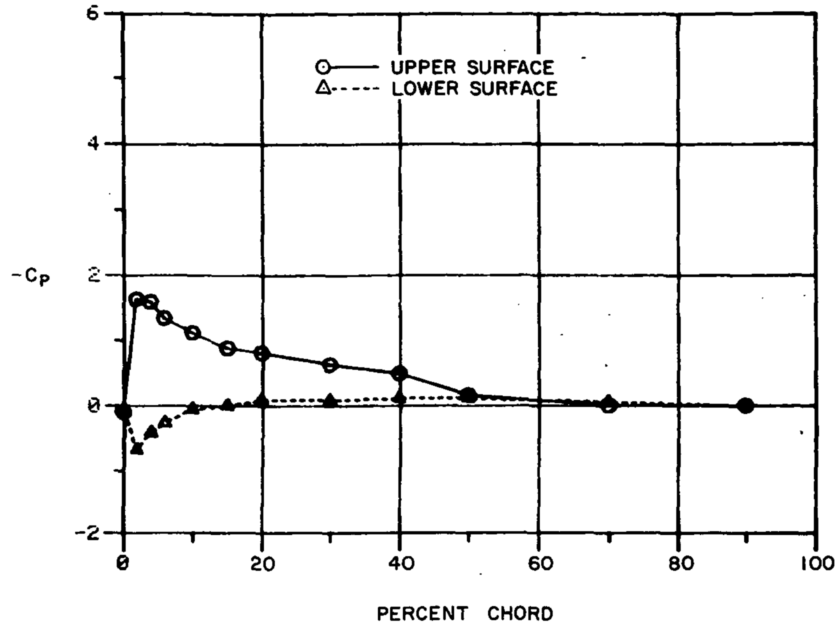

REVOLVED TIP AIRFOIL

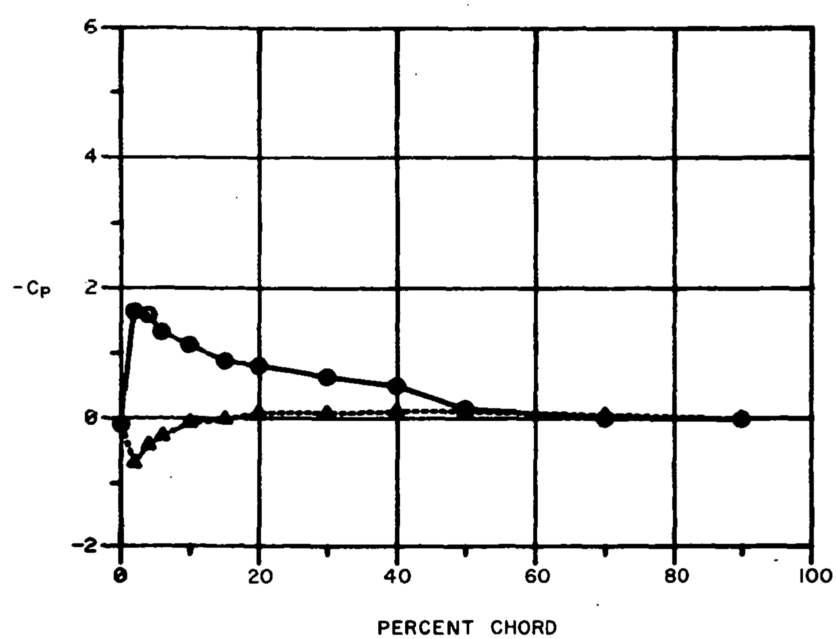

SQUARE TIP AIRFOIL

Figure 10. (Continued) Surface Pressure Coefficients, 6^{o} α, Segment 9

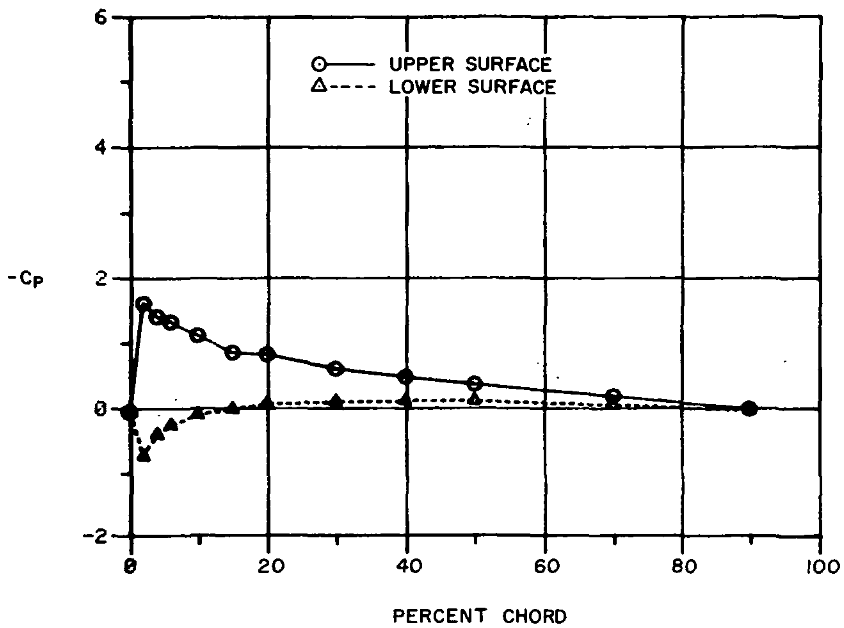

REVOLVED TIP AIRFOIL

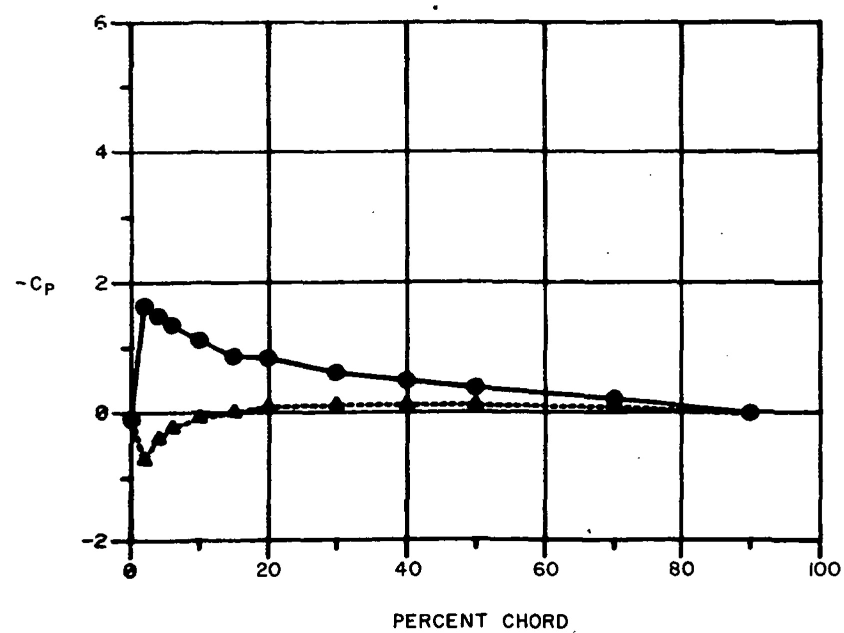

SQUARE TIP AIRFOIL

Figure 10. (Continued) Surface Pressure Coefficients, 6^{0} α, Segment 10

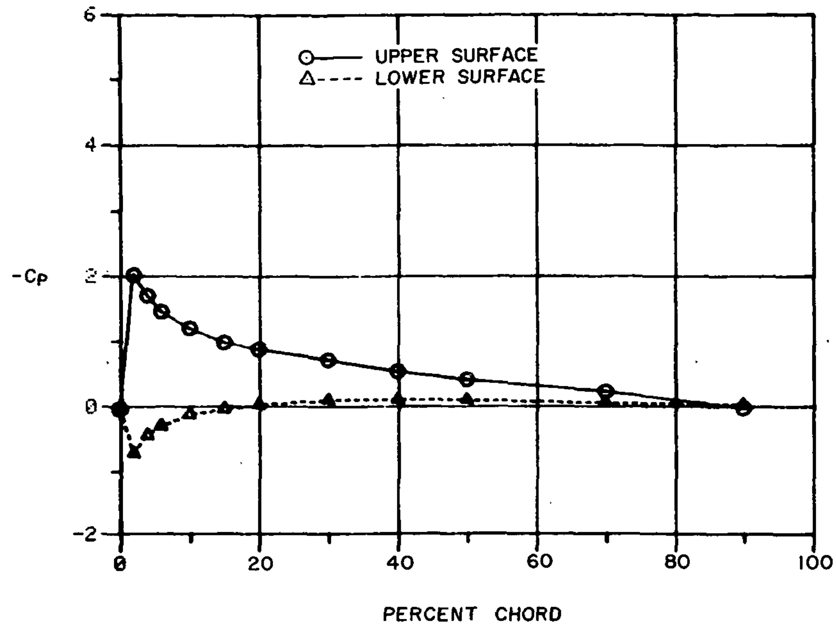

REVOLVED TIP AIRFOIL

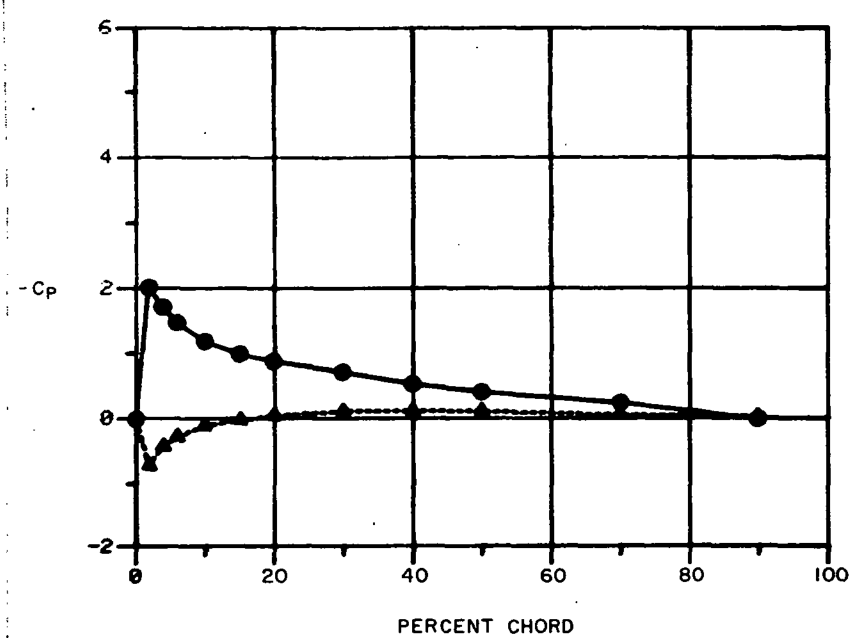

SQUARE TIP AIRFOIL

Figure 10. (Continued) Surface Pressure Coefficients, 6^{o} α, Segment 11

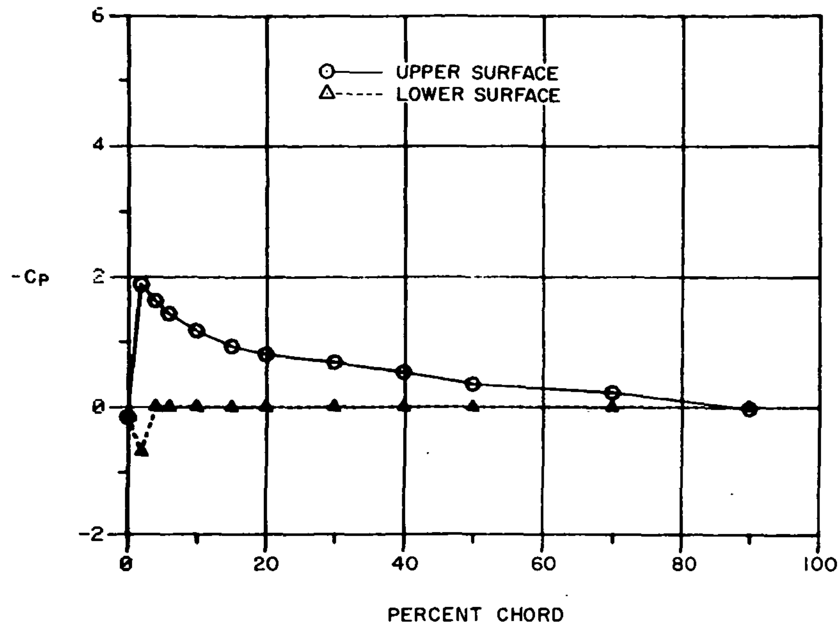

REVOLVED TIP AIRFOIL

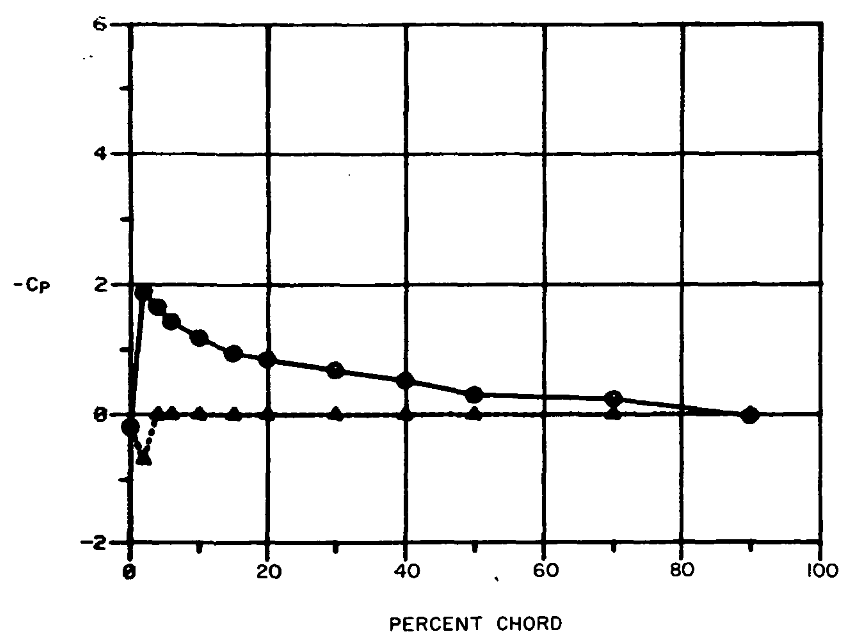

SQUARE TIP AIRFOIL

Figure 10. (Concluded) Surface Pressure Coefficients, 6° α, Segment 12

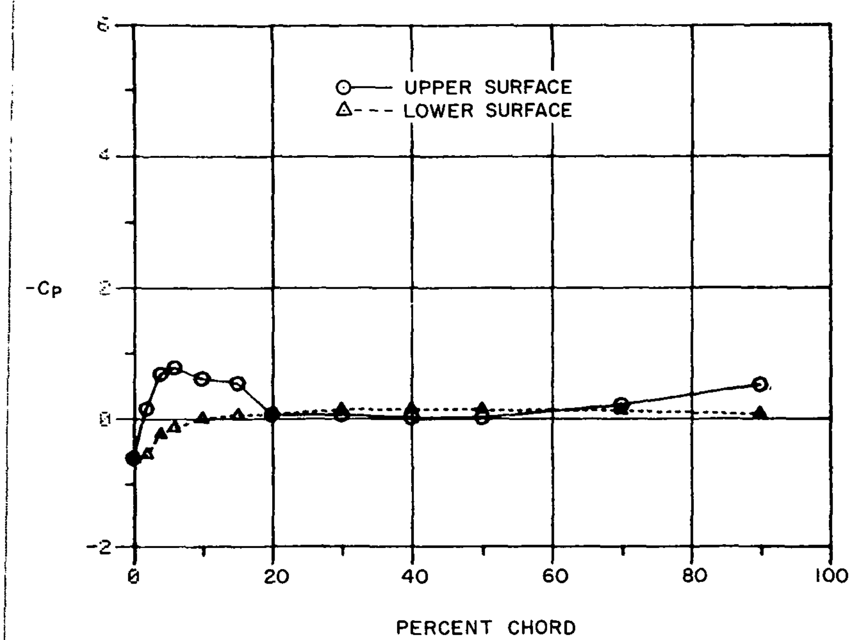

REVOLVED TIP AIRFOIL

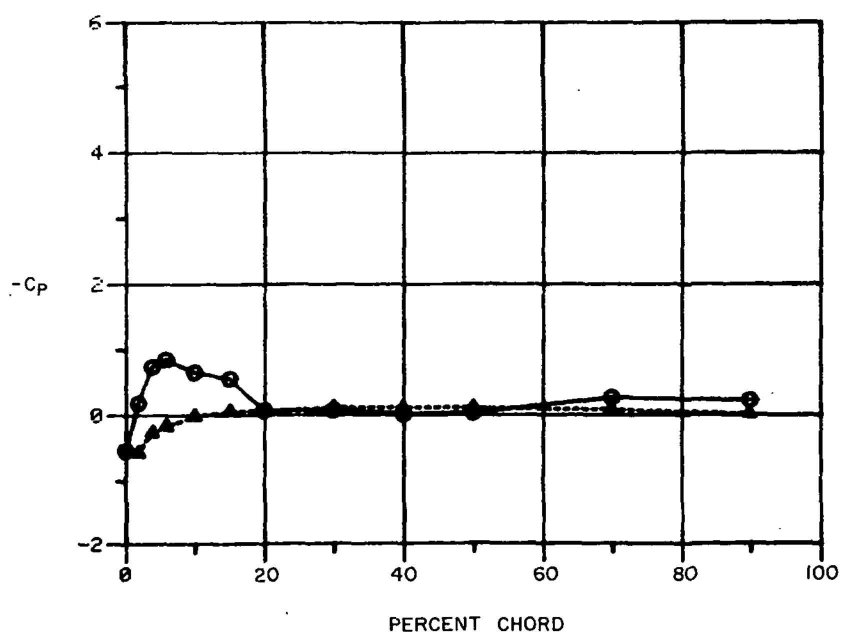

SQUARE TIP AIRFOIL

Figure 11. Surface Pressure Coefficients, 8^{o} α, Segment 1

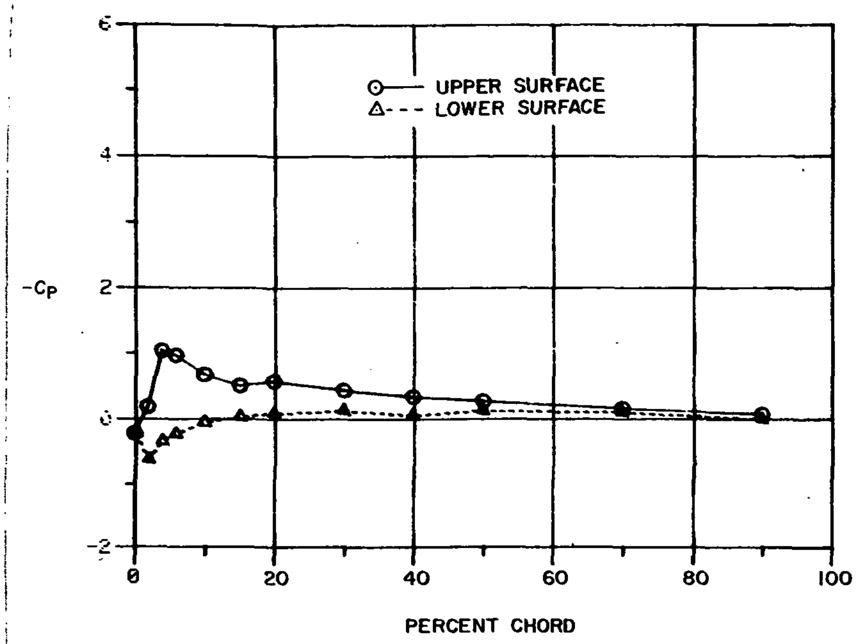

REVOLVED TIP AIRFOIL

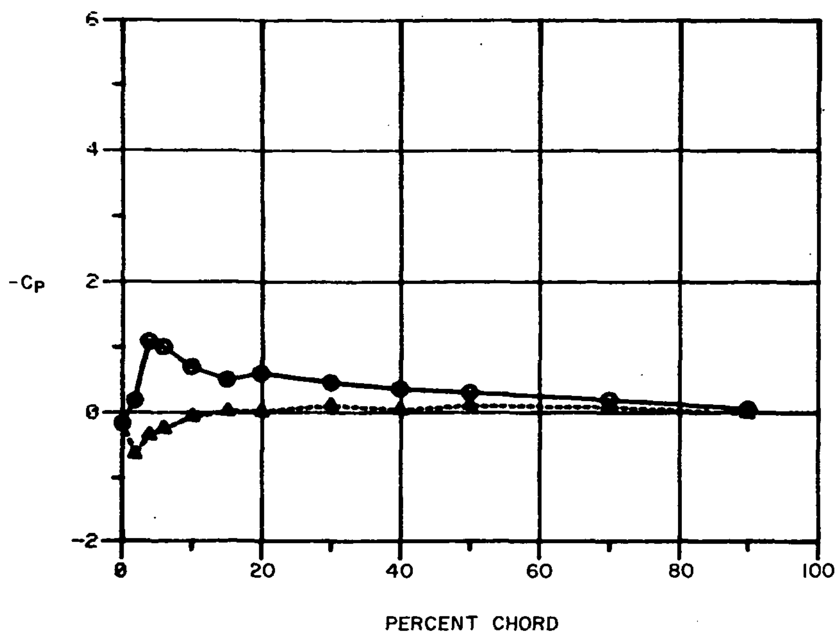

SQUARE TIP AIRFOIL

Figure 11. (Continued) Surface Pressure Coefficients, 8^{o} α, Segment 2

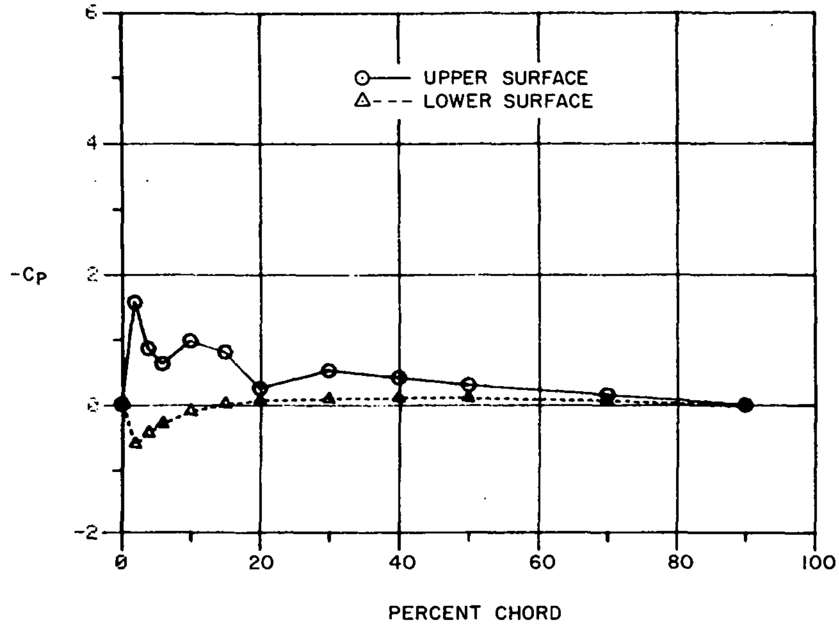

REVOLVED TIP AIRFOIL

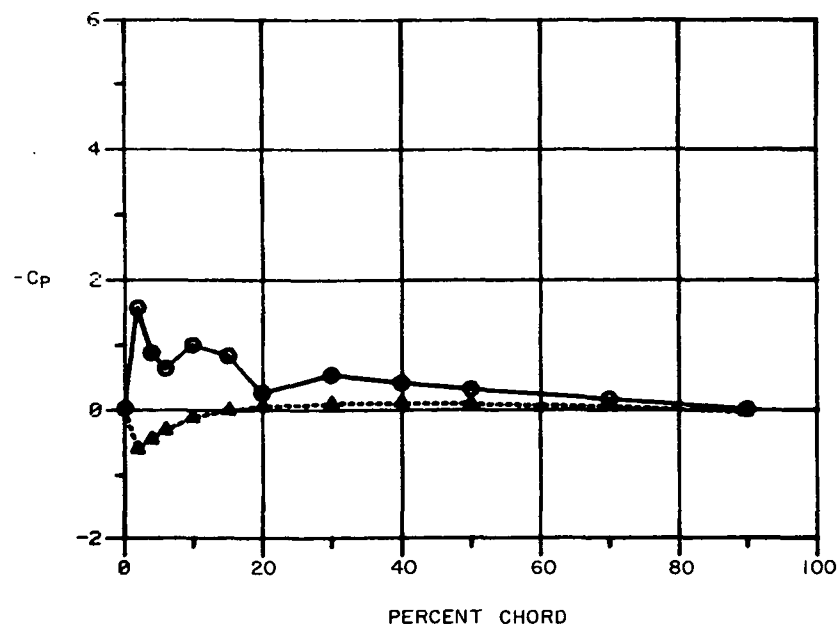

SQUARE TIP AIRFOIL

Figure 11. (Continued) Surface Pressure Coefficients, 8^{o} α, Segment 3

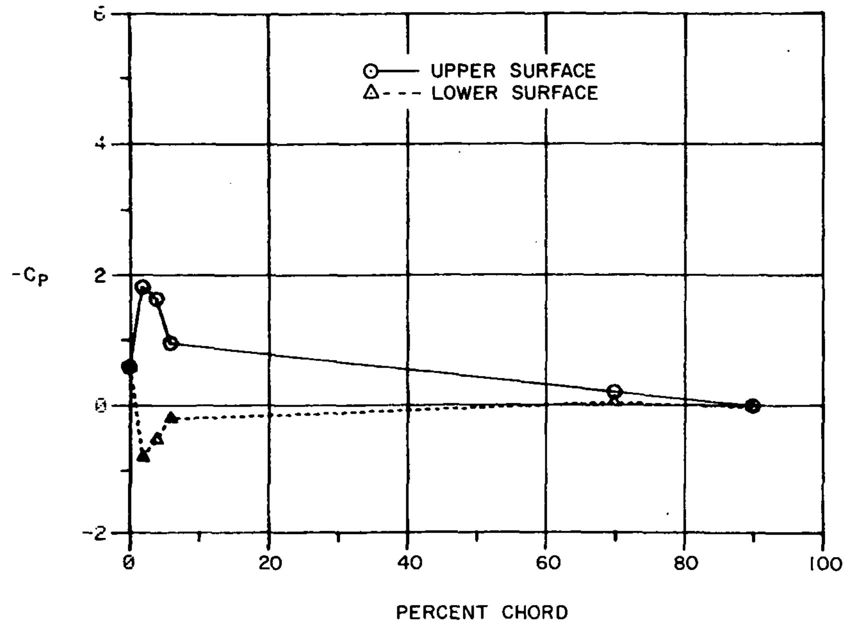

REVOLVED TIP AIRFOIL

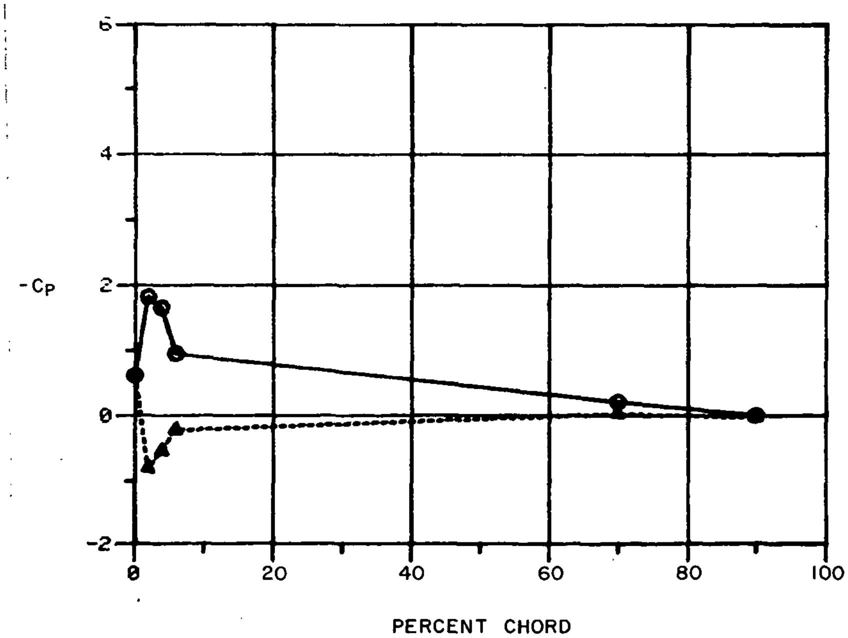

SQUARE TIP AIRFOIL

Figure 11. (Continued) Surface Pressure Coefficients, 8^0 α, Segment 4

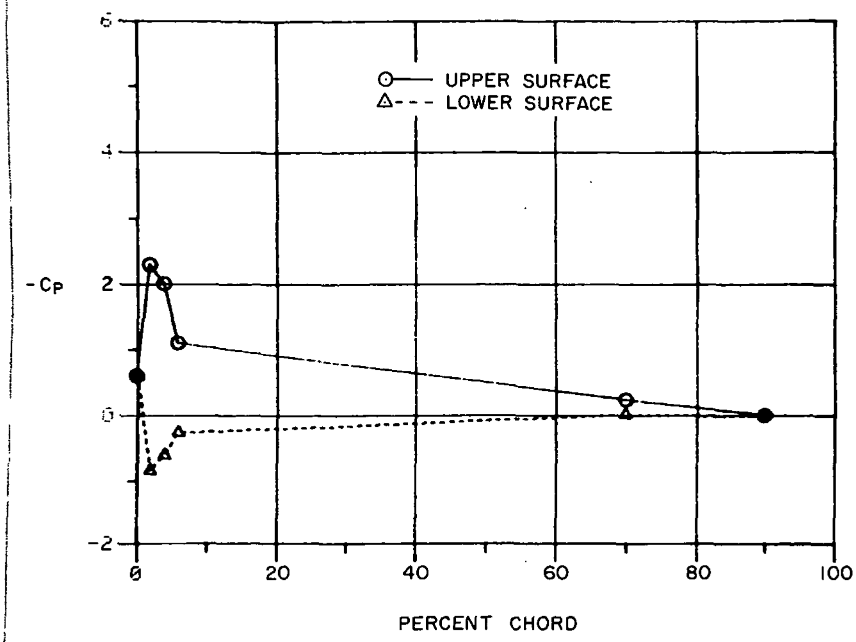

REVOLVED TIP AIRFOIL

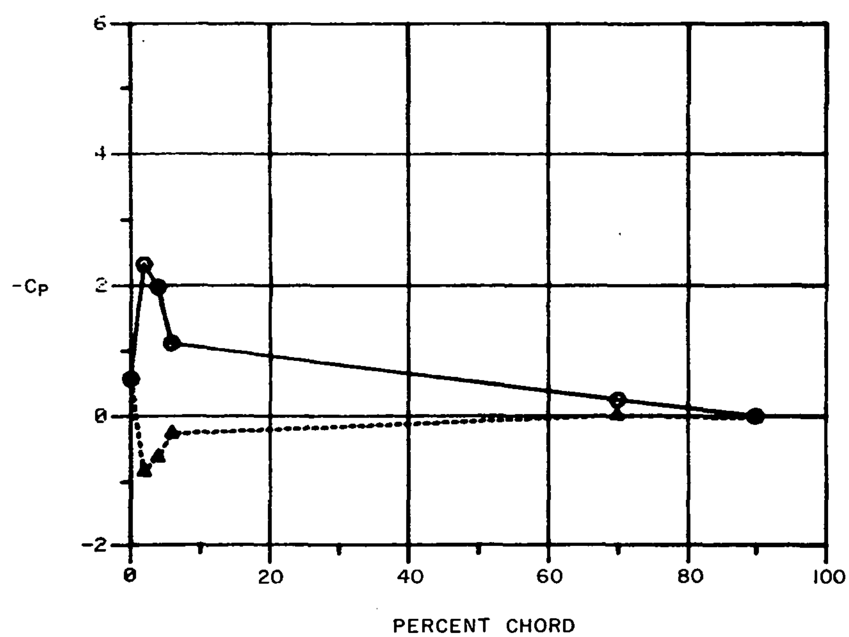

SQUARE TIP AIRFOIL

Figure 11. (Continued) Surface Pressure Coefficients, 8^{o} α, Segment 5

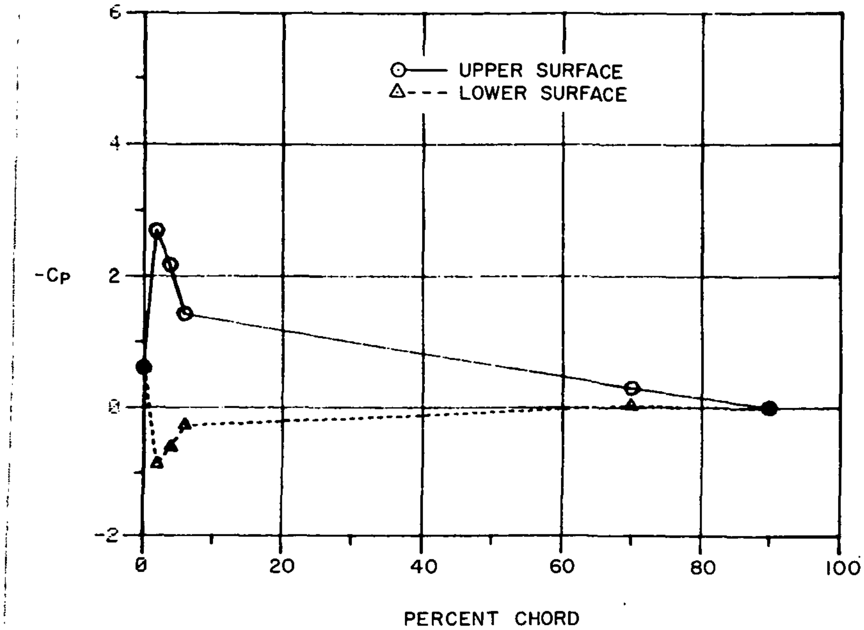

REVOLVED TIP AIRFOIL

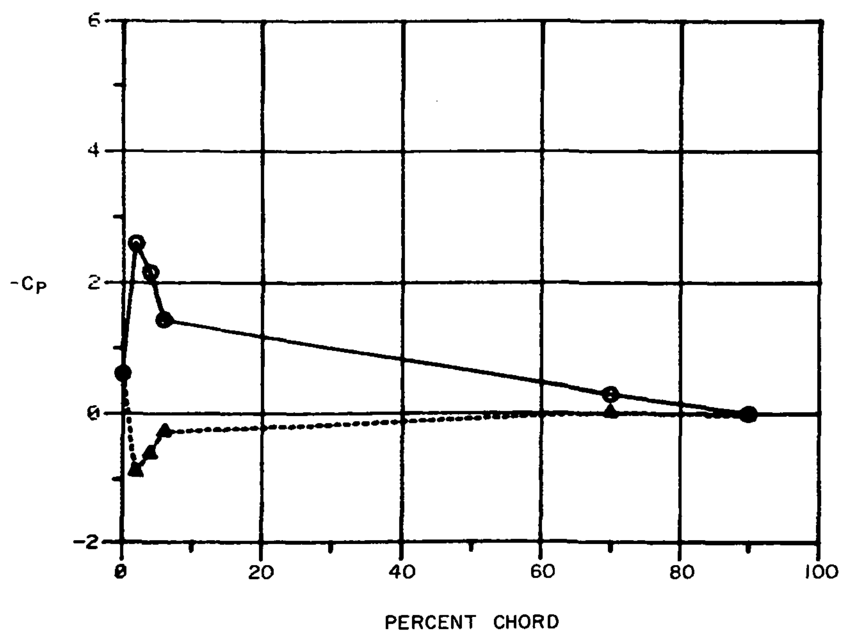

SQUARE TIP AIRFOIL

Figure 11. (Continued) Surface Pressure Coefficients, 8^0 α, Segment 6

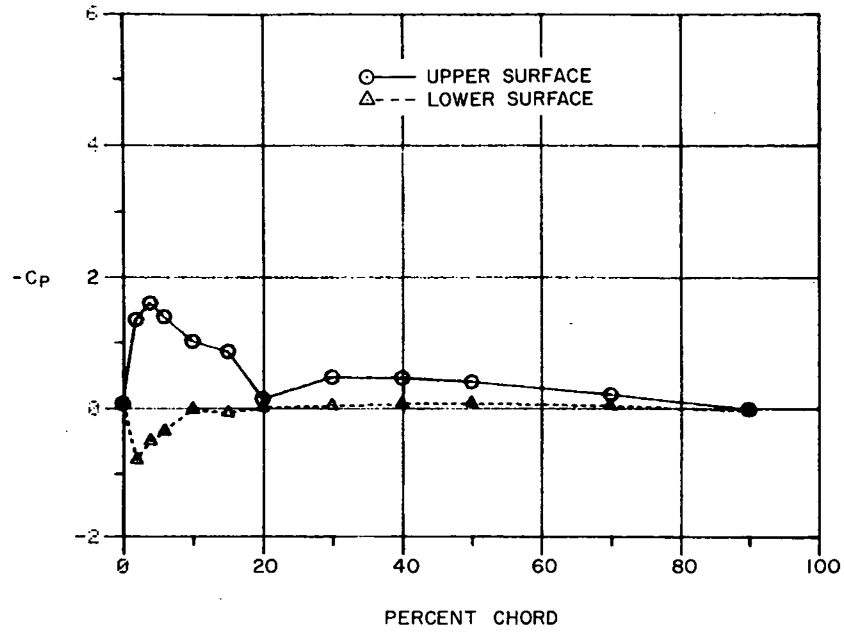

REVOLVED TIP AIRFOIL

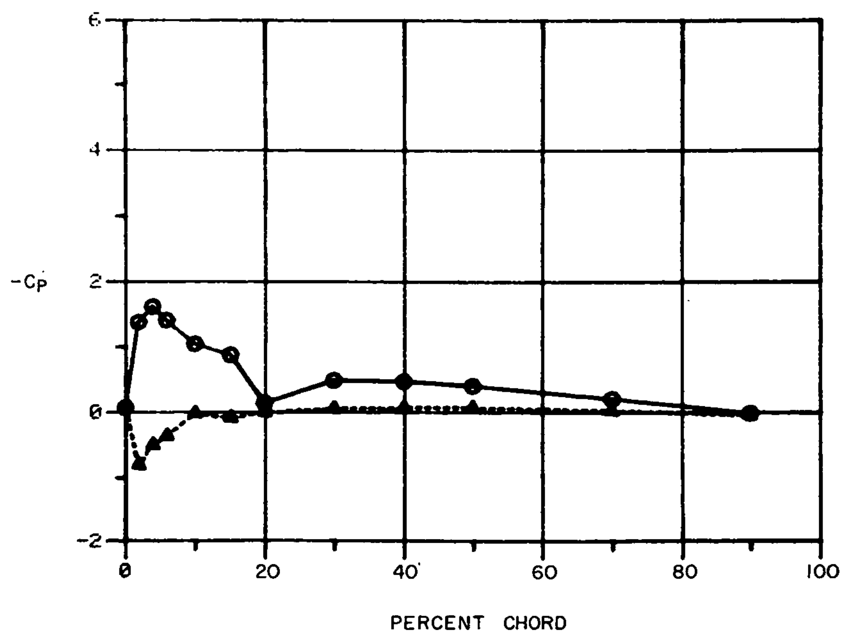

SQUARE TIP AIRFOIL

Figure 11. (Continued) Surface Pressure Coefficients, 8^{0} α, Segment 7

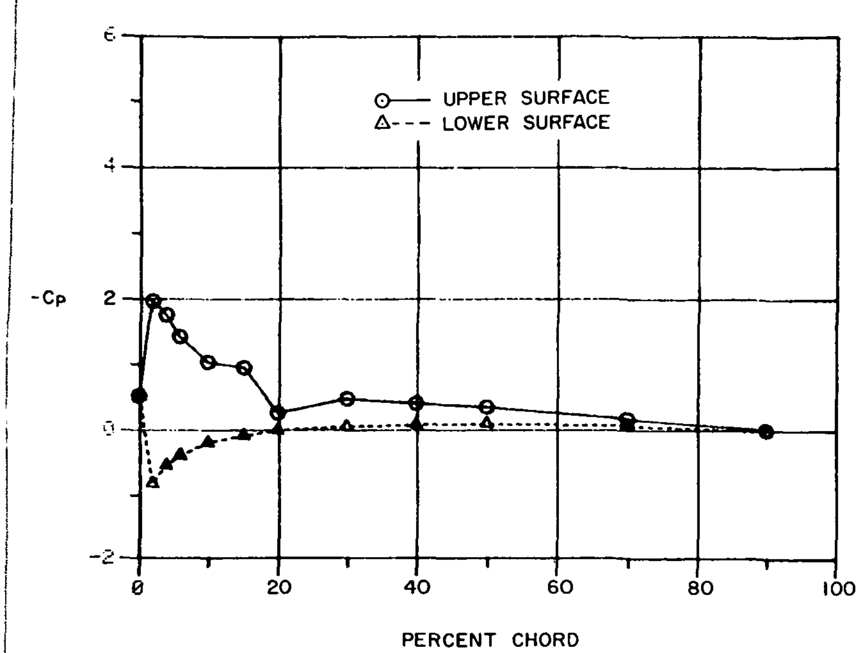

REVOLVED TIP AIRFOIL

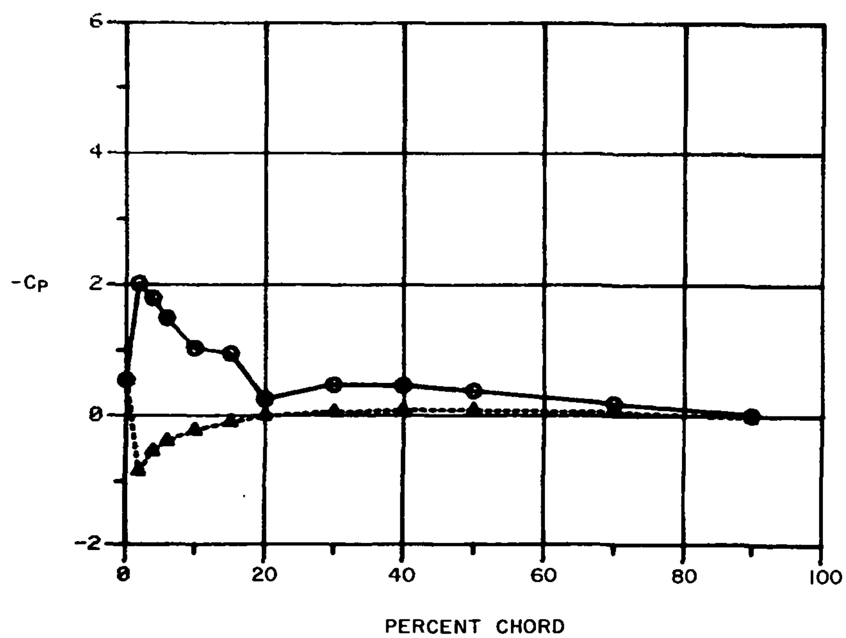

SQUARE TIP AIRFOIL

Figure 11. (Continued) Surface Pressure Coefficients, 8^{o} α, Segment 8

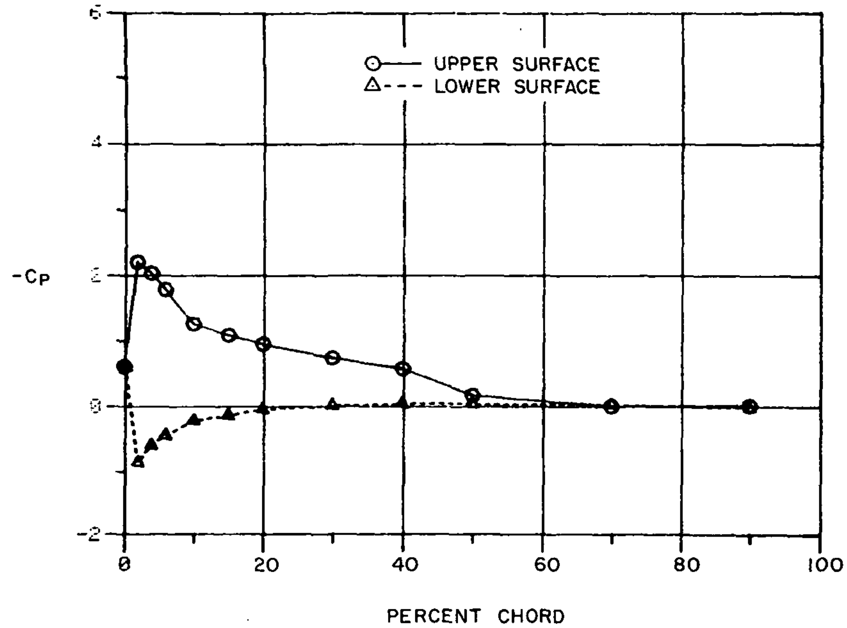

REVOLVED TIP AIRFOIL

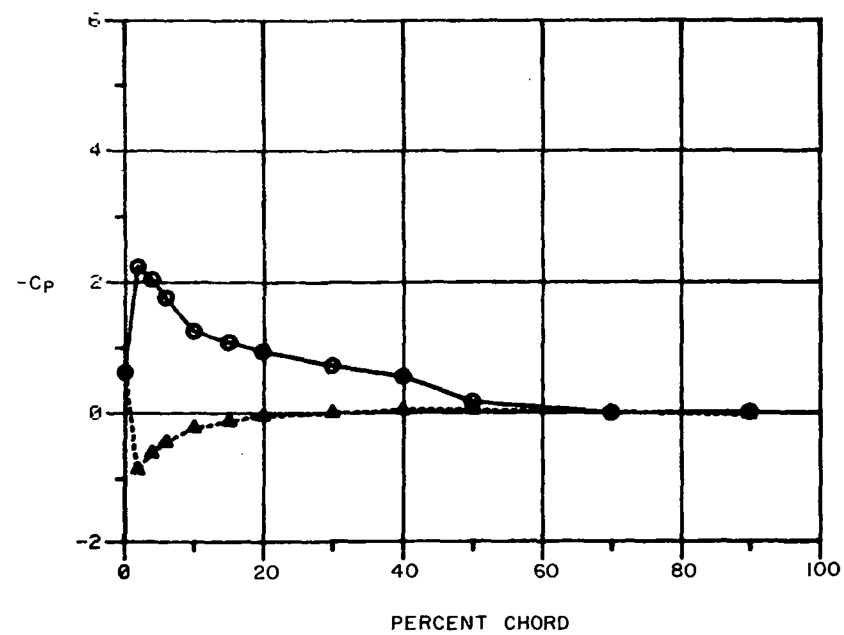

SQUARE TIP AIRFOIL

Figure 11. (Continued) Surface Pressure Coefficients, 8^{o} α, Segment 9

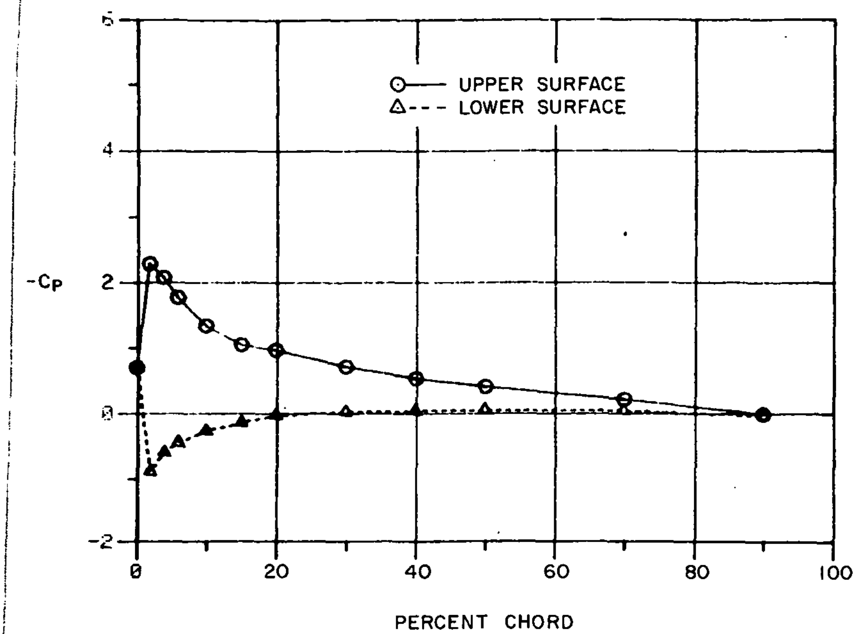

REVOLVED TIP AIRFOIL

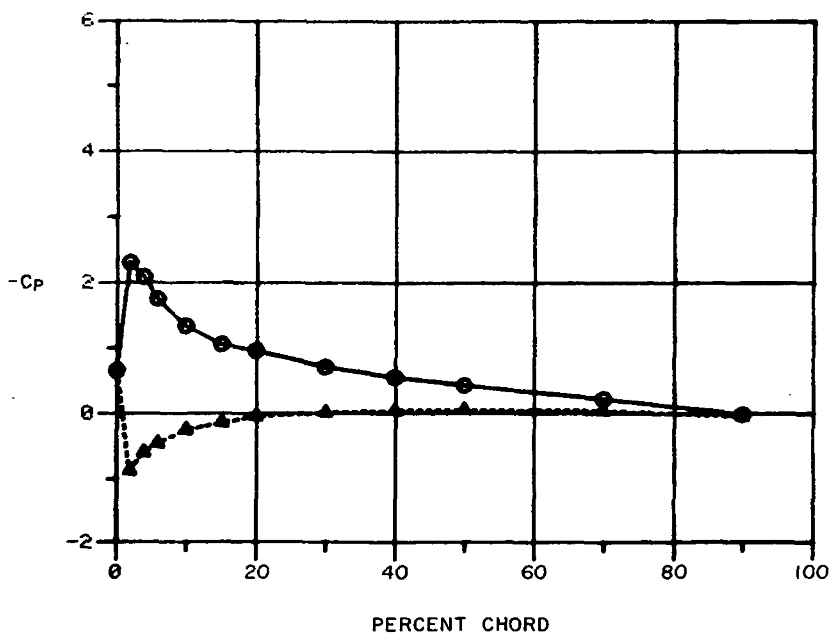

SQUARE TIP AIRFOIL

Figure 11. (Continued) Surface Pressure Coefficients, 8^{0} α, Segment 10

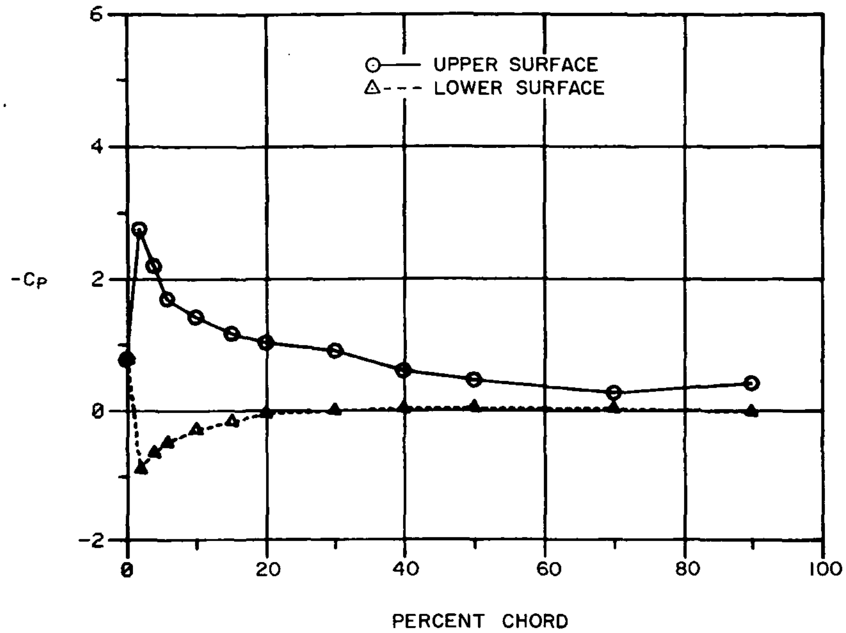

REVOLVED TIP AIRFOIL

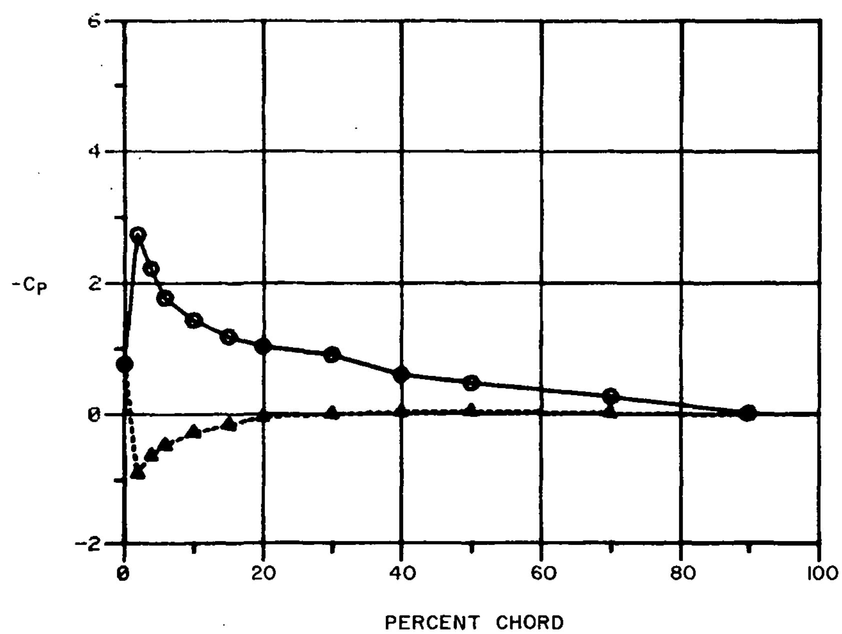

SQUARE TIP AIRFOIL

Figure 11. (Continued) Surface Pressure Coefficients, 8^0 α, Segment 11

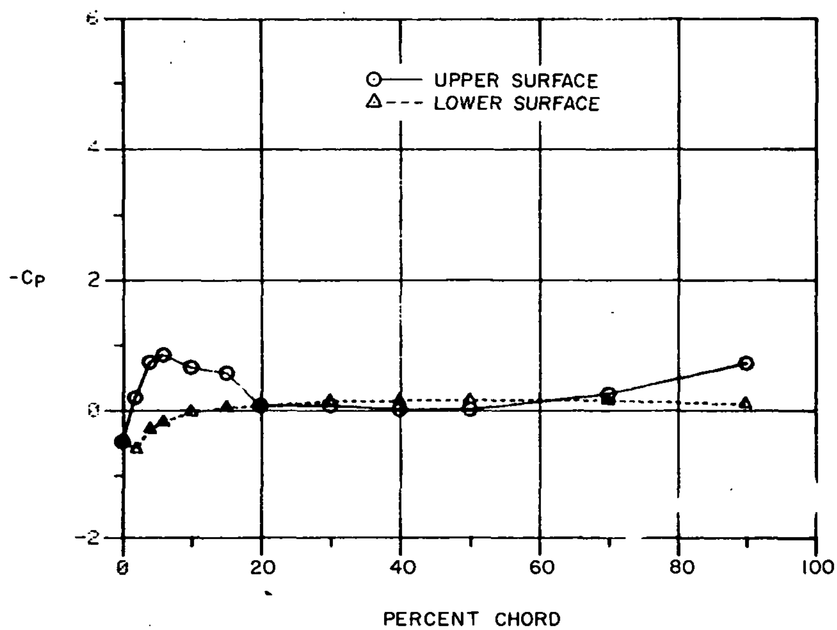

REVOLVED TIP AIRFOIL

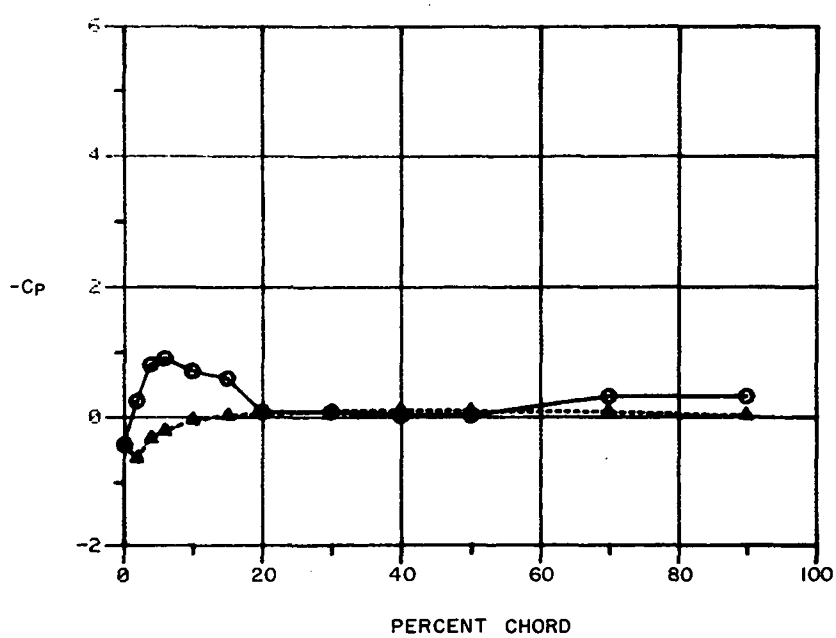

SQUARE TIP AIRFOIL

Figure 12. Surface Pressure Coefficients, 9^{o} α, Segment 1

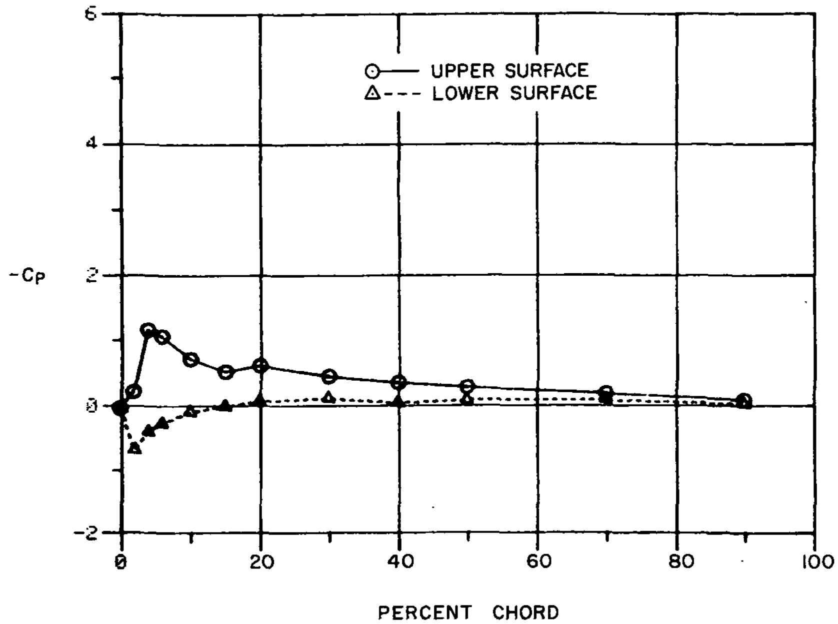

REVOLVED TIP AIRFOIL

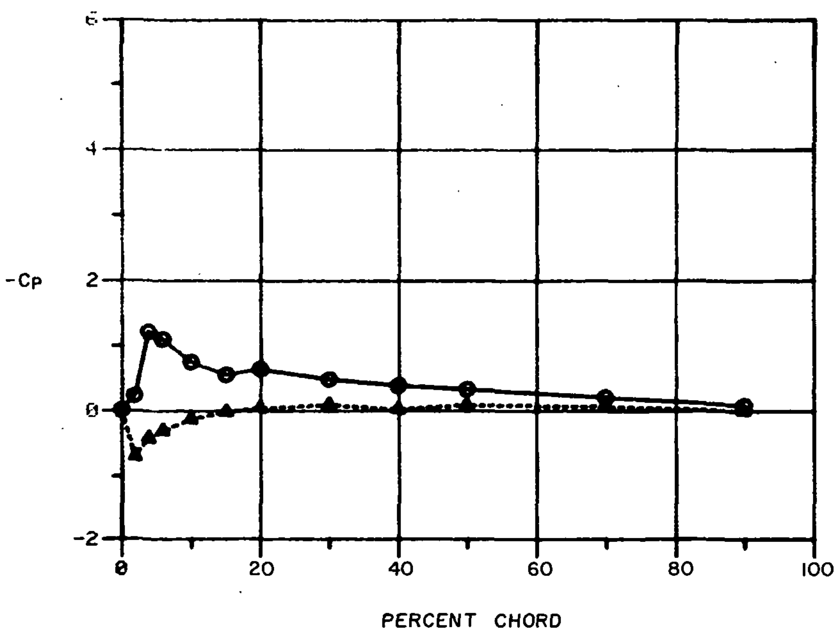

SQUARE TIP AIRFOIL

Figure 12. (Continued) Surface Pressure Coefficients, 9^{0} α, Segment 2

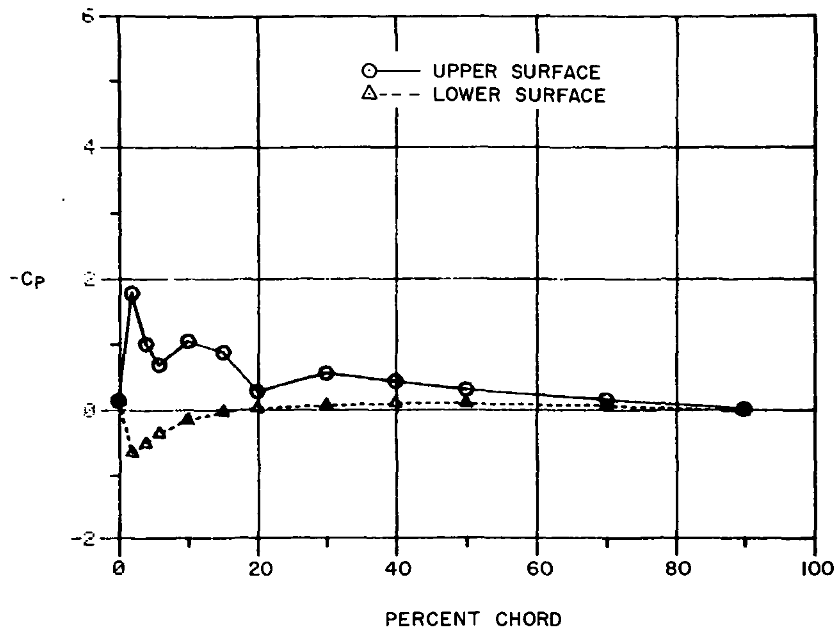

REVOLVED TIP AIRFOIL

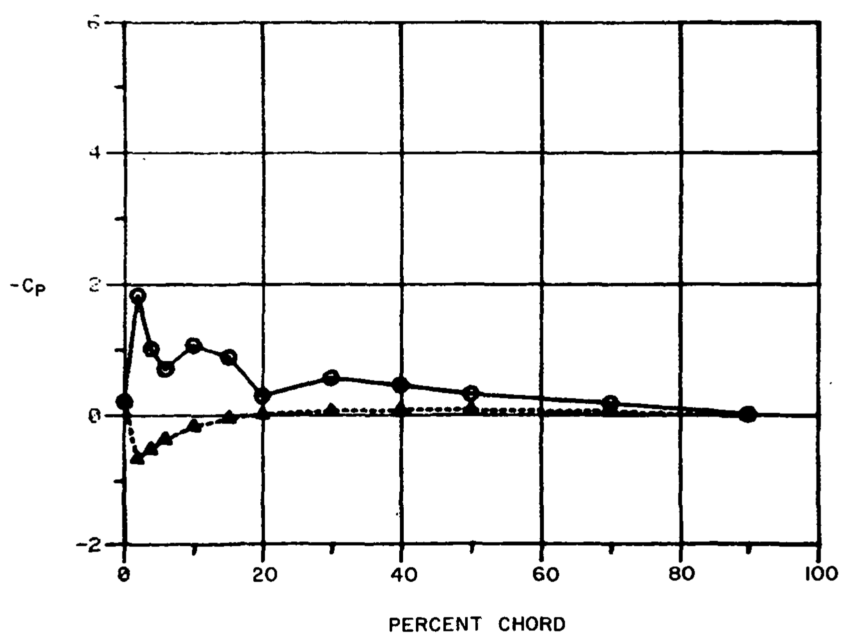

SQUARE TIP AIRFOIL

Figure 12. (Continued) Surface Pressure Coefficients, 9^{o} α, Segment 3

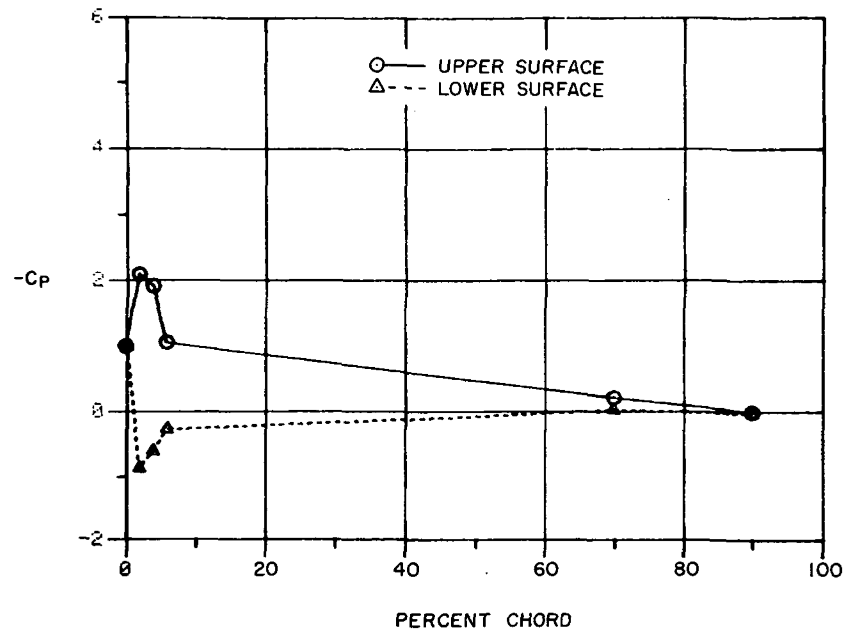

REVOLVED TIP AIRFOIL

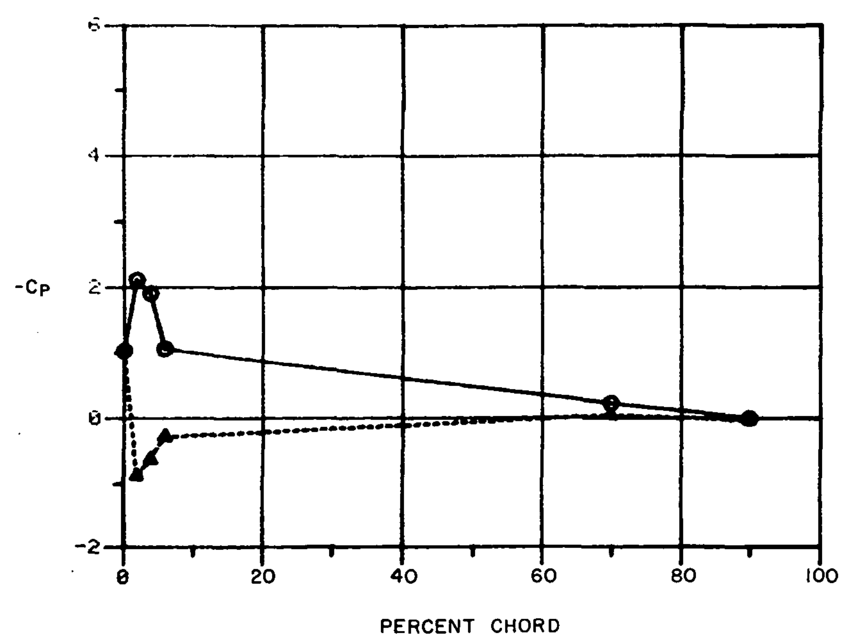

SQUARE TIP AIRFOIL

Figure 12. (Continued) Surface Pressure Coefficients, 9^{o} α, Segment 4

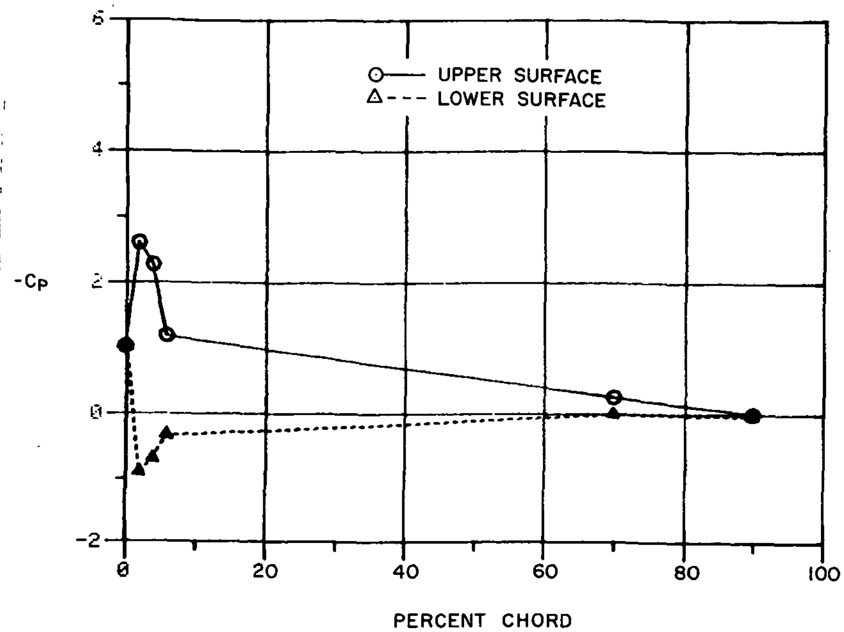

REVOLVED TIP AIRFOIL

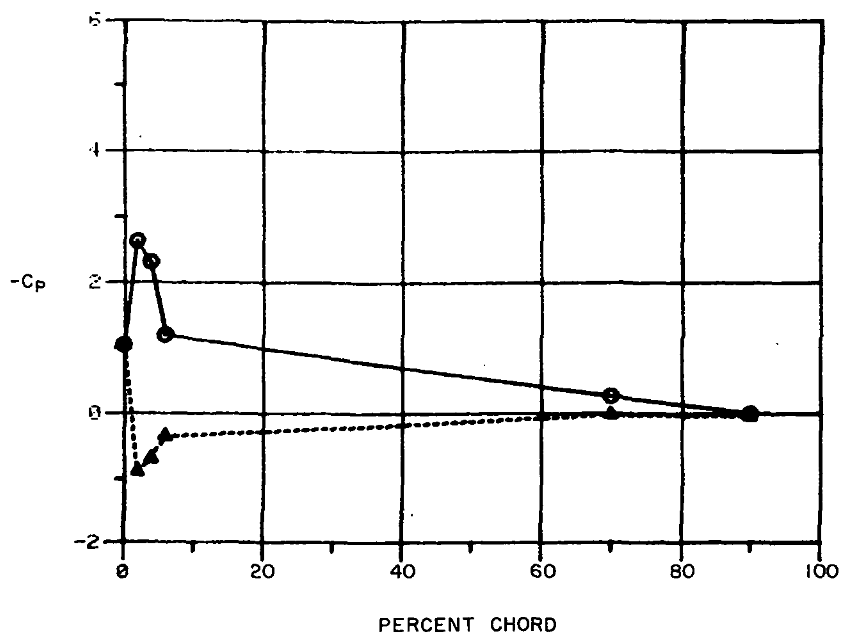

SQUARE TIP AIRFOIL

Figure 12. (Continued) Surface Pressure Coefficients, 9° α, Segment 5

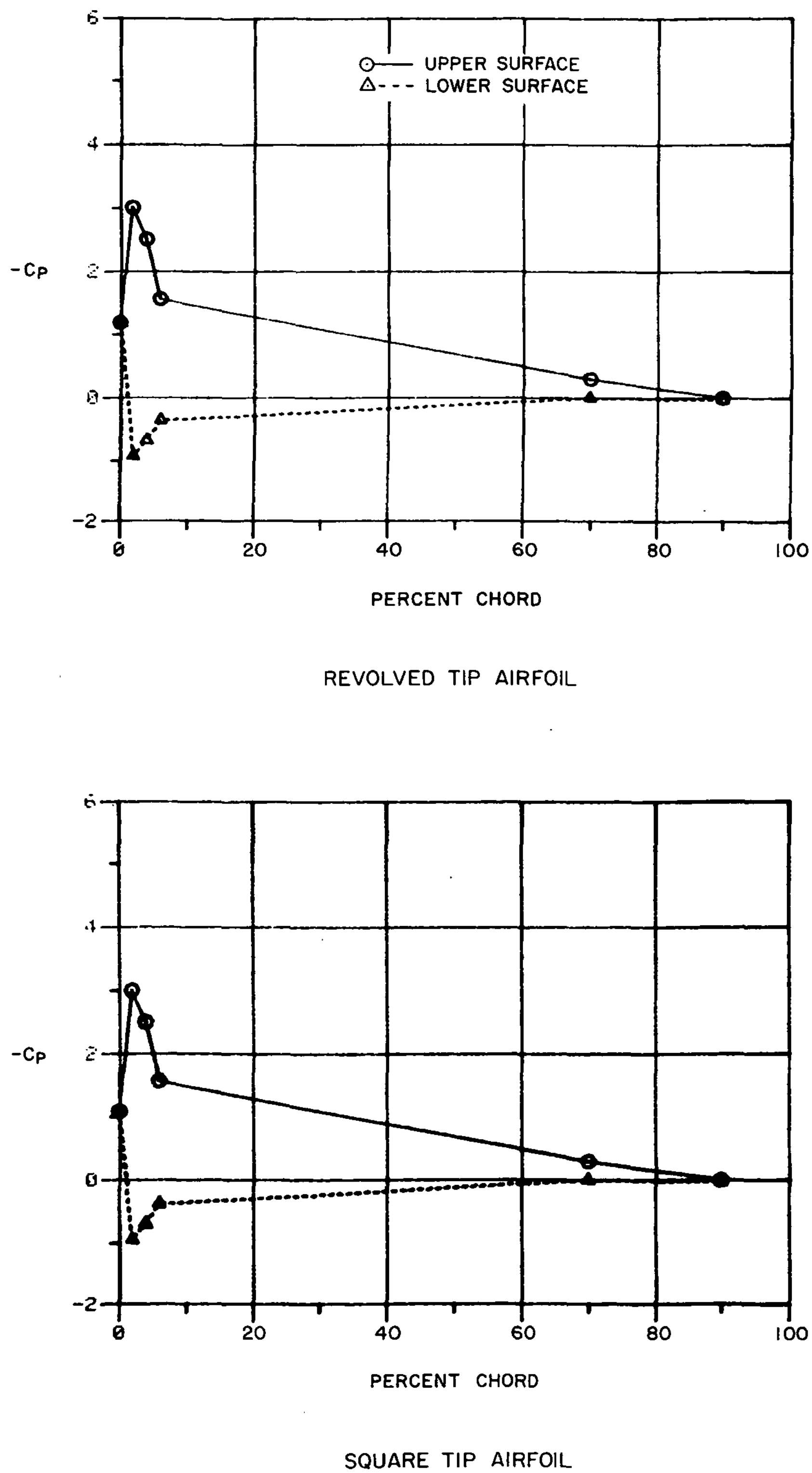

Figure 12. (Continued) Surface Pressure Coefficients, 9^0 α, Segment 6

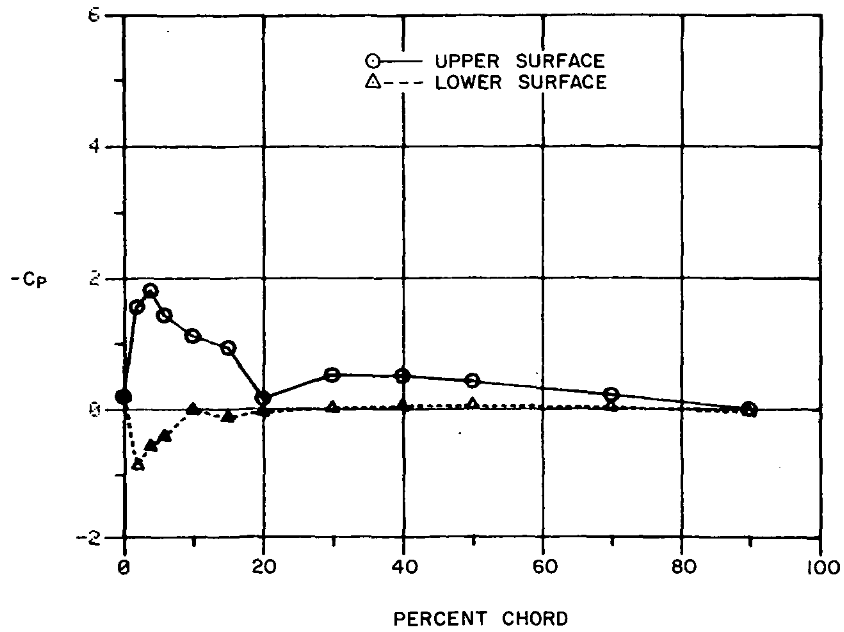

REVOLVED TIP AIRFOIL

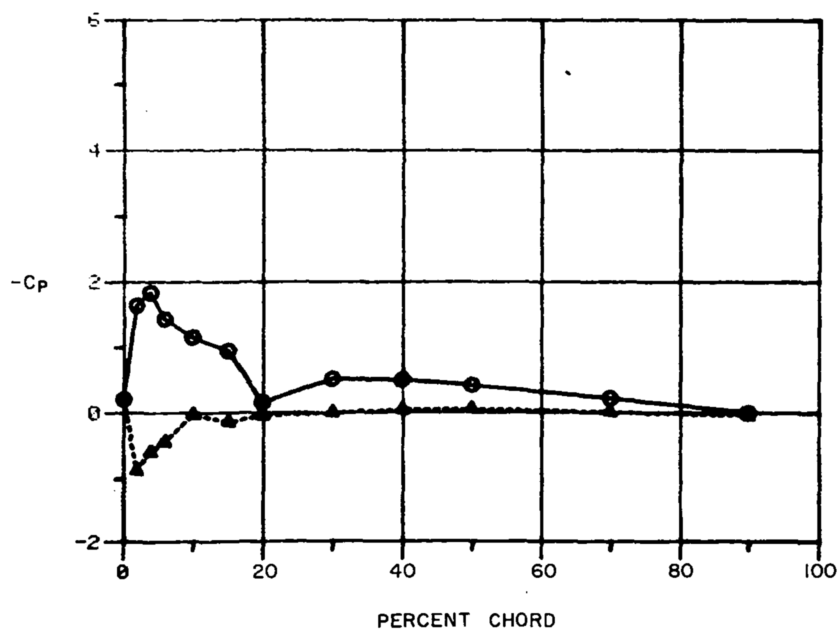

SQUARE TIP AIRFOIL

Figure 12. (Continued) Surface Pressure Coefficients, 9^{o} α, Segment 7

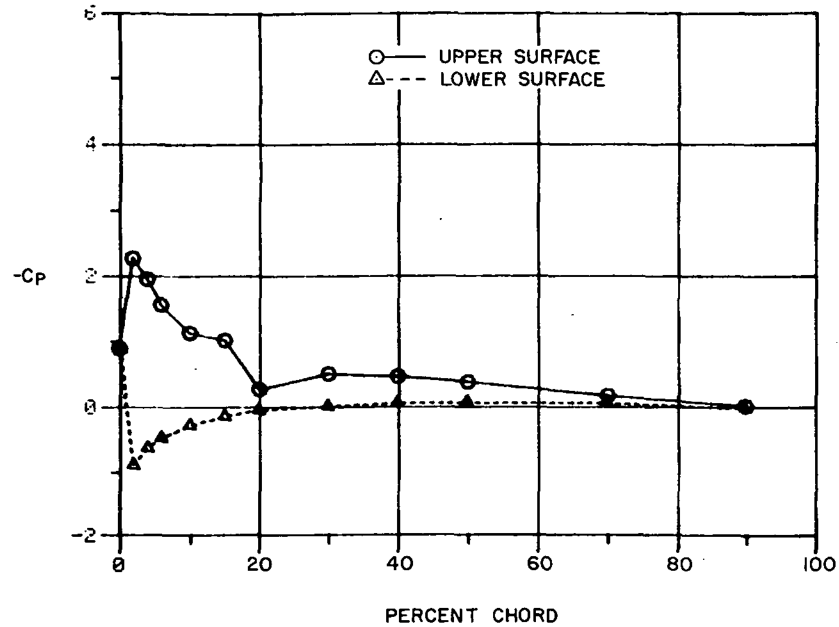

REVOLVED TIP AIRFOIL

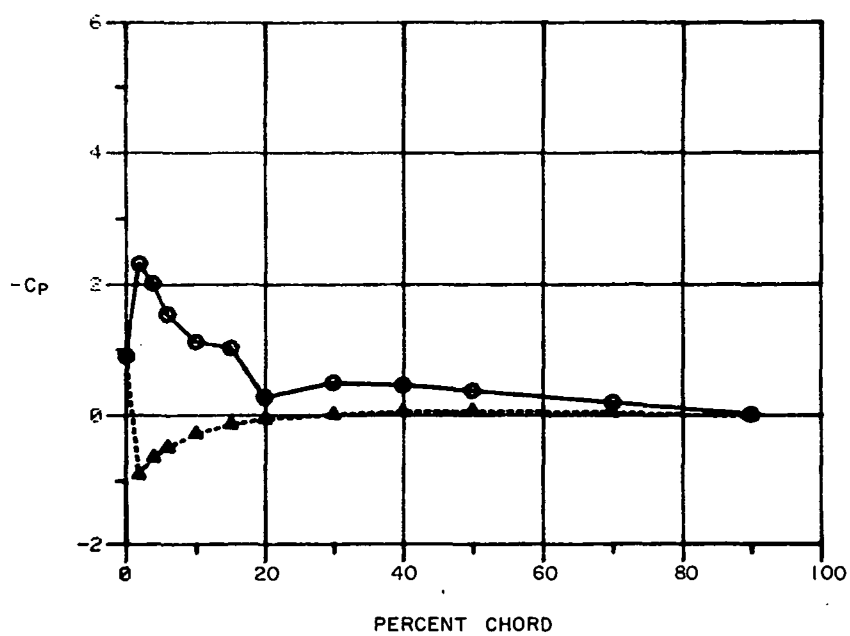

SQUARE TIP AIRFOIL

Figure 12. (Continued) Surface Pressure Coefficients, 9^{0} α, Segment 8

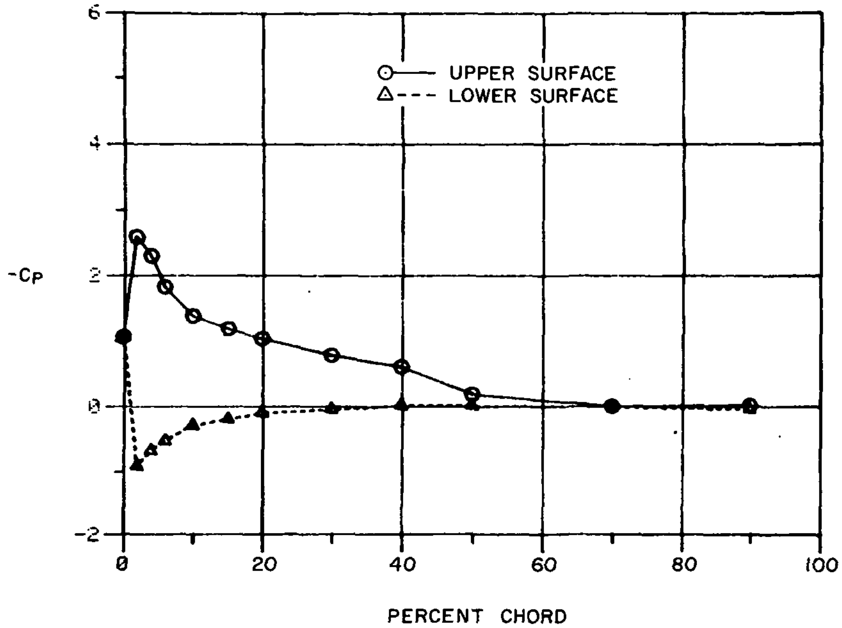

REVOLVED TIP AIRFOIL

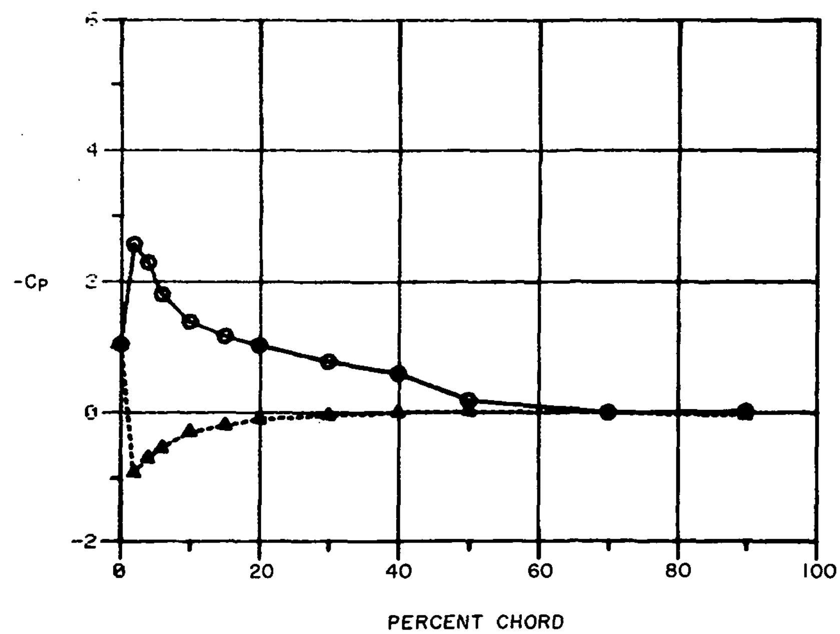

SQUARE TIP AIRFOIL

Figure 12. (Continued) Surface Pressure Coefficients, 9^o α, Segment 9

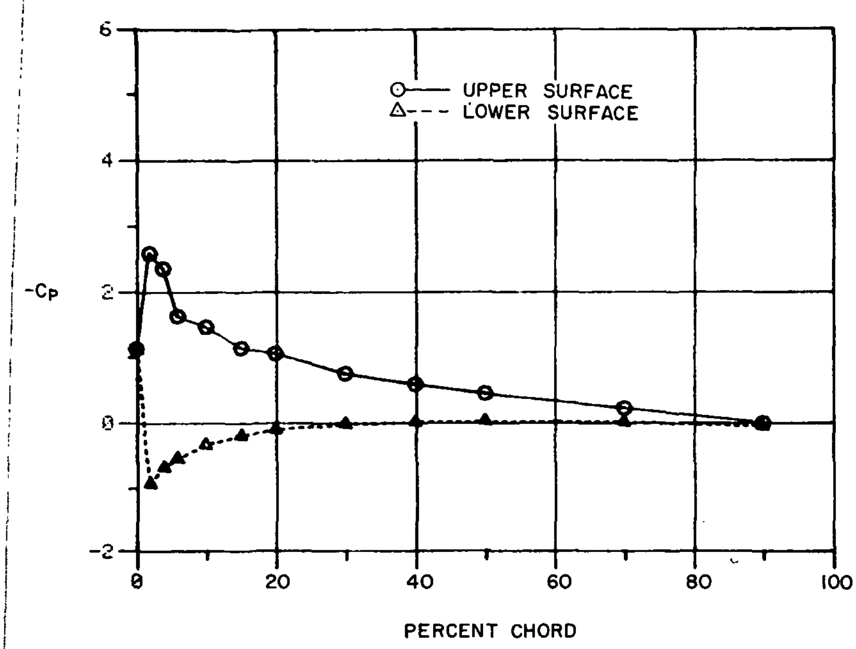

REVOLVED TIP AIRFOIL

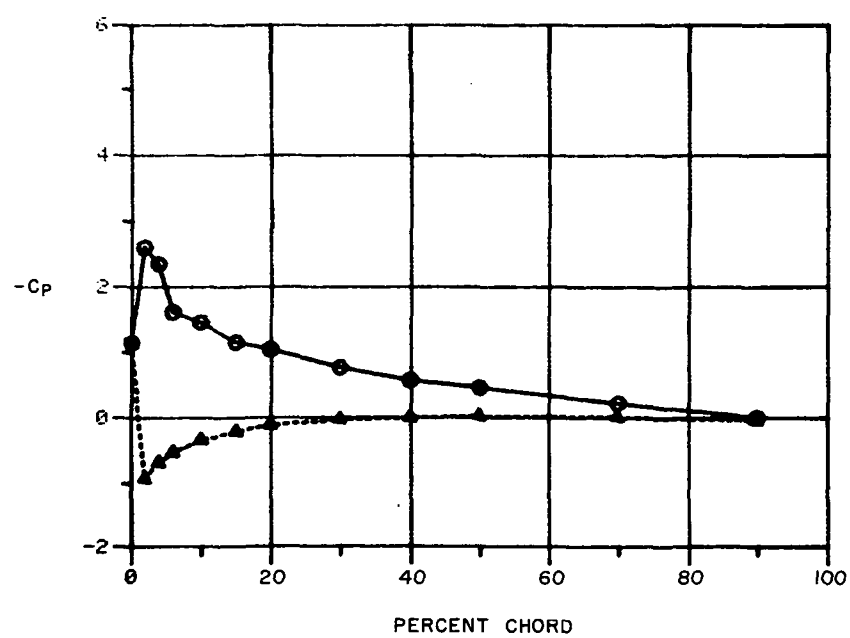

SQUARE TIP AIRFOIL

Figure 12. (Continued) Surface Pressure Coefficients, 9^{o} α, Segment 10

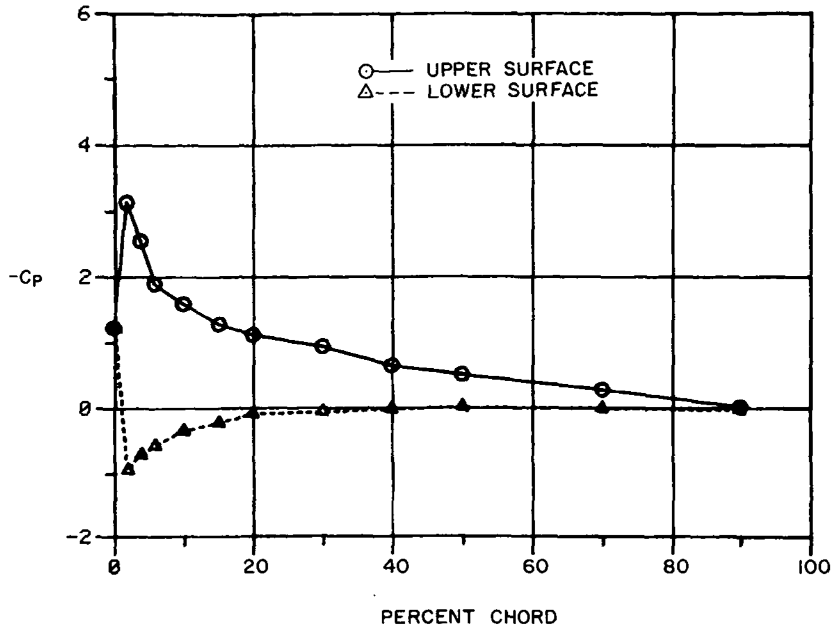

REVOLVED TIP AIRFOIL

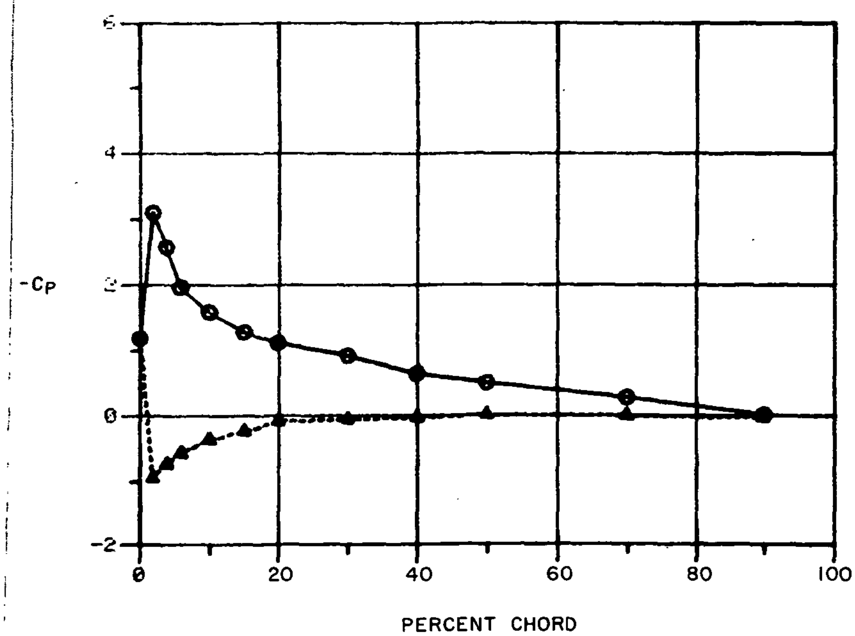

SQUARE TIP AIRFOIL

Figure 12. (Continued) Surface Pressure Coefficients, 9^{o} α, Segment 11

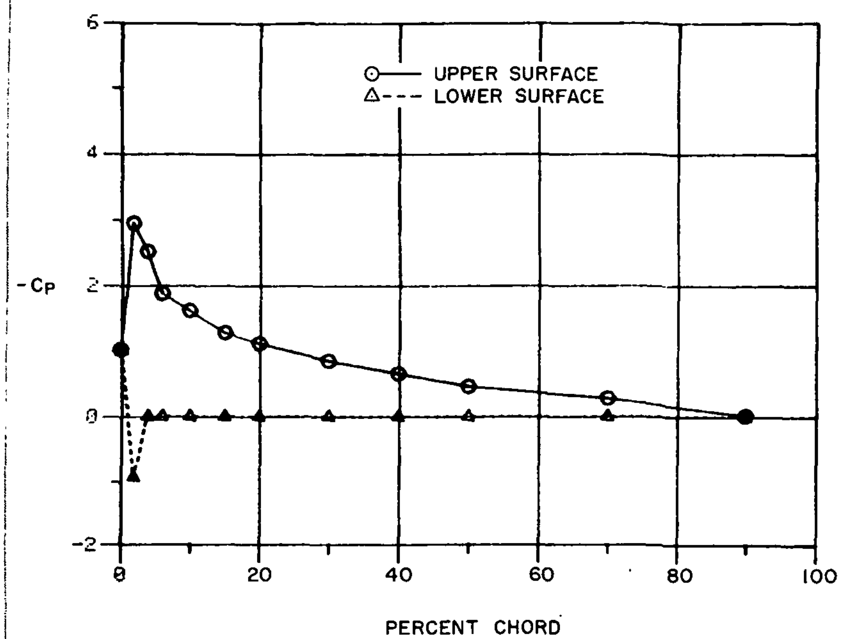

REVOLVED TIP AIRFOIL

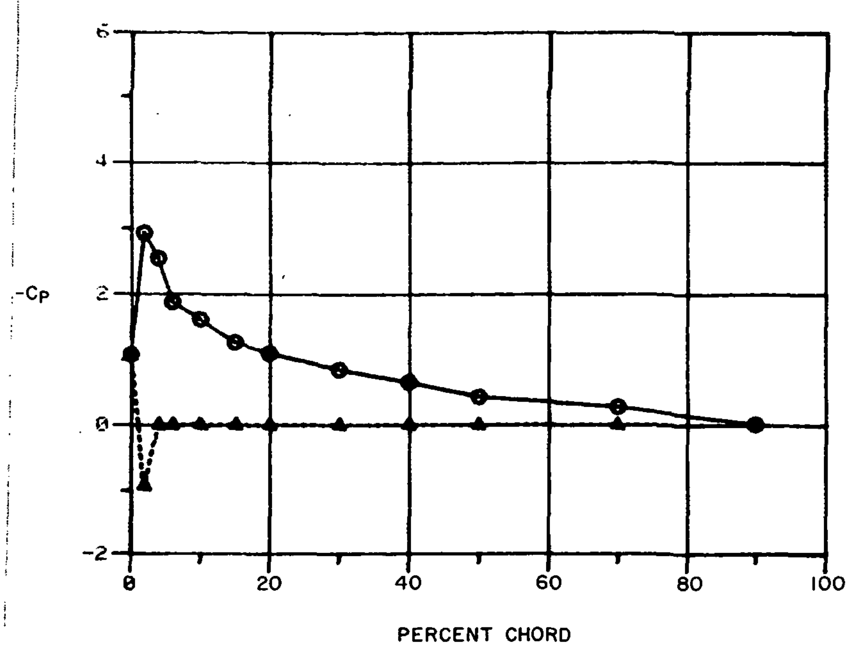

SQUARE TIP AIRFOIL

Figure 12. (Concluded) Surface Pressure Coefficients, 9^{o} α, Segment 12

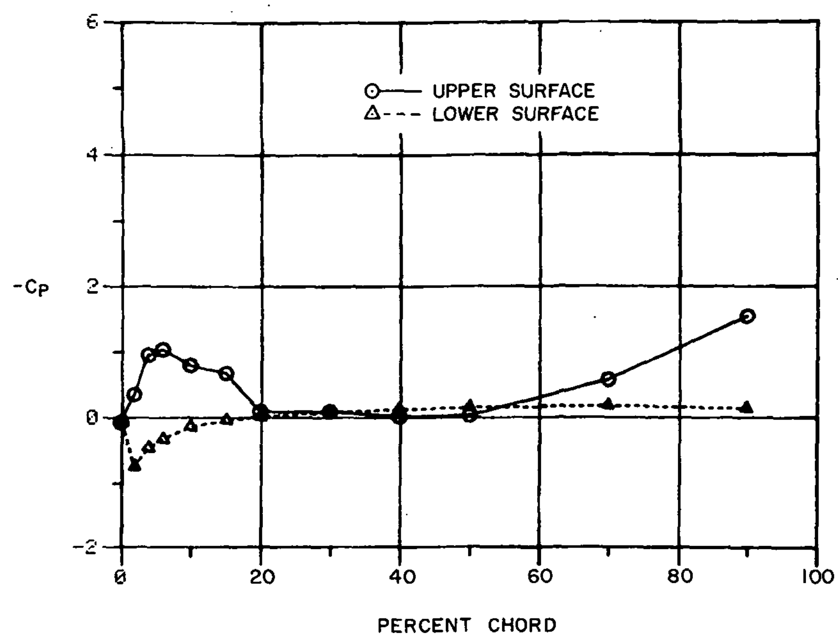

REVOLVED TIP AIRFOIL

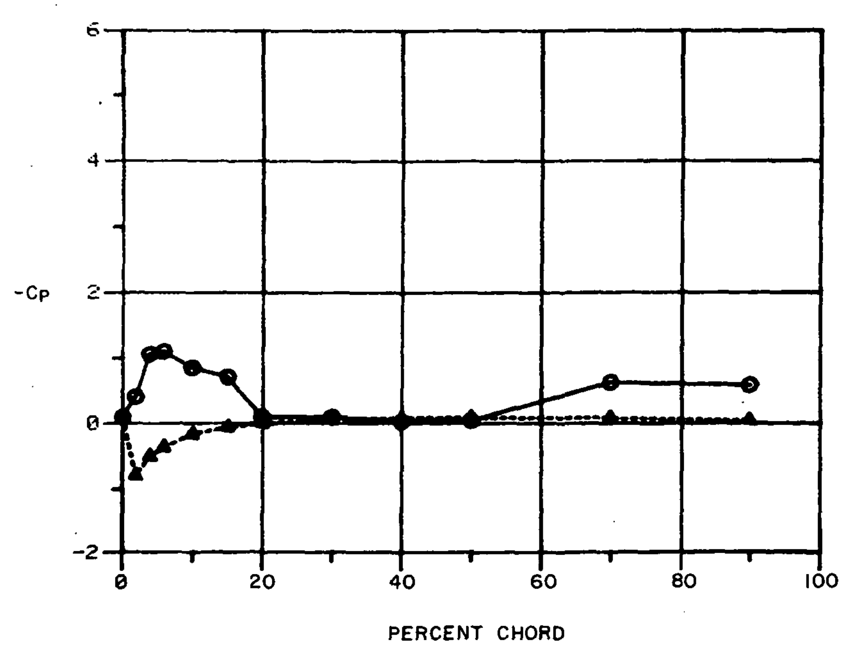

SQUARE TIP AIRFOIL

Figure 13. Surface Pressure Coefficients, 12^{o} α, Segment 1

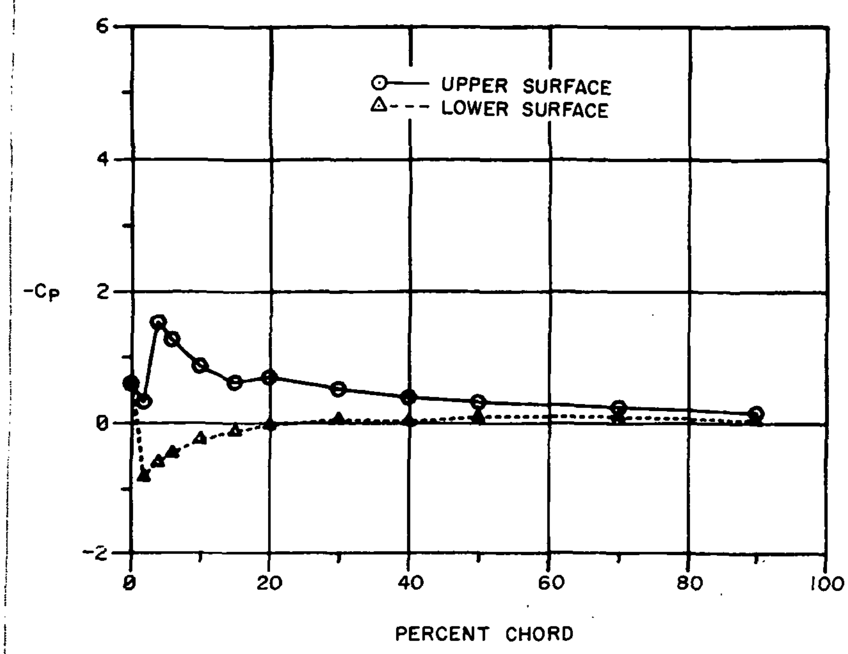

REVOLVED TIP AIRFOIL

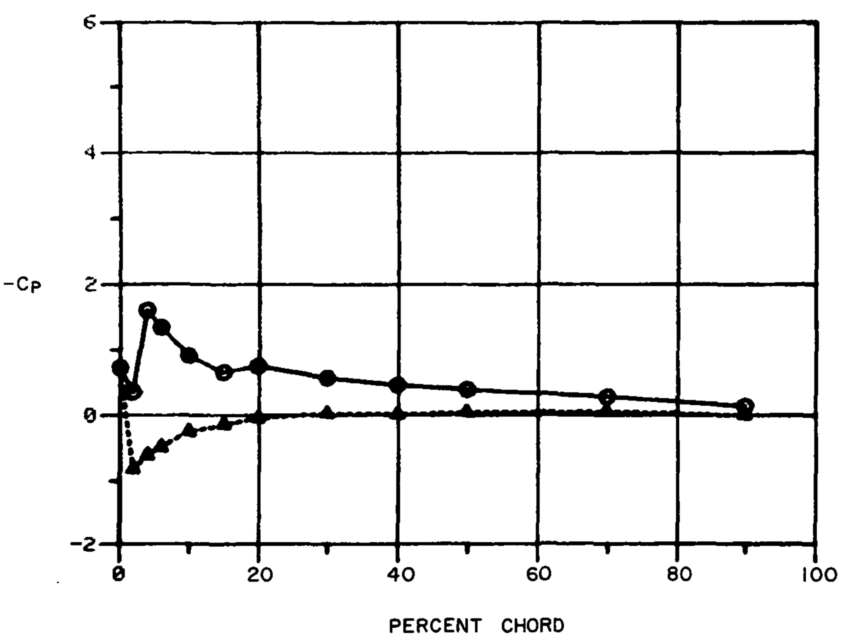

SQUARE TIP AIRFOIL

Figure 13. (Continued) Surface Pressure Coefficients, 12^{o} α, Segment 2

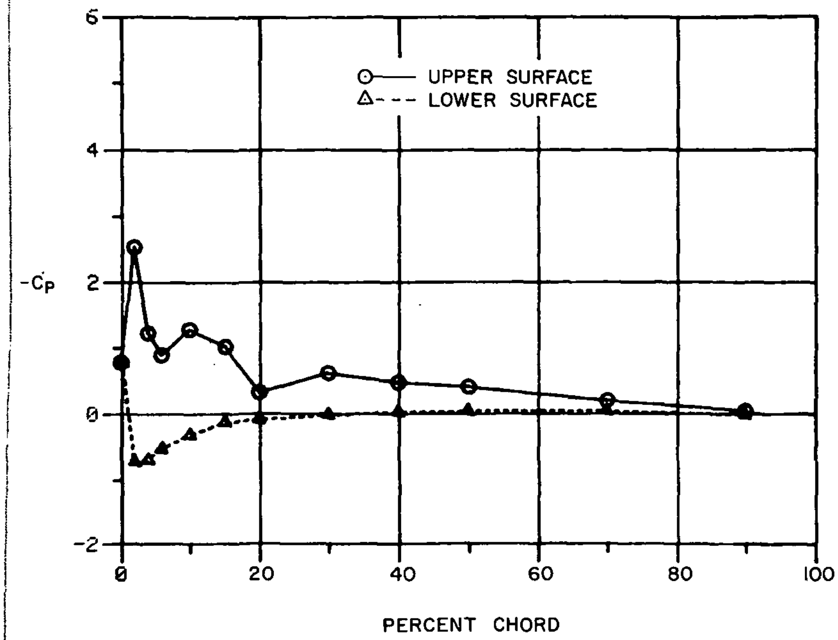

REVOLVED TIP AIRFOIL

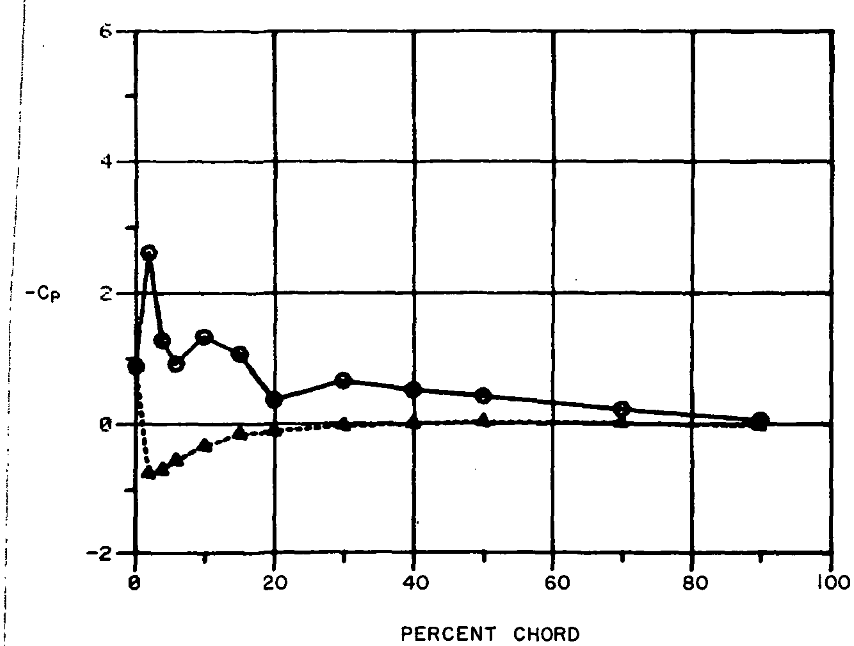

SQUARE TIP AIRFOIL

Figure 13. (Continued) Surface Pressure Coefficients, 12^{o} α, Segment 3

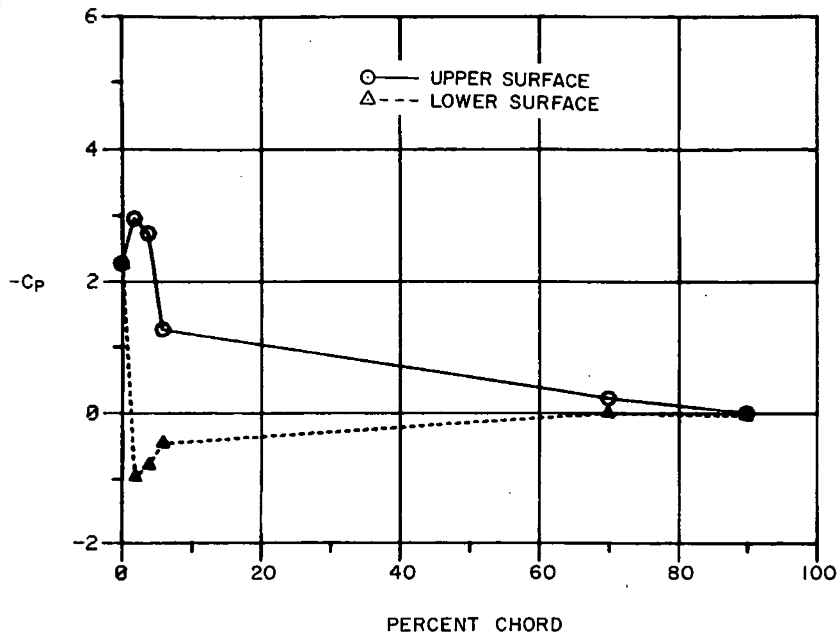

REVOLVED TIP AIRFOIL

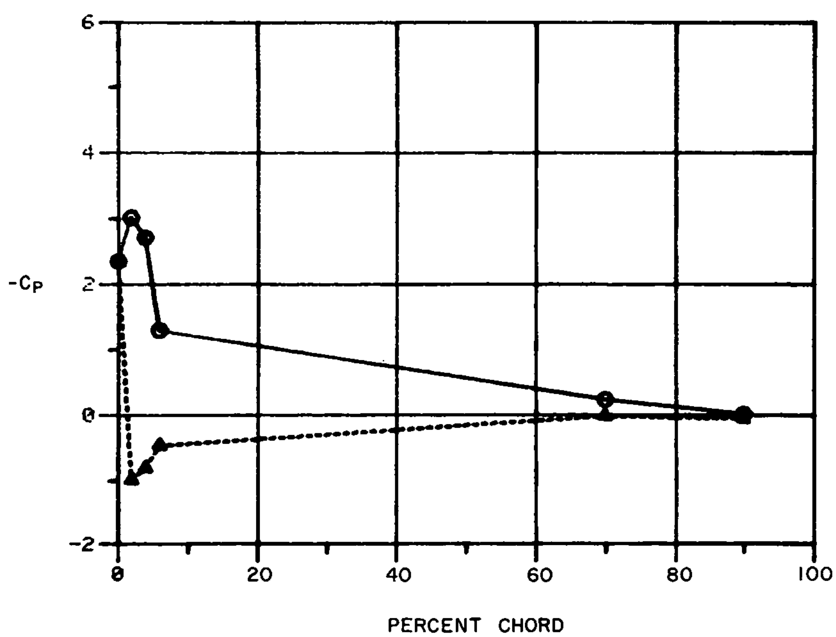

SQUARE TIP AIRFOIL

Figure 13. (Continued) Surface Pressure Coefficients, 12^{o} α, Segment 4

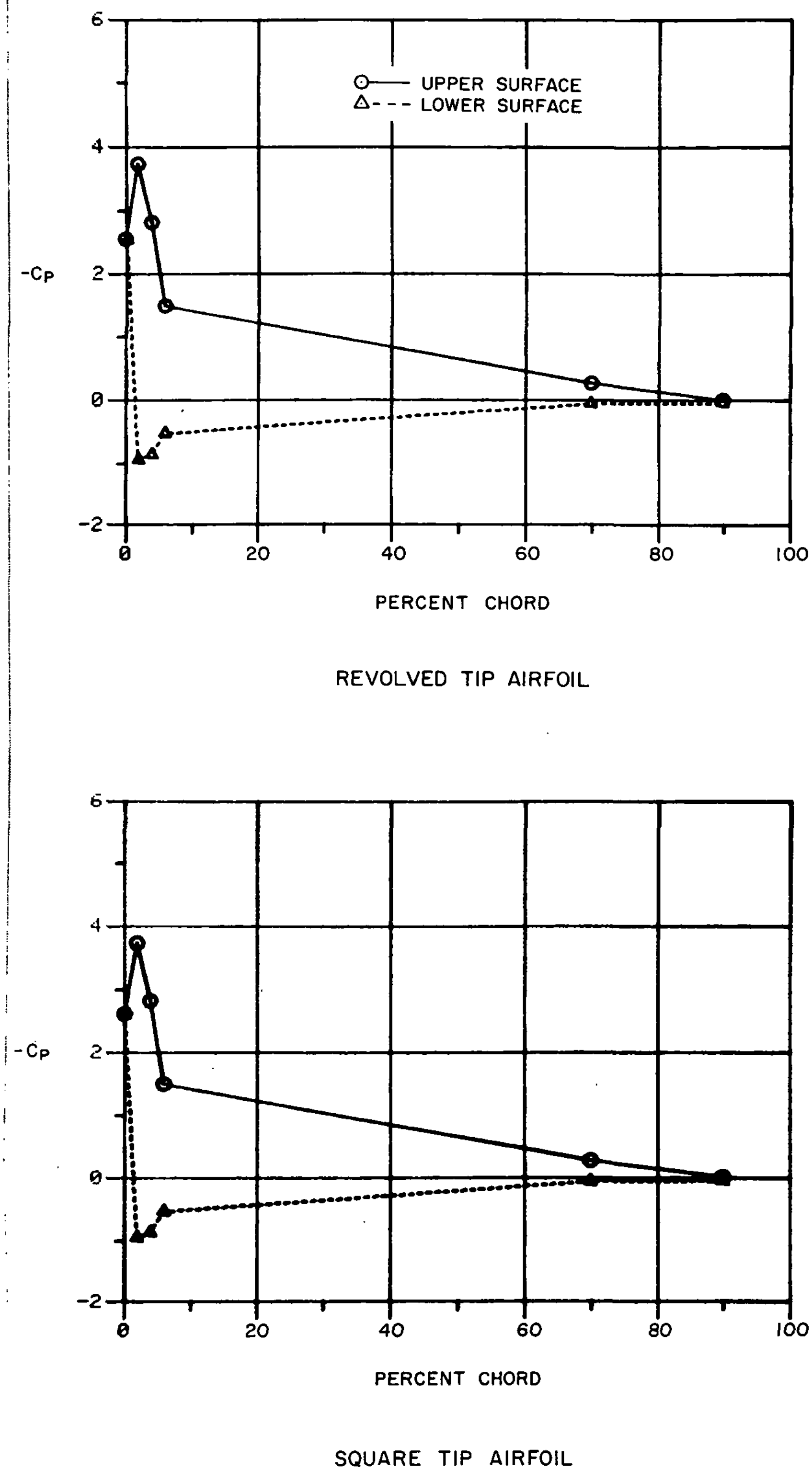

Figure 13. (Continued) Surface Pressure Coefficients, 12^{o} α, Segment 5

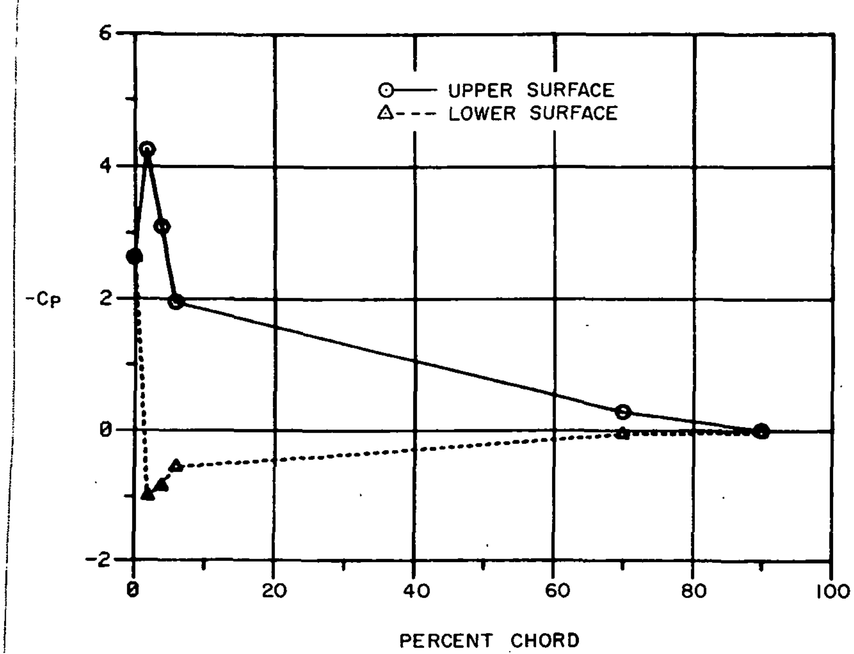

REVOLVED TIP AIRFOIL

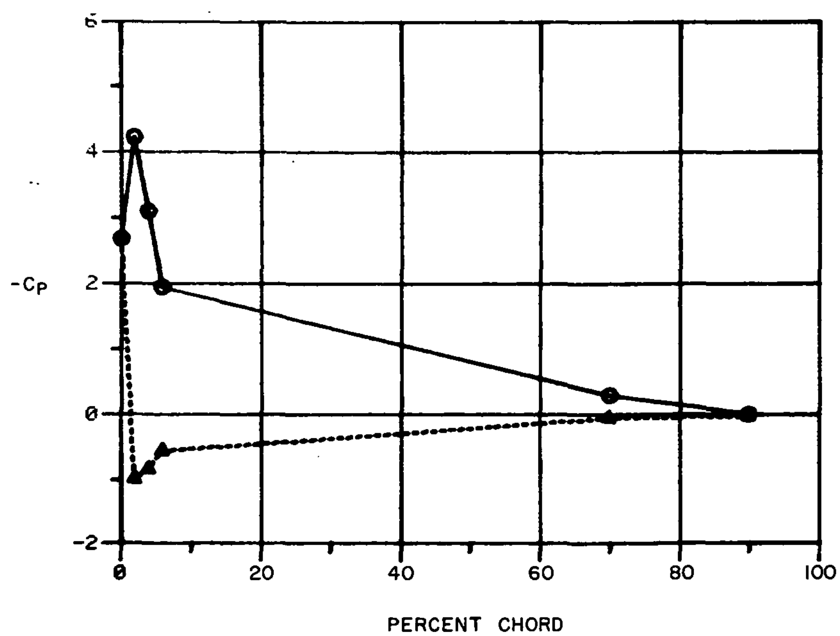

SQUARE TIP AIRFOIL

Figure 13. (Continued) Surface Pressure Coefficients, 12^{o} α, Segment 6

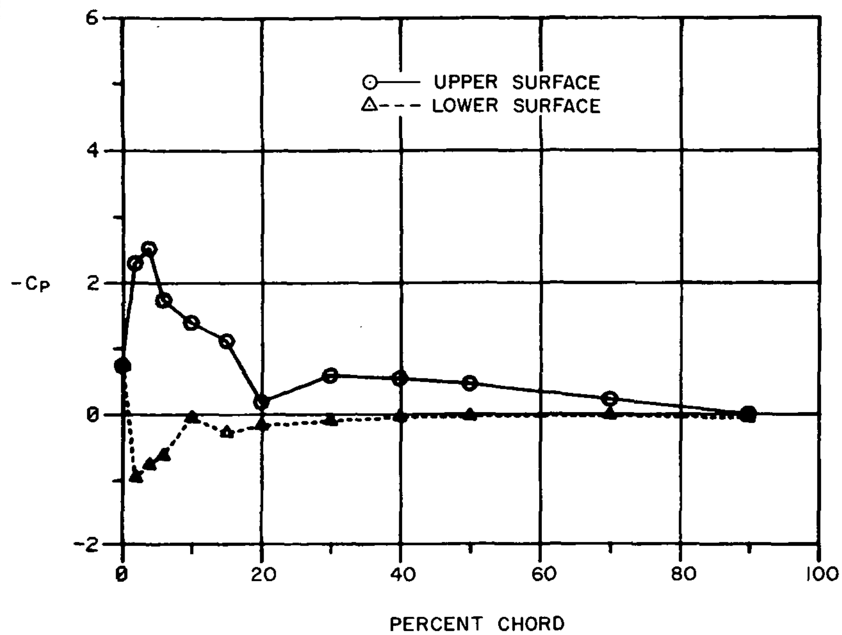

REVOLVED TIP AIRFOIL

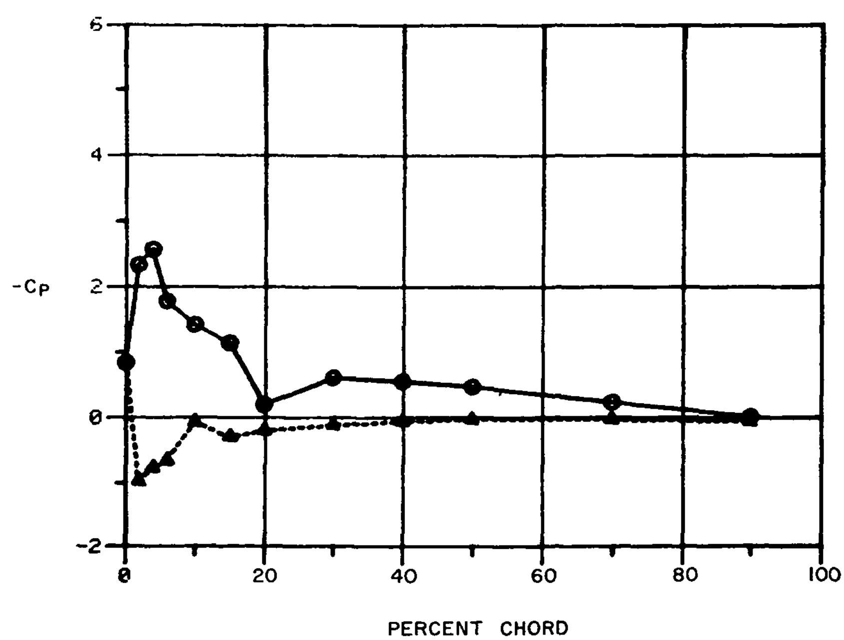

SQUARE TIP AIRFOIL

Figure 13. (Continued) Surface Pressure Coefficients, 12^{o} α, Segment 7

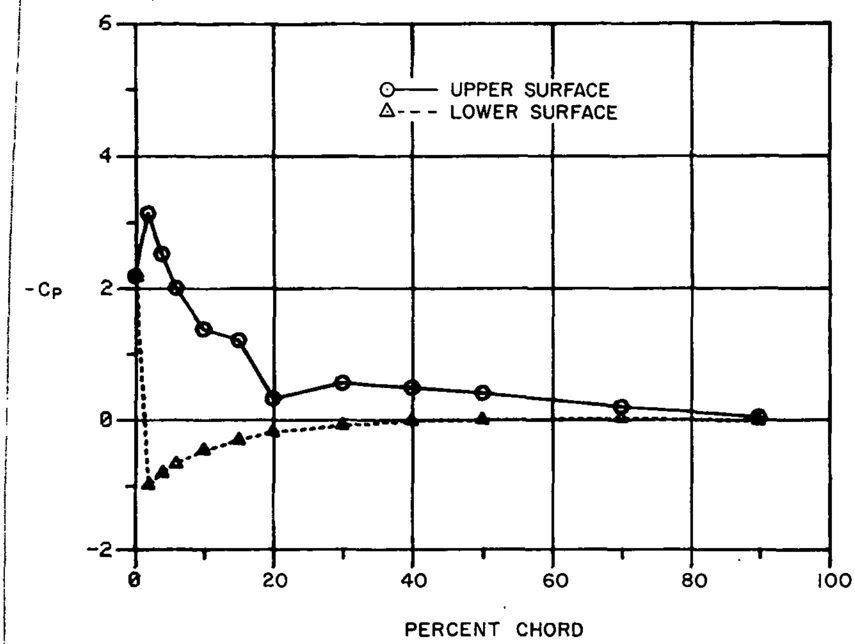

REVOLVED TIP AIRFOIL

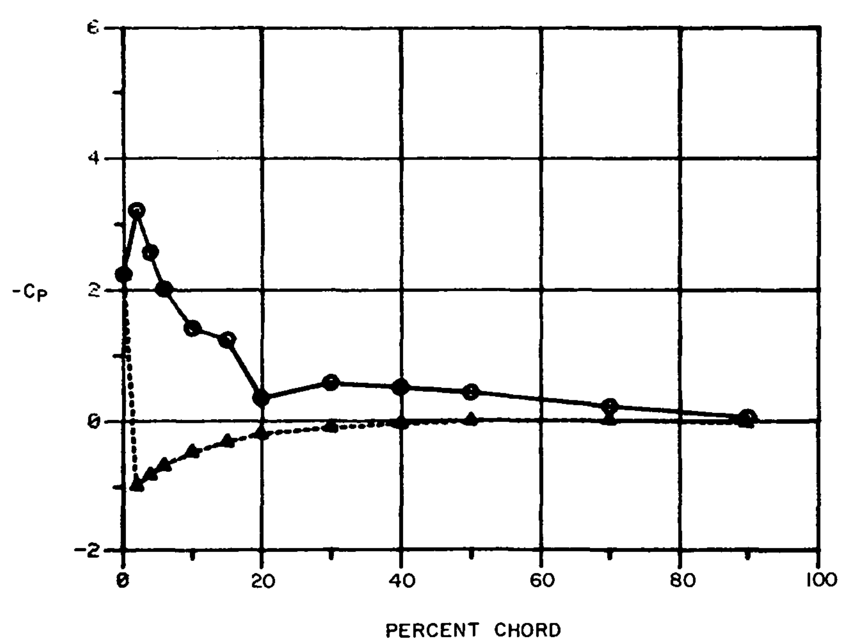

SQUARE TIP AIRFOIL

Figure 13. (Continued) Surface Pressure Coefficients, 12^{o} α, Segment 8

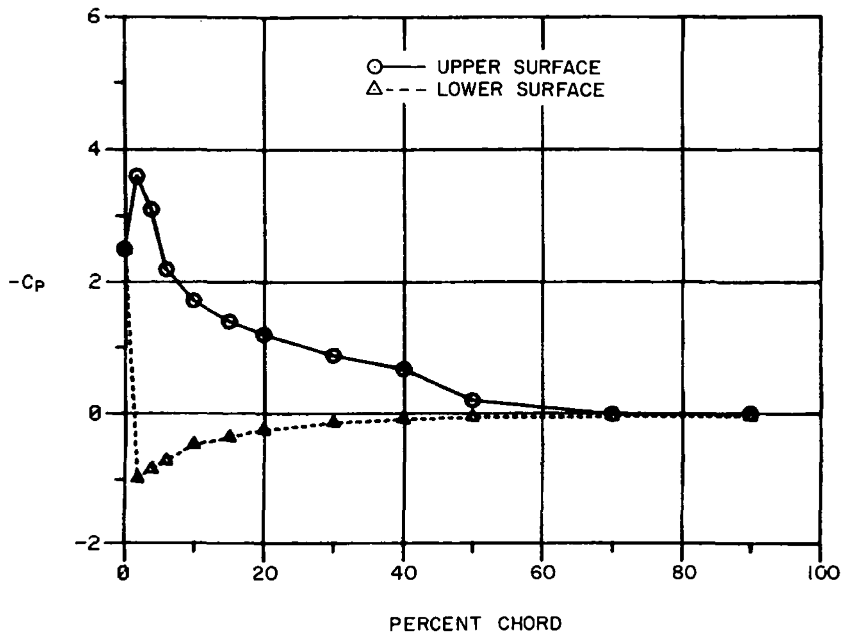

REVOLVED TIP AIRFOIL

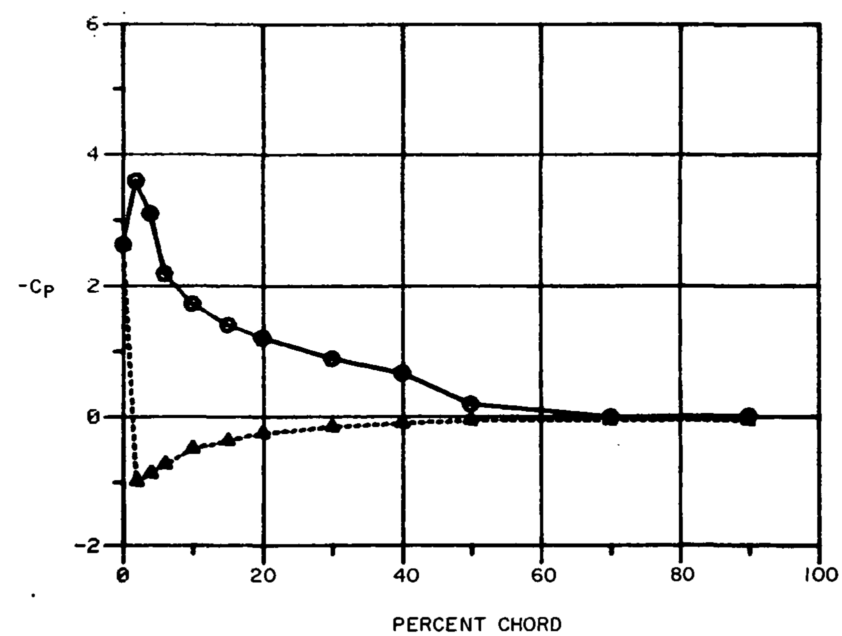

SQUARE TIP AIRFOIL

Figure 13. (Continued) Surface Pressure Coefficients, 12^{o} α, Segment 9

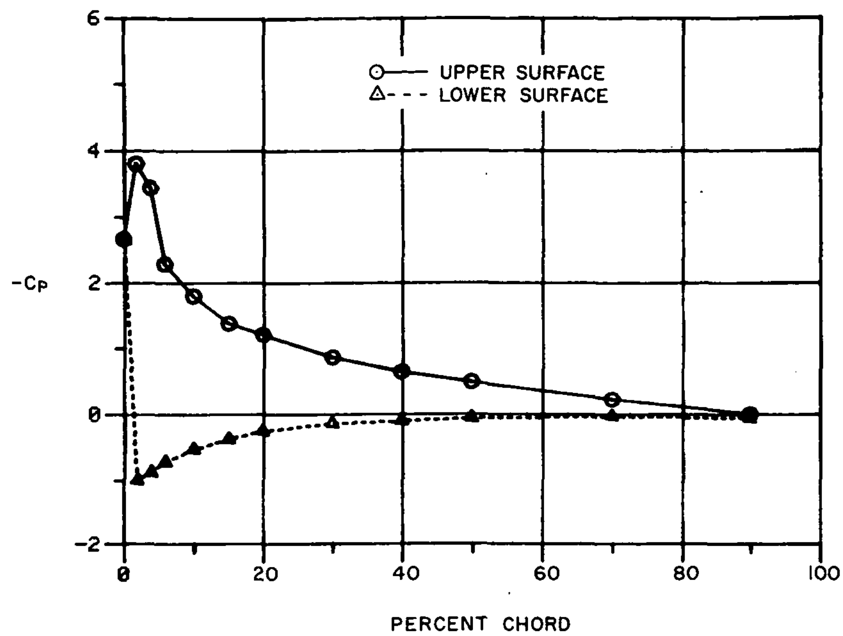

REVOLVED TIP AIRFOIL

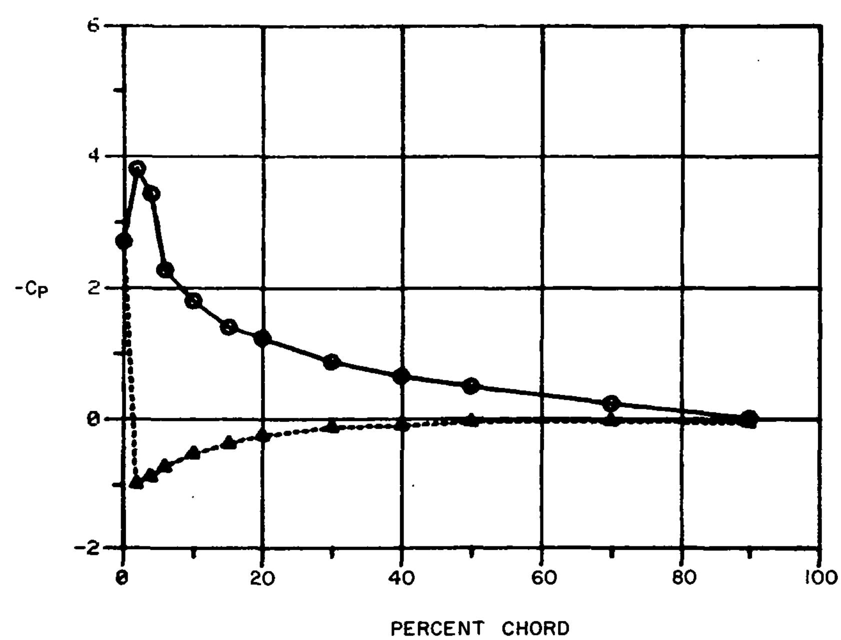

SQUARE TIP AIRFOIL

Figure 13. (Continued) Surface Pressure Coefficients, 12° α, Segment 10

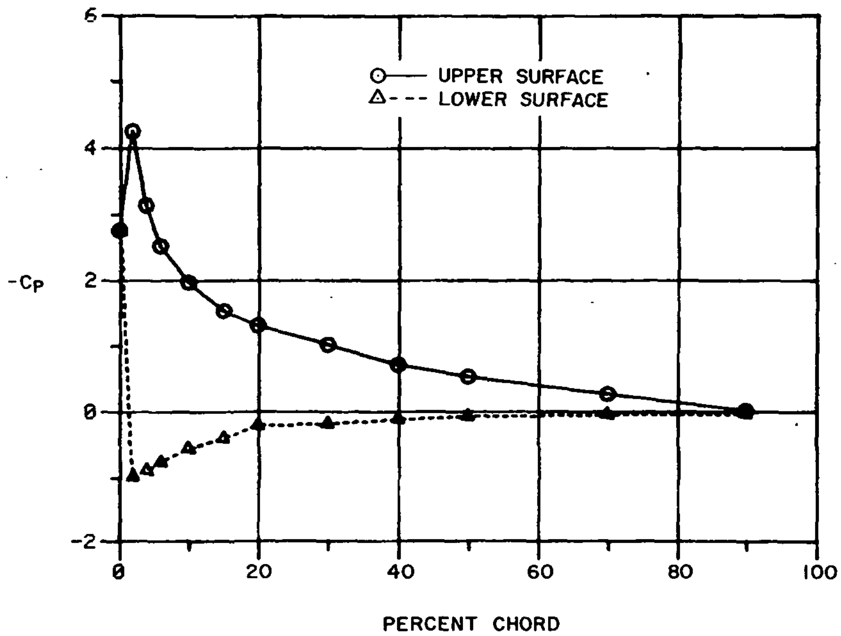

REVOLVED TIP AIRFOIL

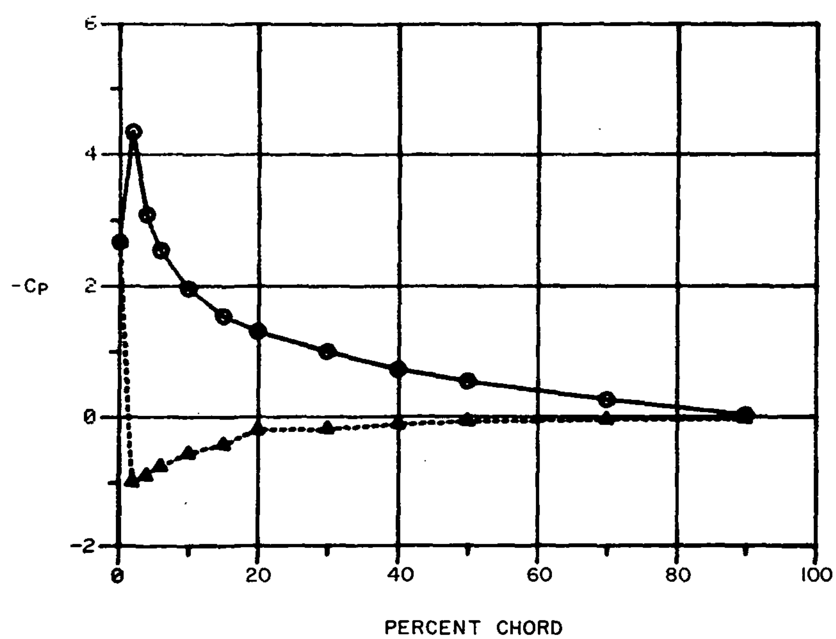

SQUARE TIP AIRFOIL

Figure 13. (Continued) Surface Pressure Coefficients, 12^{o} α, Segment 11

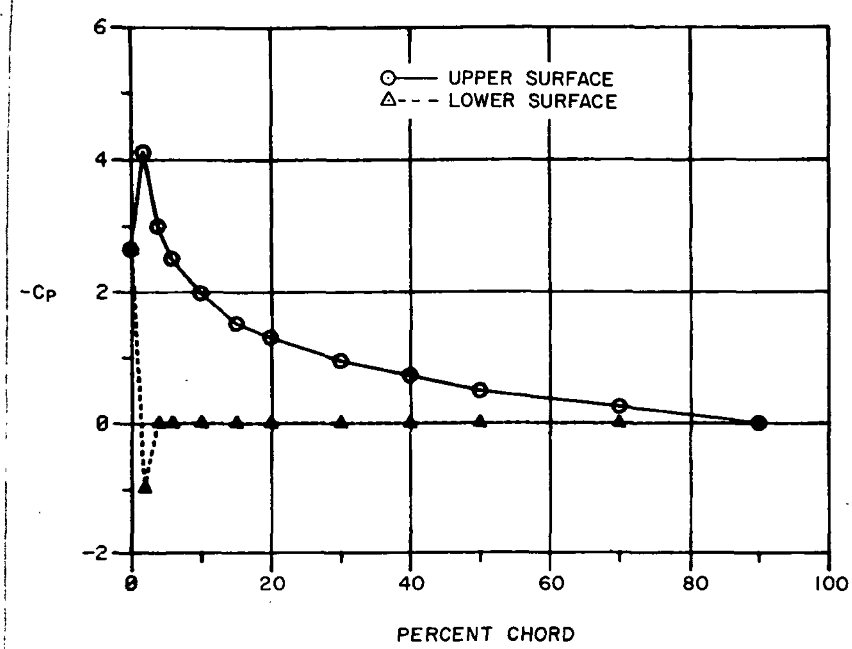

REVOLVED TIP AIRFOIL

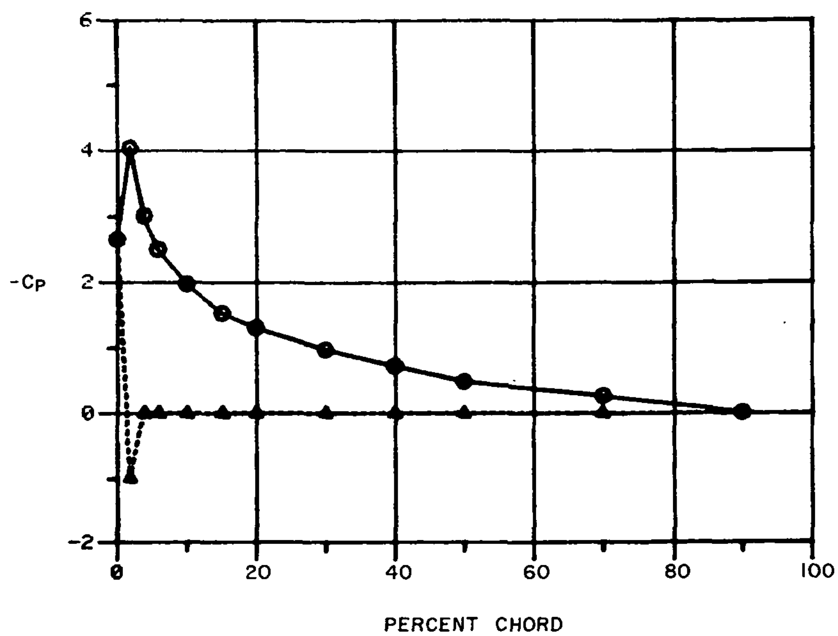

SQUARE TIP AIRFOIL

Figure 13. (Concluded) Surface Pressure Coefficients, 12^{o} α, Segment 12

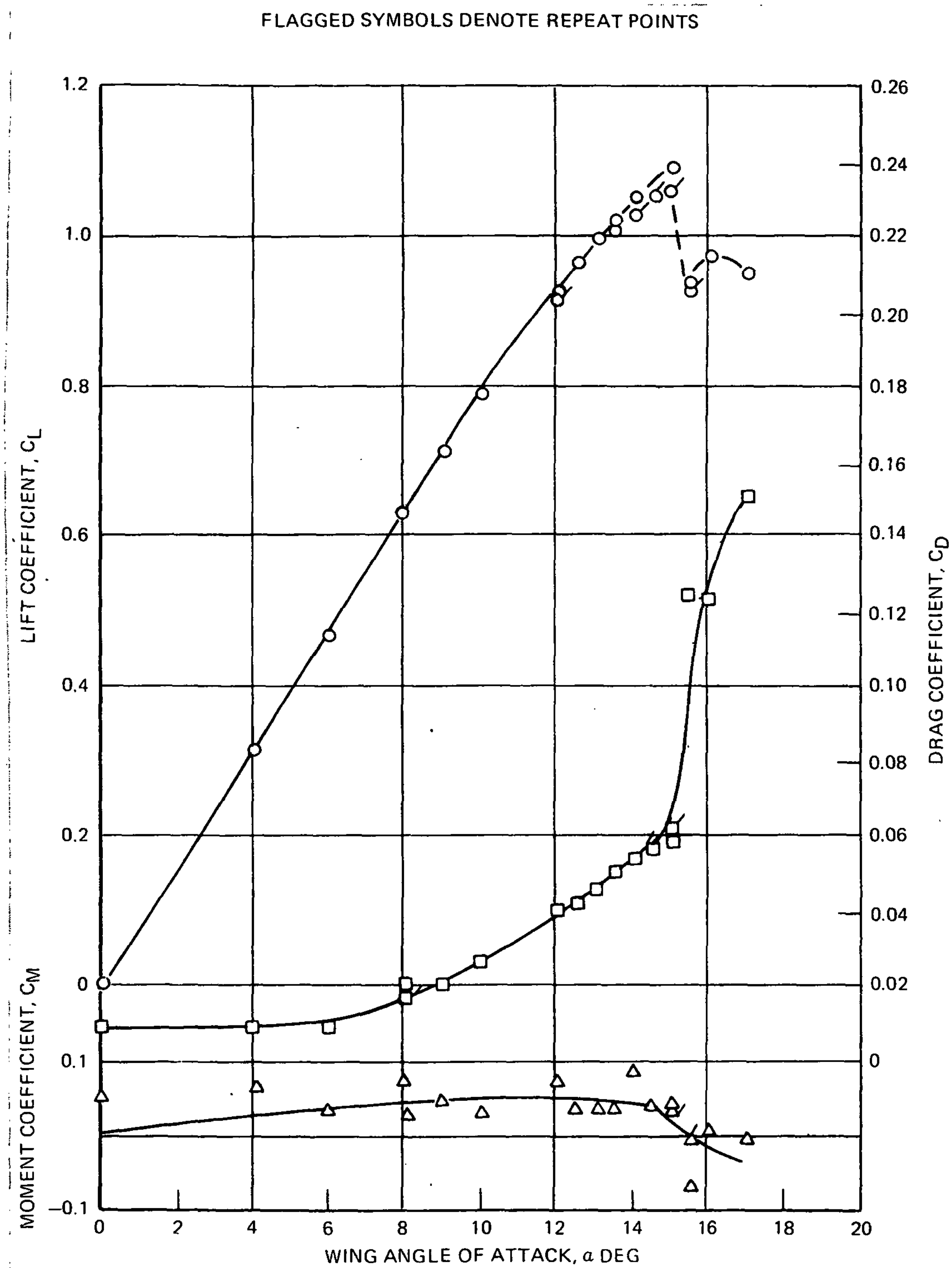

Figure 14. Lift, Drag and Pitching Moment Data for Revolved Airfoil Tip.

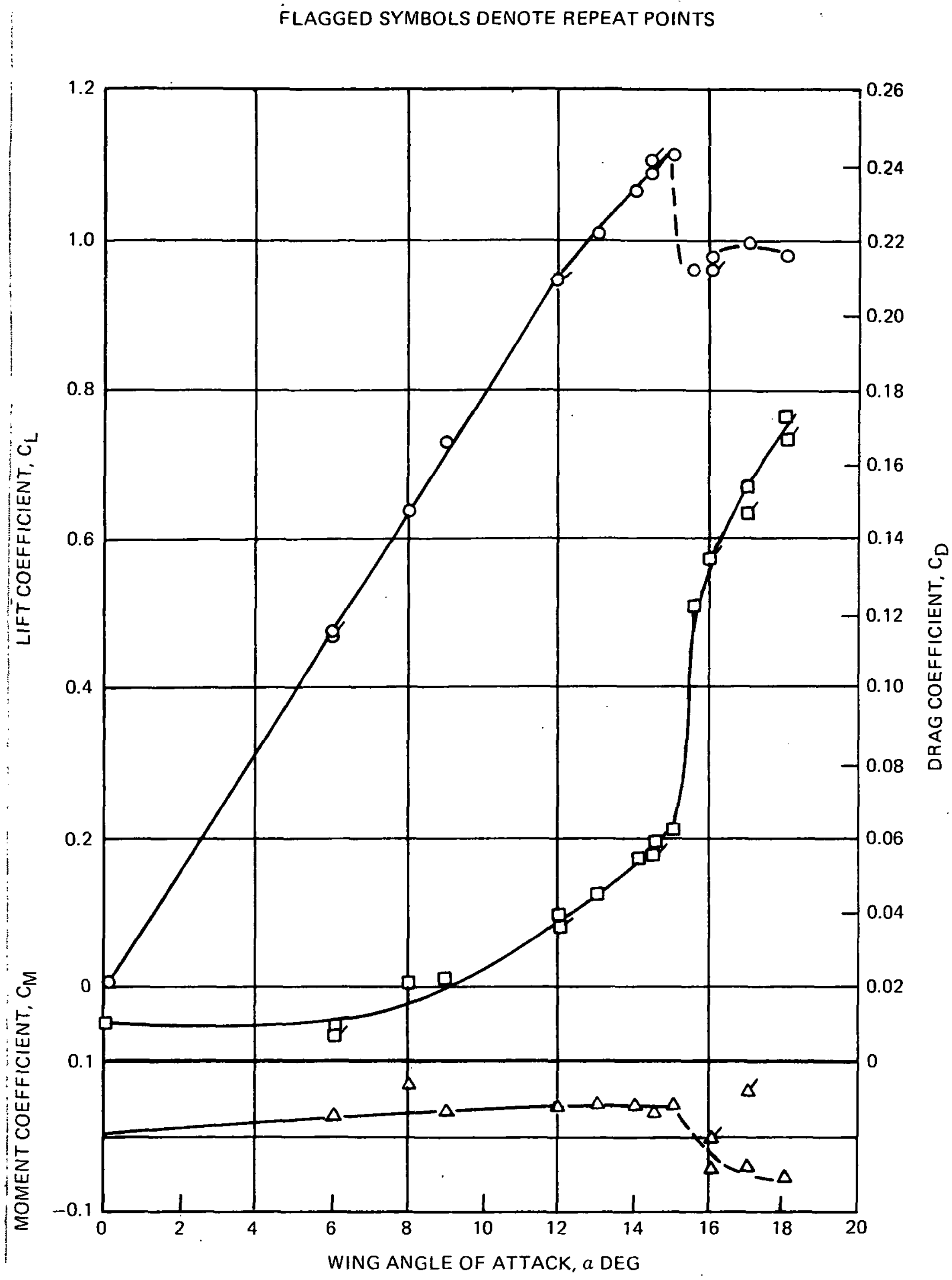

Figure 15. Lift, Drag and Pitching Moment Data for Square Tip.

FLAGGED SYMBOLS DENOTE REPEAT POINTS

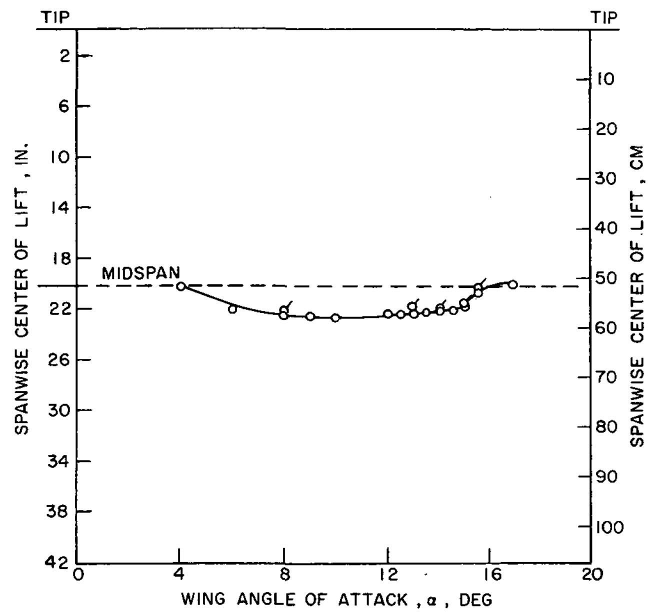

REVOLVED AIRFOIL TIP

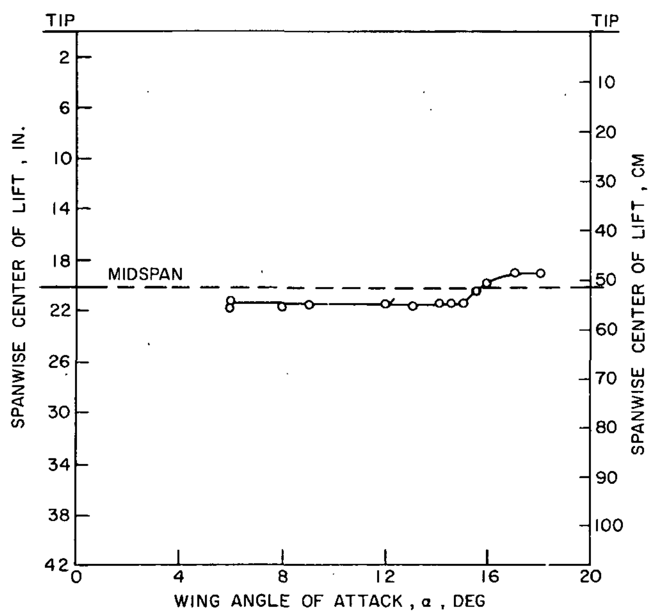

SQUARE TIP

Figure 16. Spanwise Center of Lift vs. Wing Angle.

This page intentionally left blank.

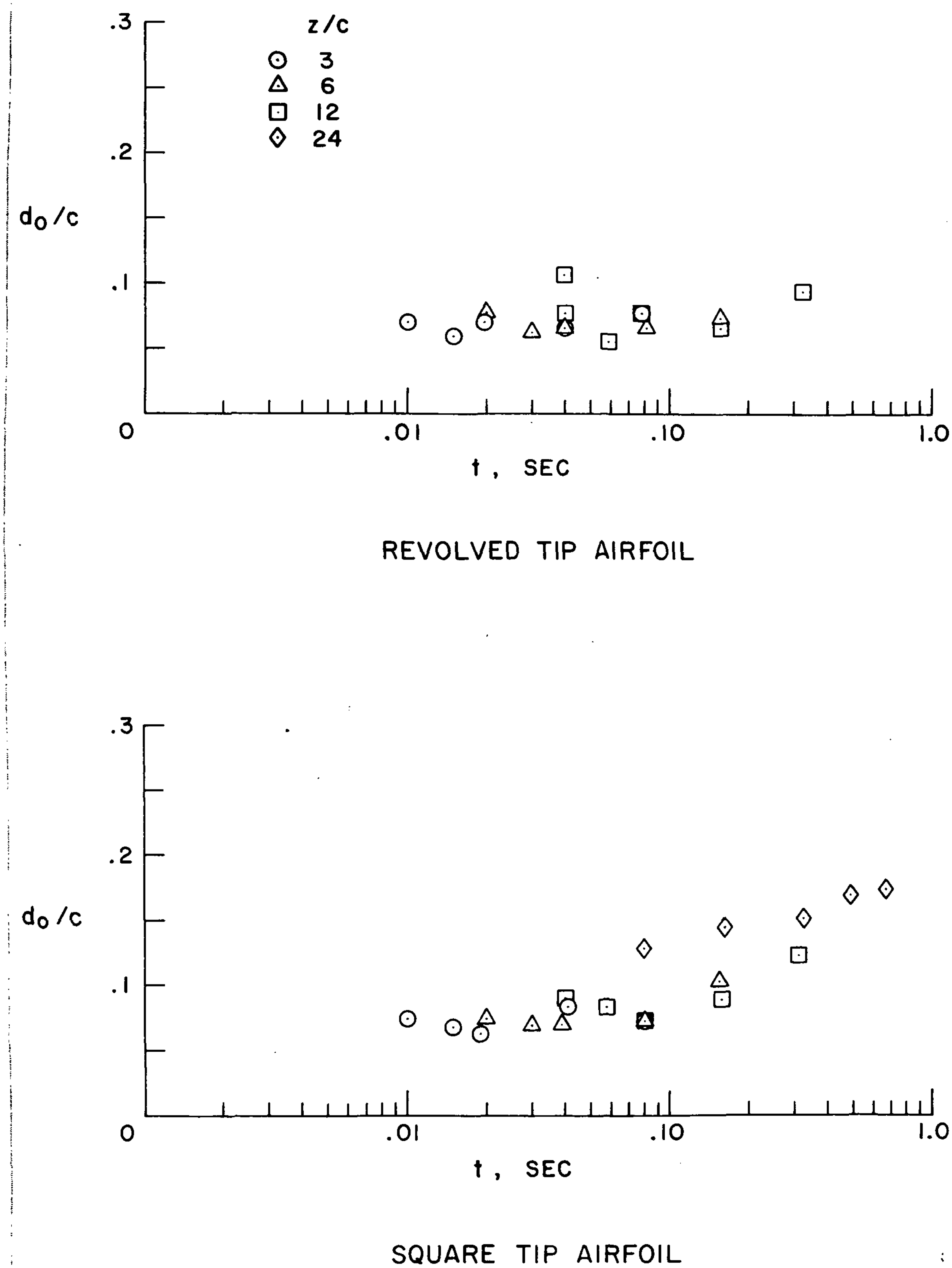

Figure 17. Vortex Core Size vs. Age, 6^{0} Wing Angle.

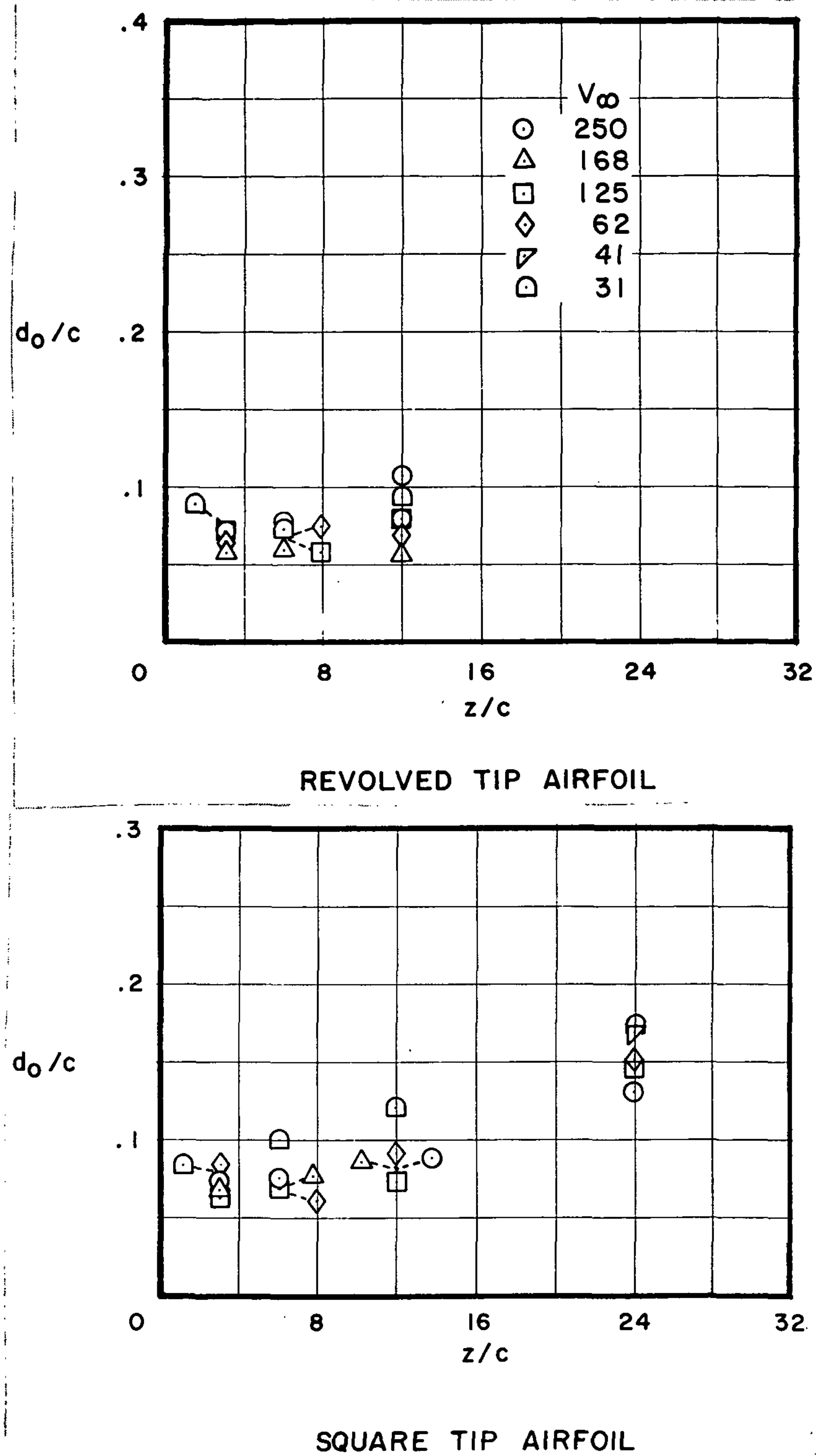

Figure 18. Vortex Core Size vs. Downstream Distance, 6^0 Wing Angle.

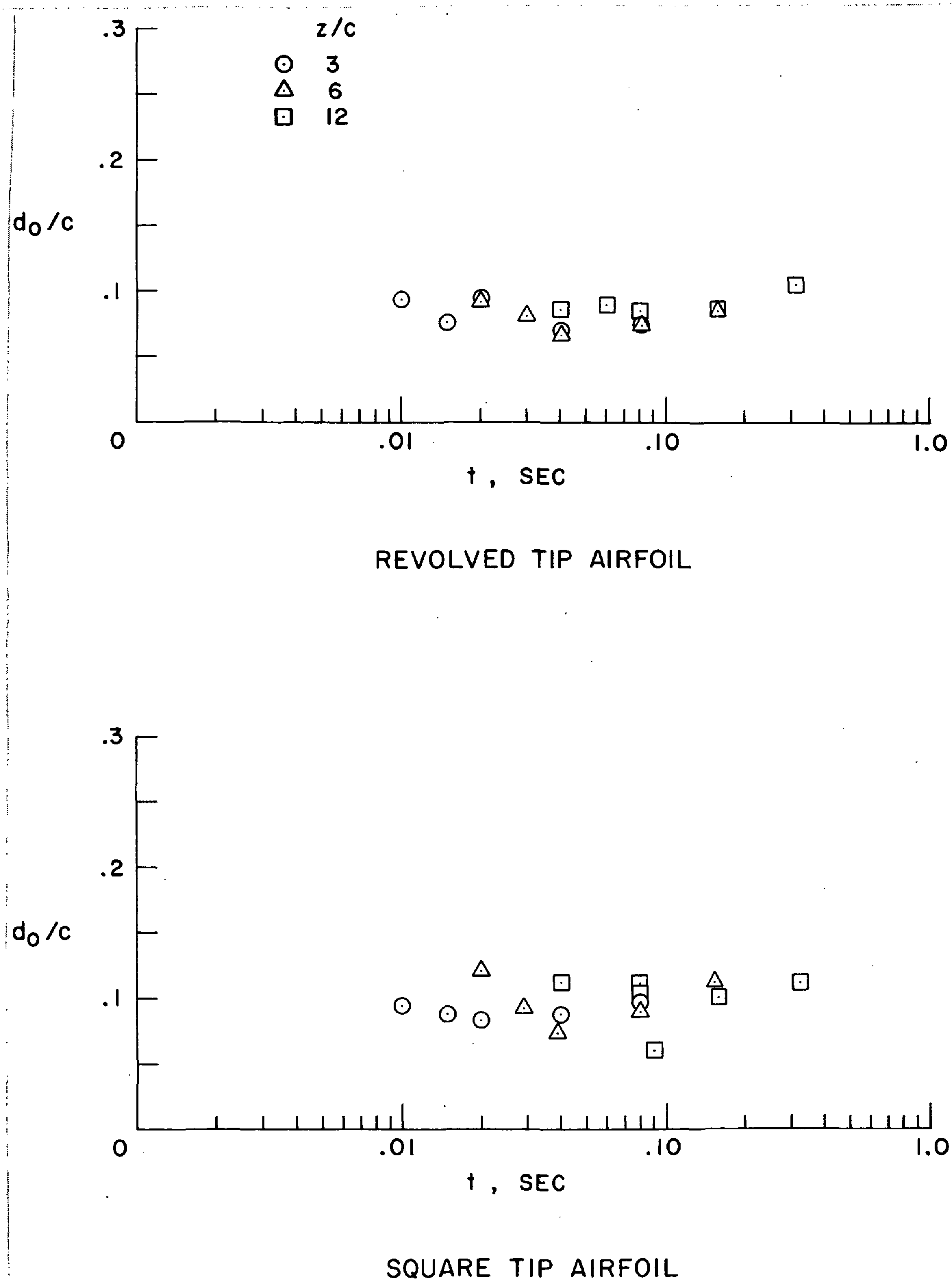

Figure 19. Vortex Core Size vs. Age, 8^o Wing Angle.

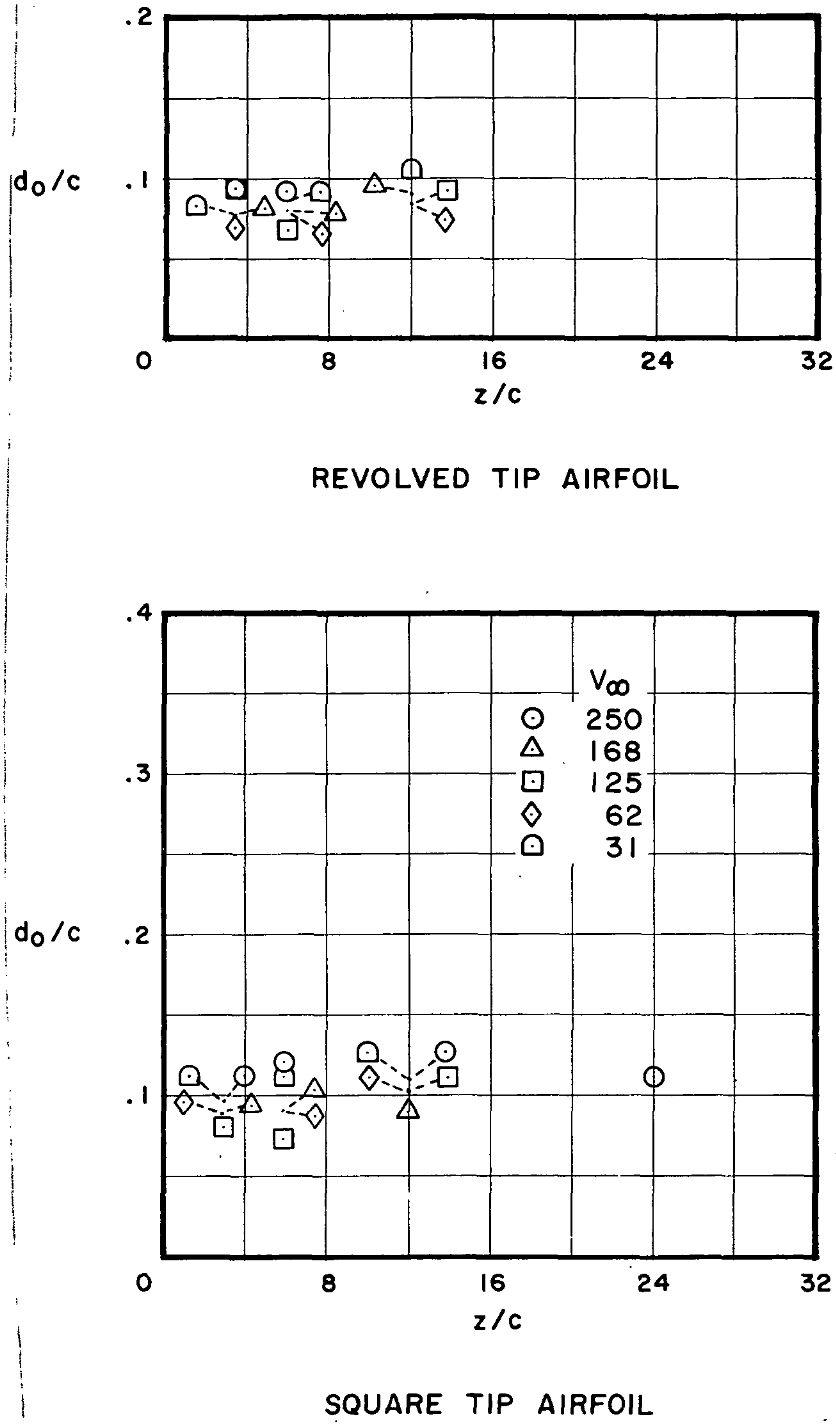

Figure 20. Vortex Core Size vs. Downstream Distance, 8^0 Wing Angle.

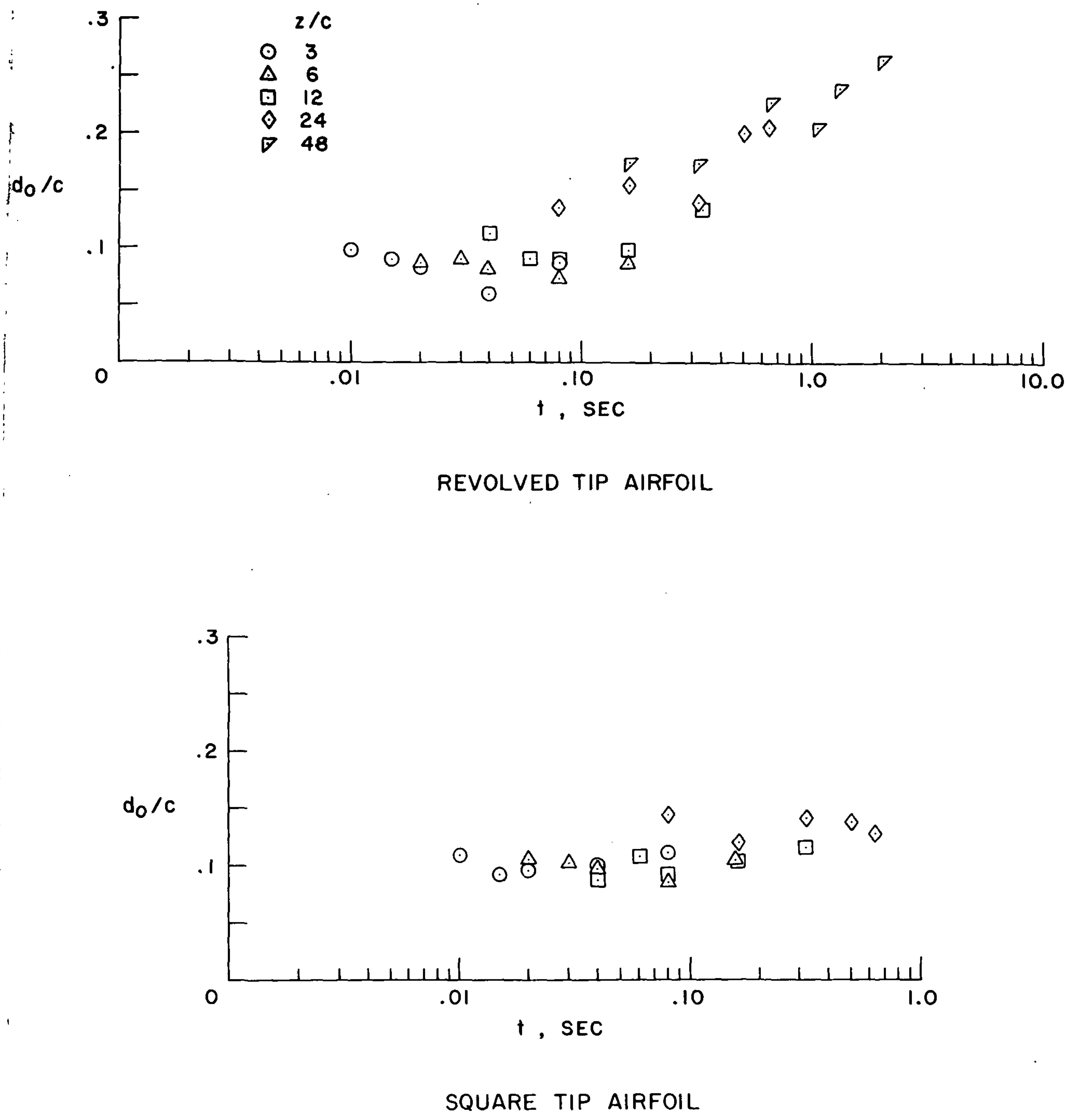

Figure 21. Vortex Core Size vs. Vortex Age, 9° Wing Angle.

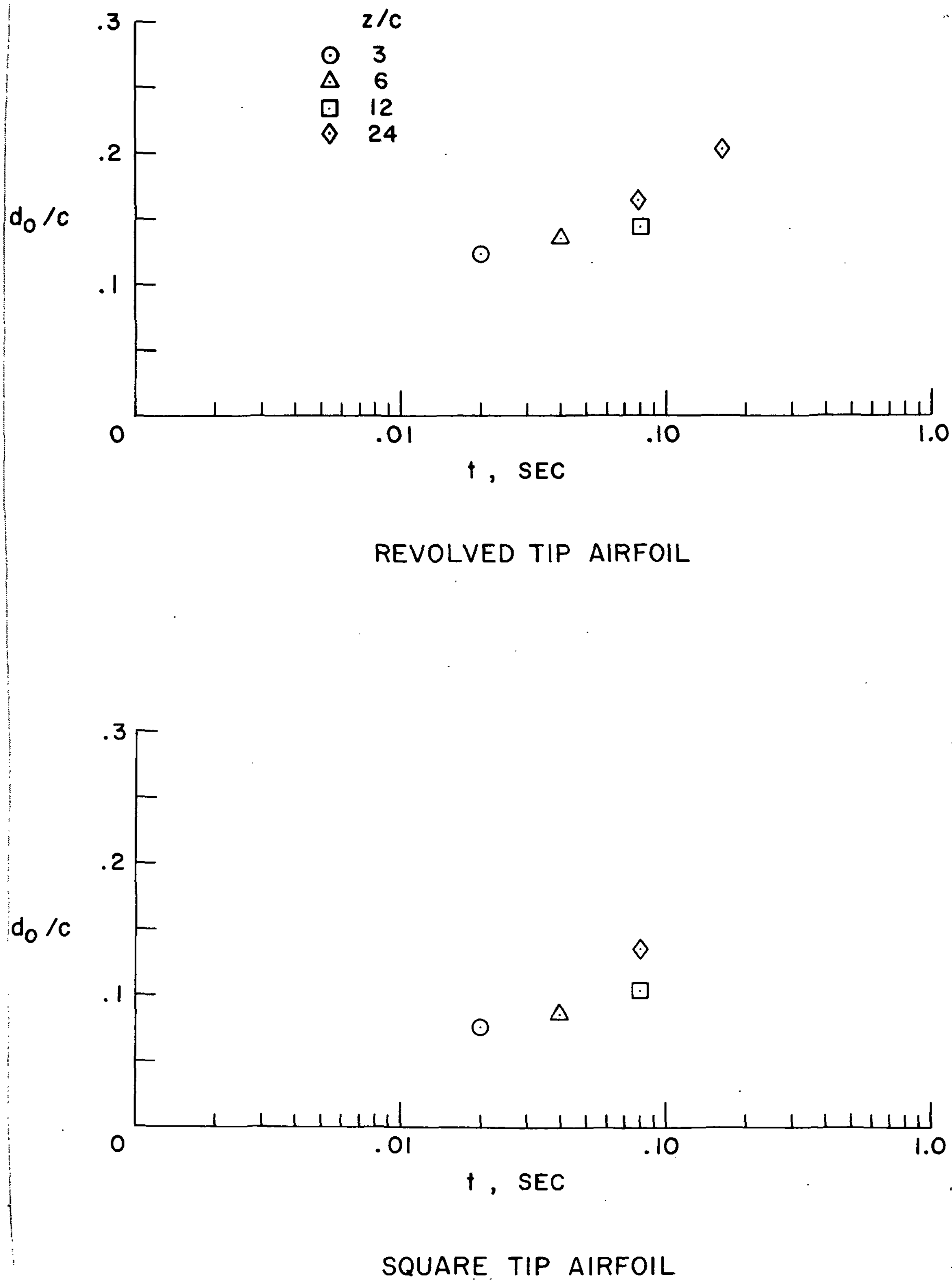

Figure 23. Vortex Core Size vs. Vortex Age, 12° Wing Angle.

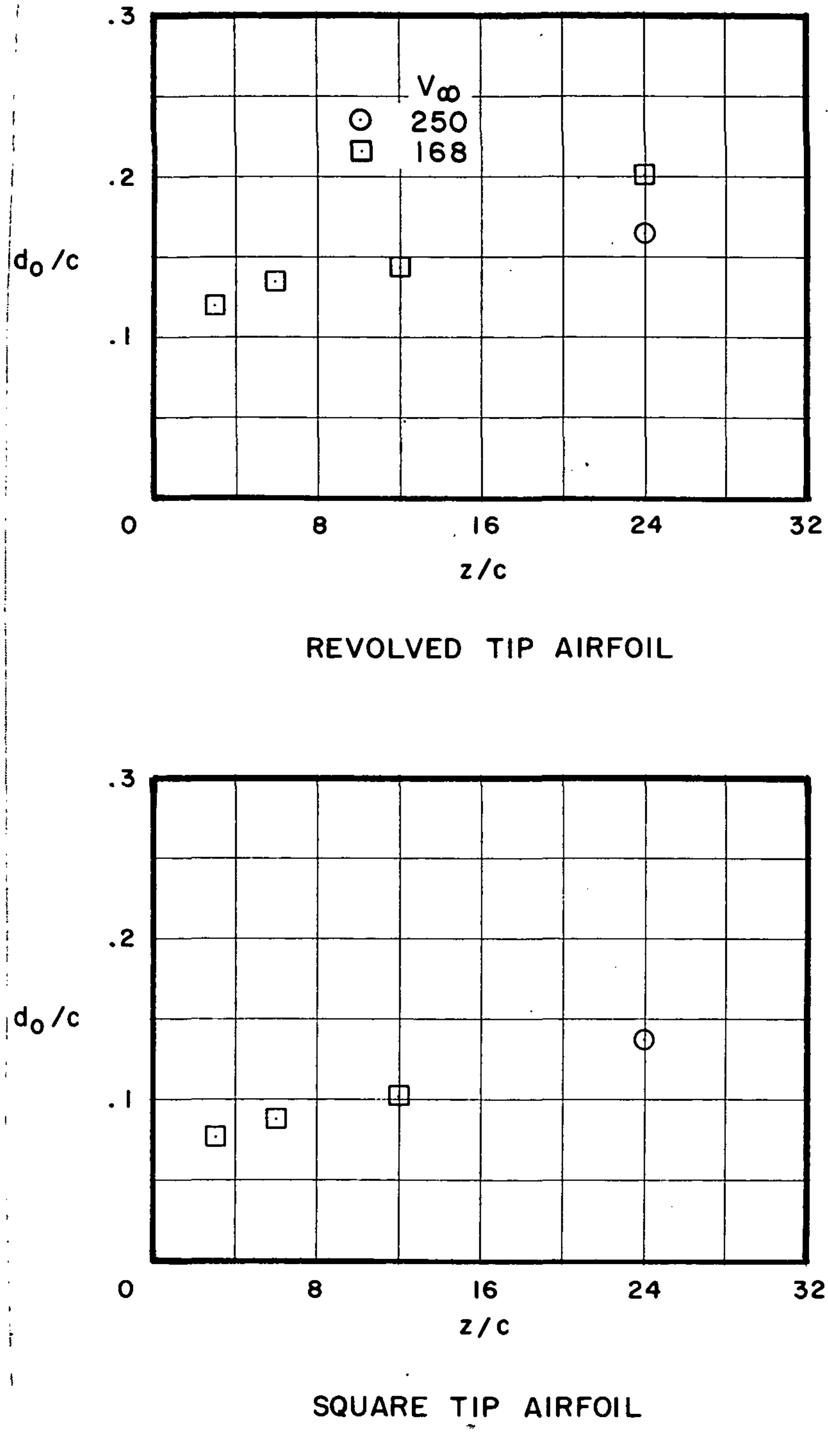

Figure 24. Vortex Core Size vs. Downstream Distance, 12° Wing Angle.

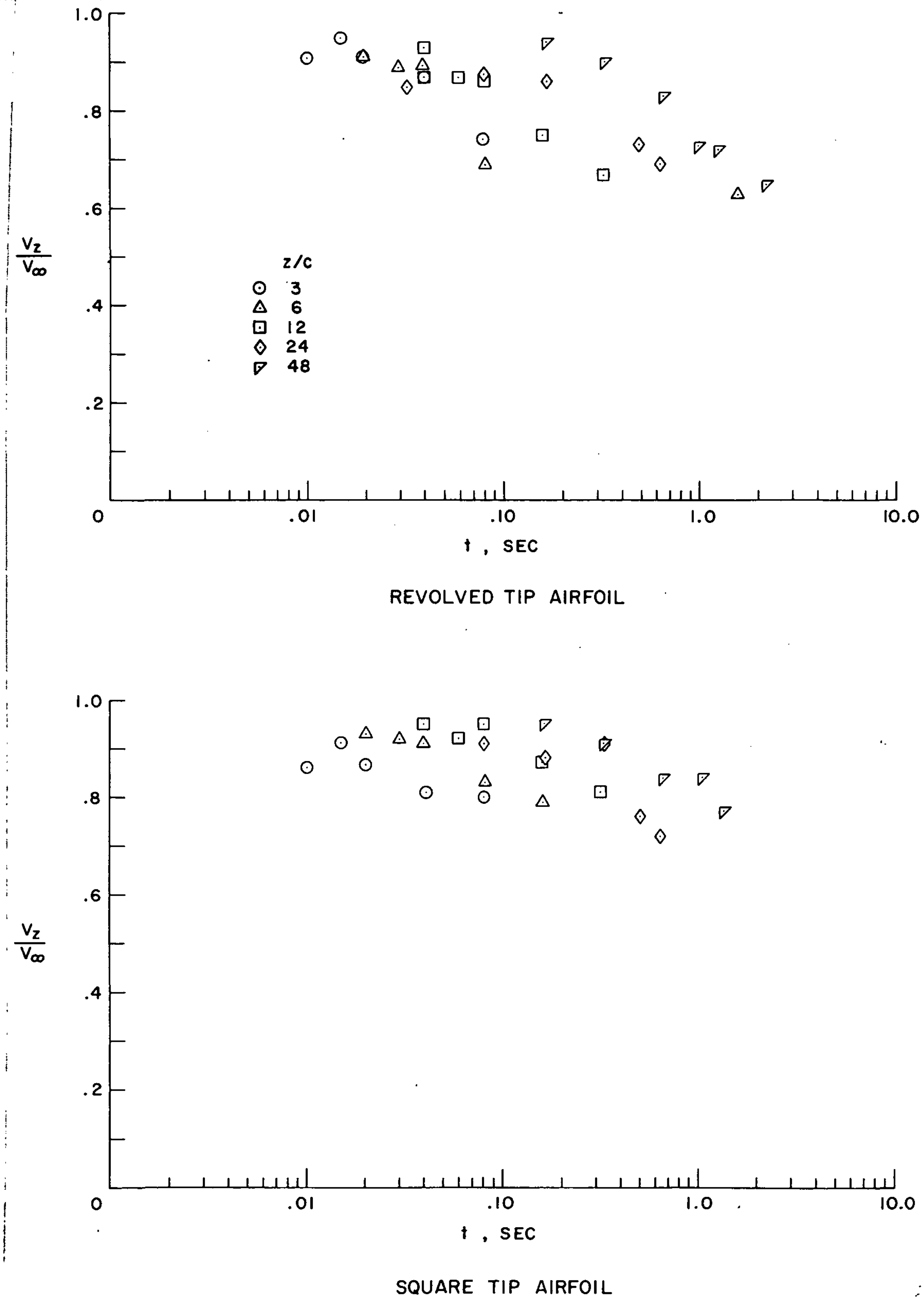

Figure 25. Axial Velocity Ratio vs. Vortex Age, 6^{0} Wing Angle.

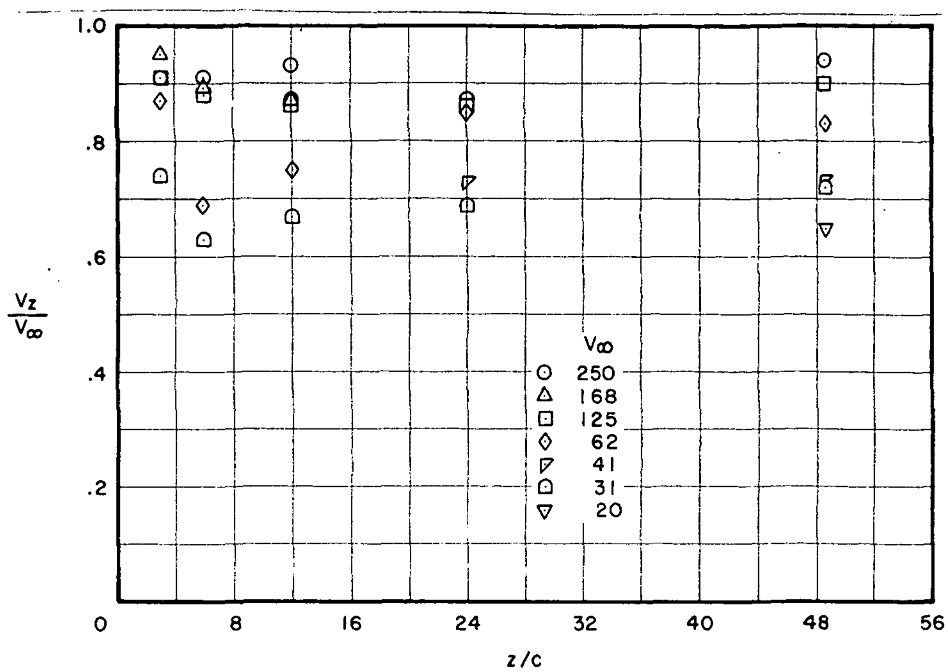

REVOLVED TIP AIRFOIL

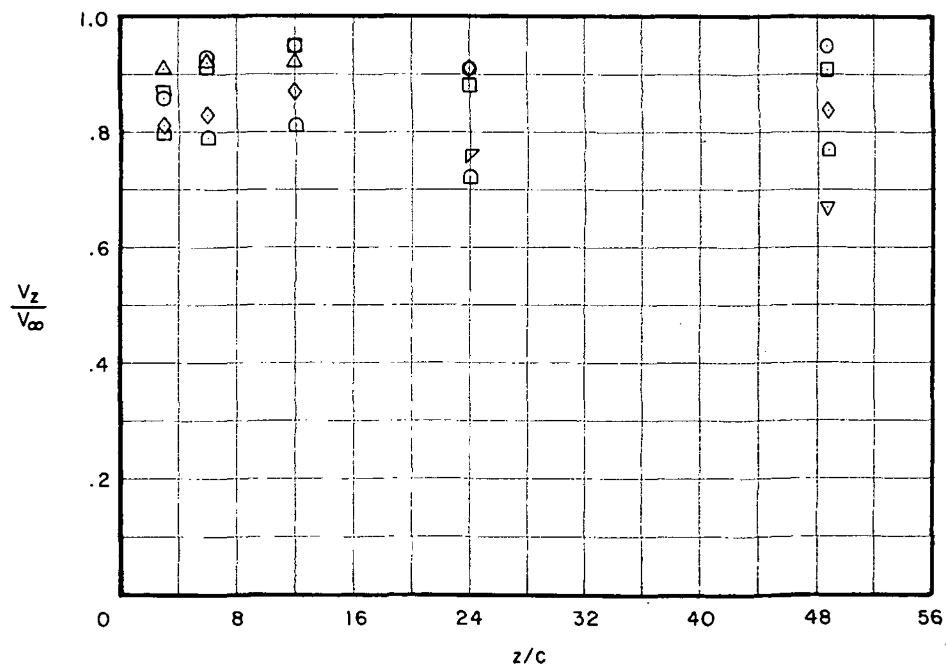

SQUARE TIP AIRFOIL

Figure 26. Axial Velocity Ratio vs. Downstream Distance, 6^{0} Wing Angle.

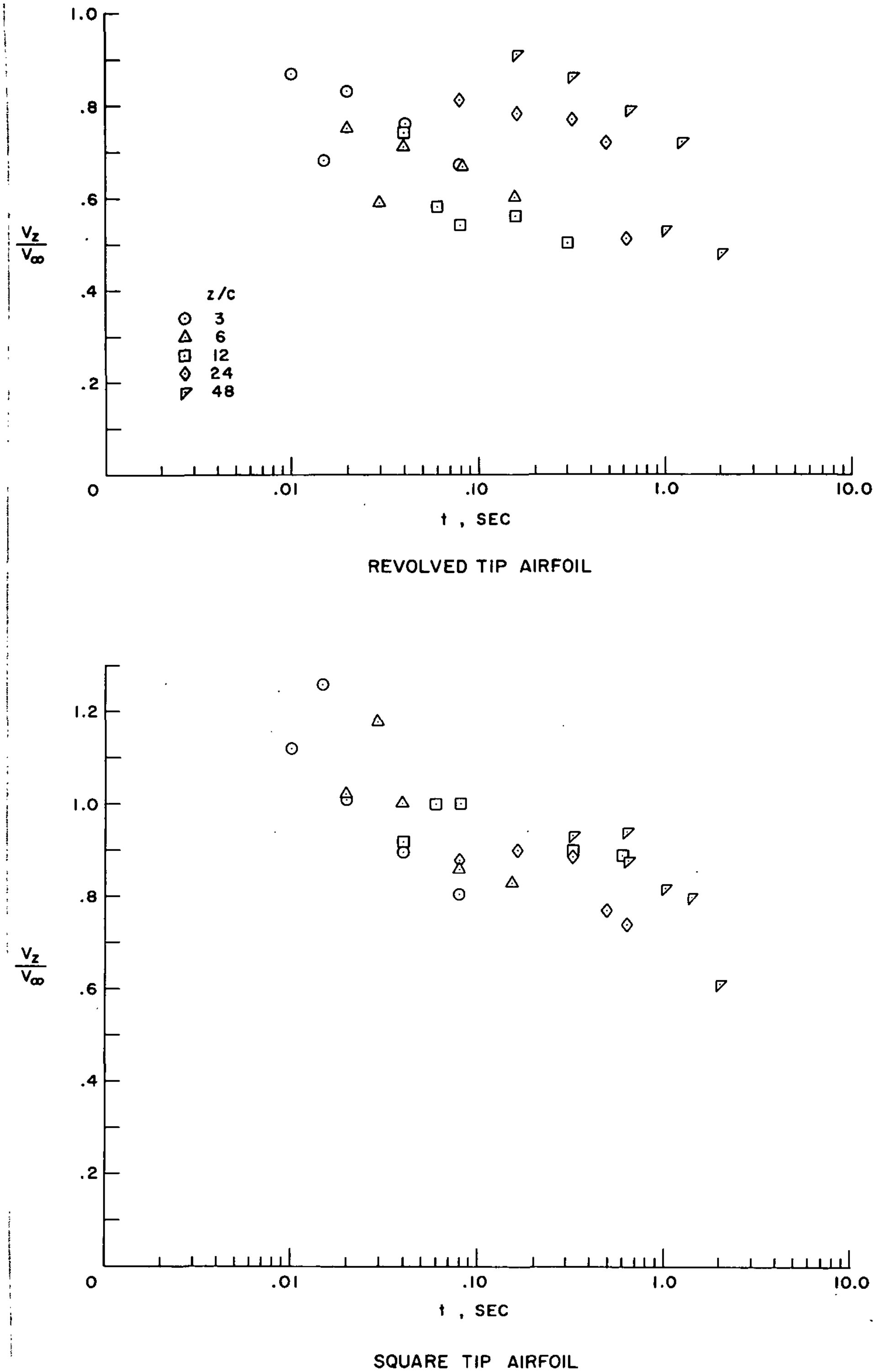

Figure 27. Axial Velocity Ratio vs. Vortex Age, 8^{0} Wing Angle.

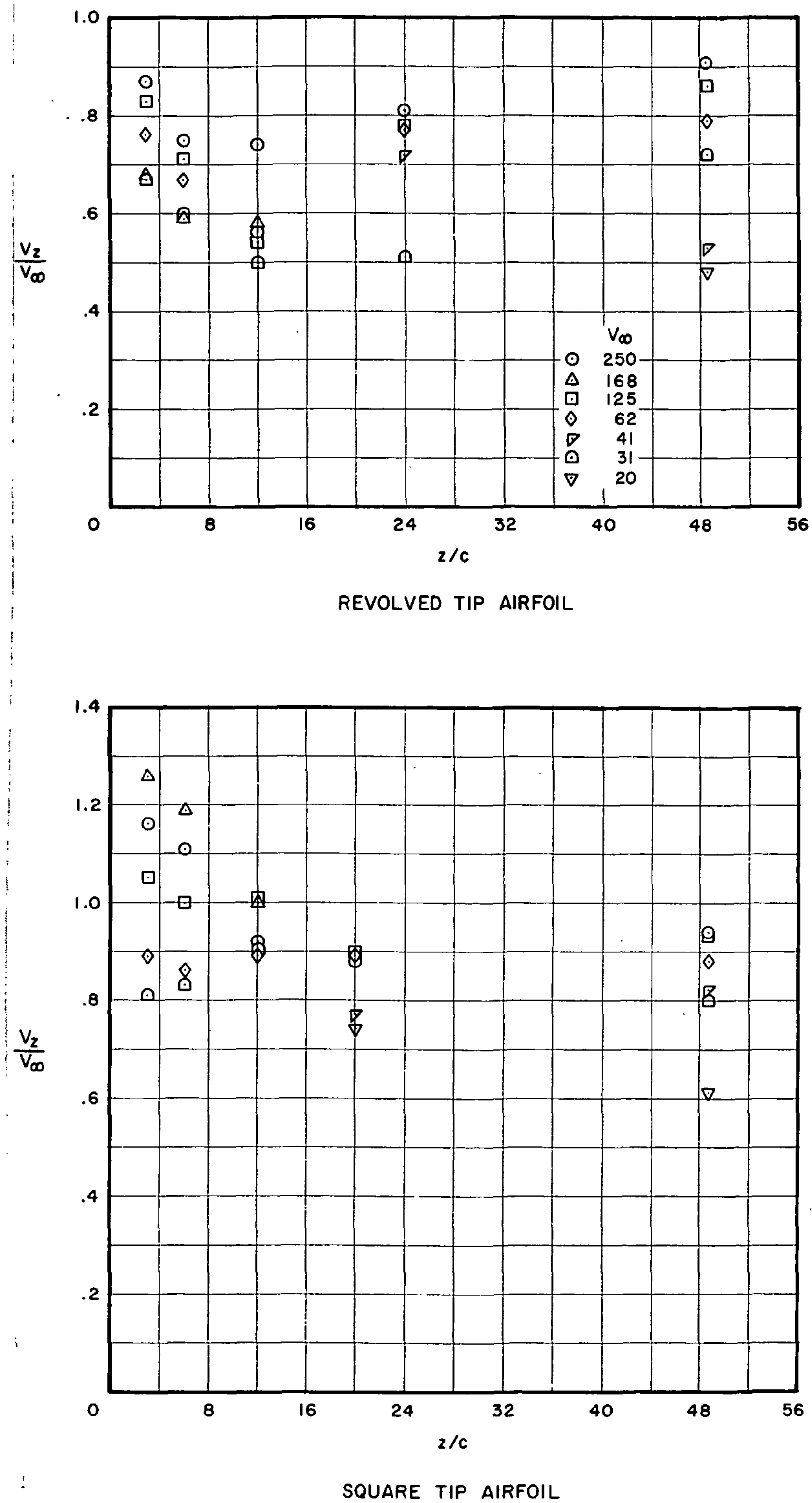

Figure 28. Axial Velocity Ratio vs. Downstream Distance, 8° Wing Angle.

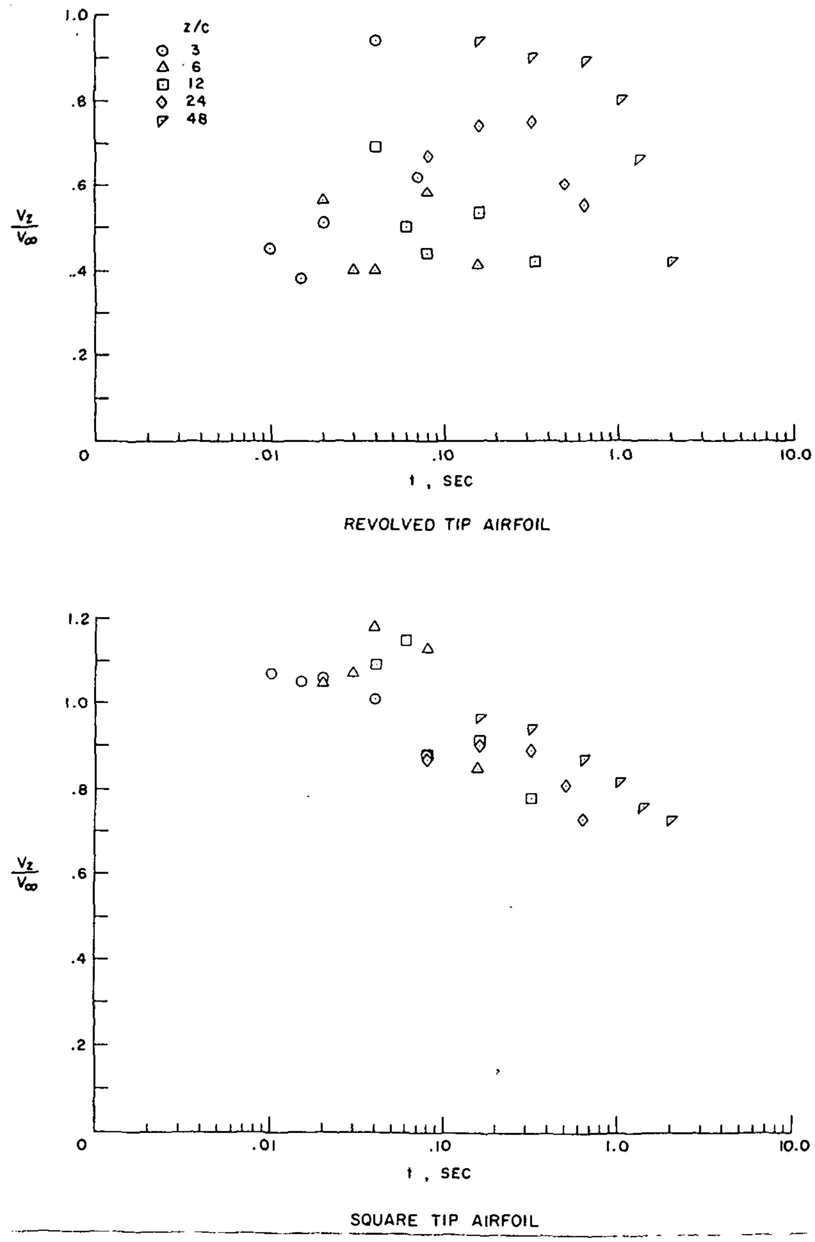

Figure 29. Axial Velocity Ratio vs. Vortex Age, 9° Wing Angle

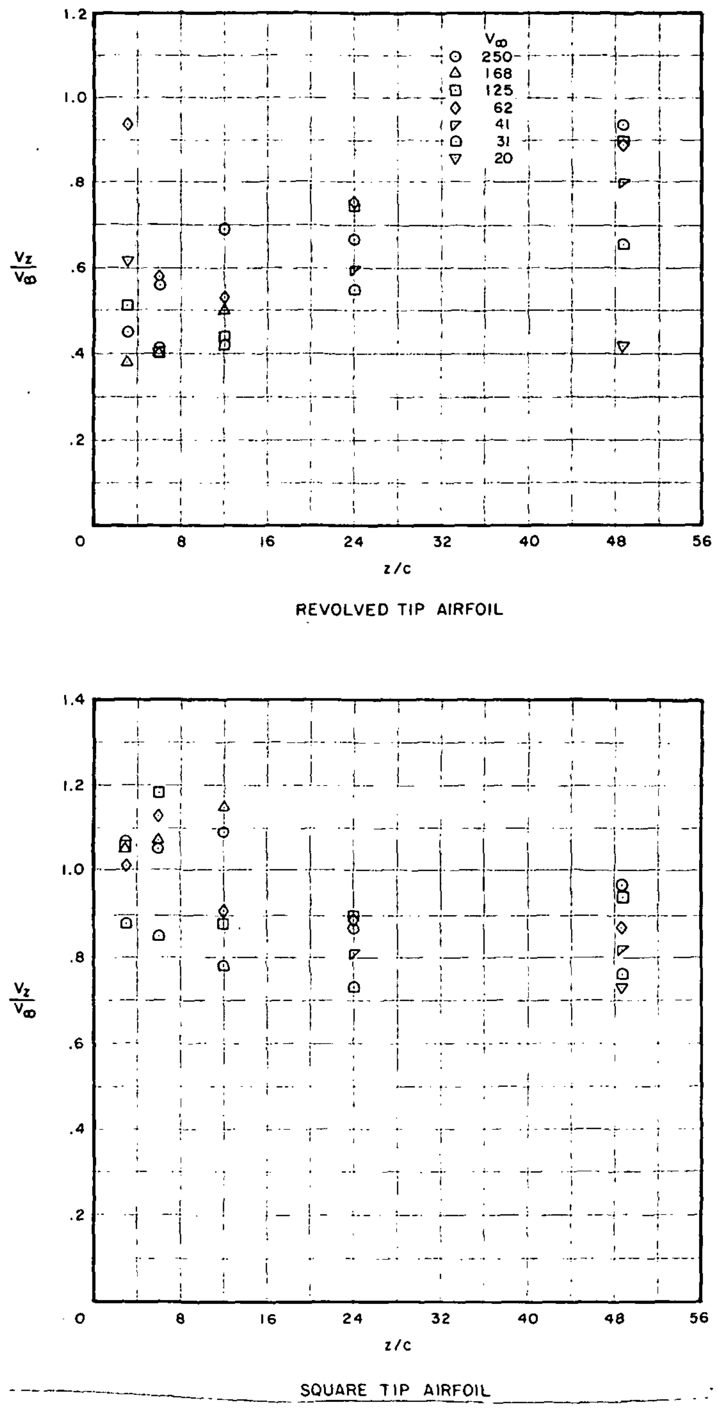

Figure 30. Axial Velocity Ratio vs. Downstream Distance, 9° Wing Angle.

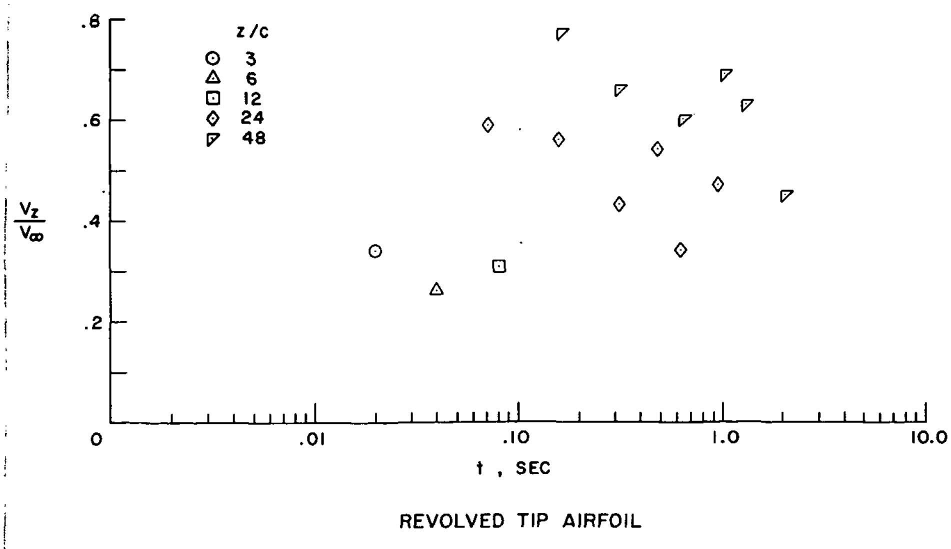

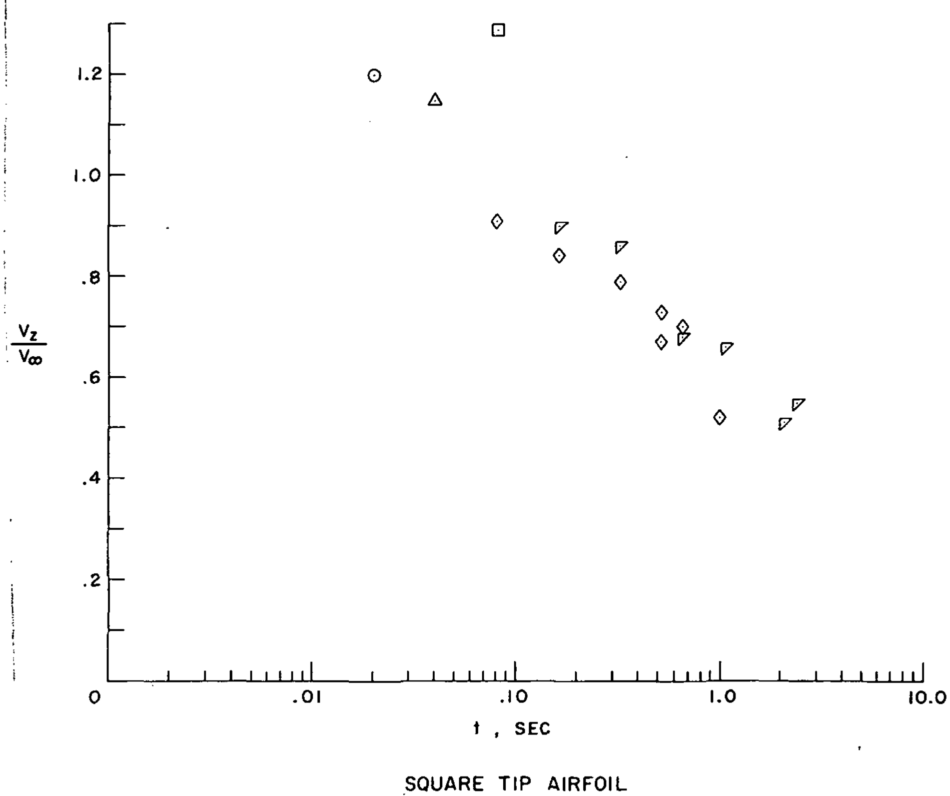

Figure 31. Axial Velocity Ratio vs. Vortex Age, 12° Wing Angle.

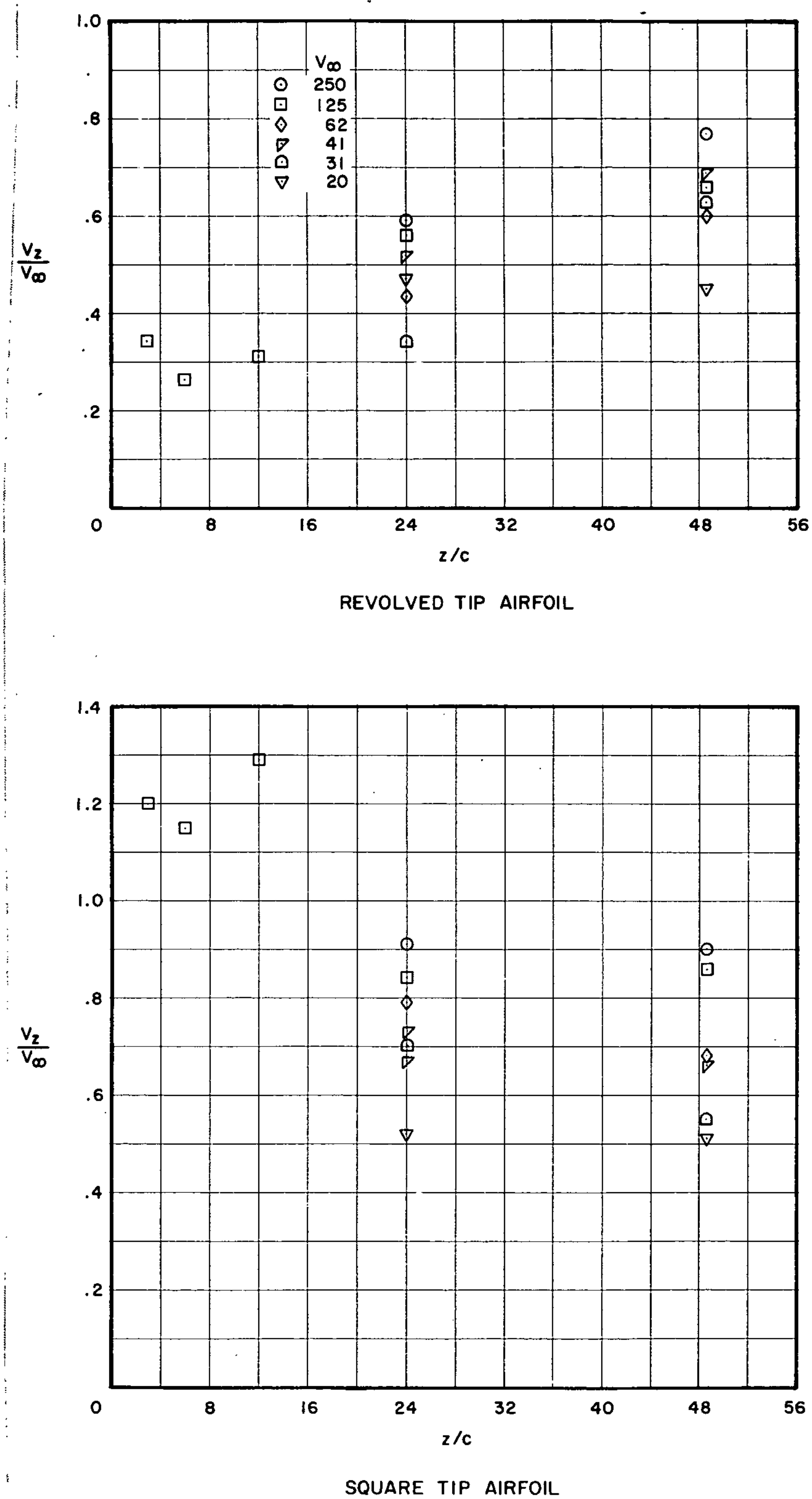

Figure 32. Axial Velocity Ratio vs. Downstream Distance, 12^{o} Wing Angle.

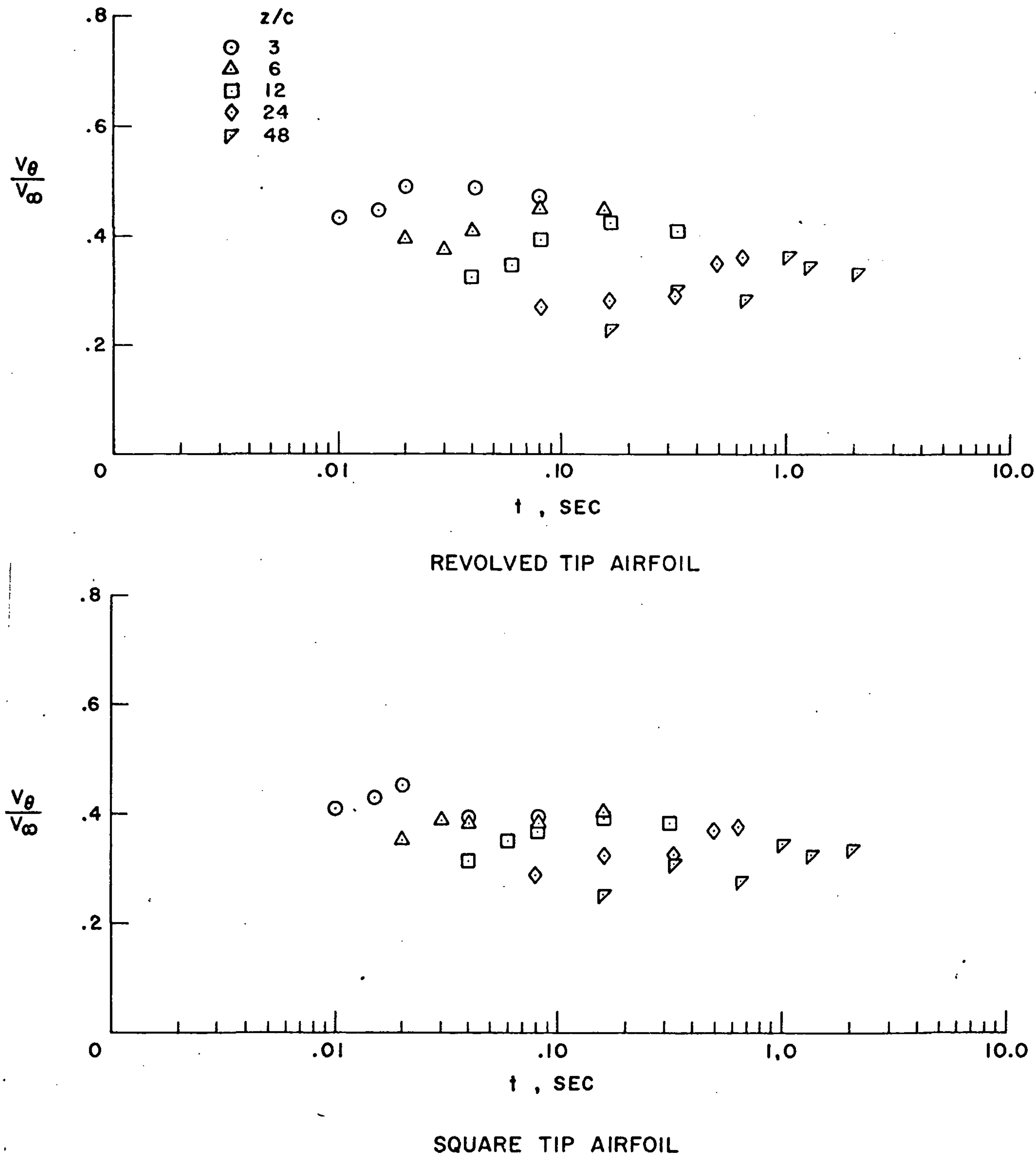

Figure 33. Tangential Velocity Ratio vs. Vortex Age, 6^{0} Wing Angle.

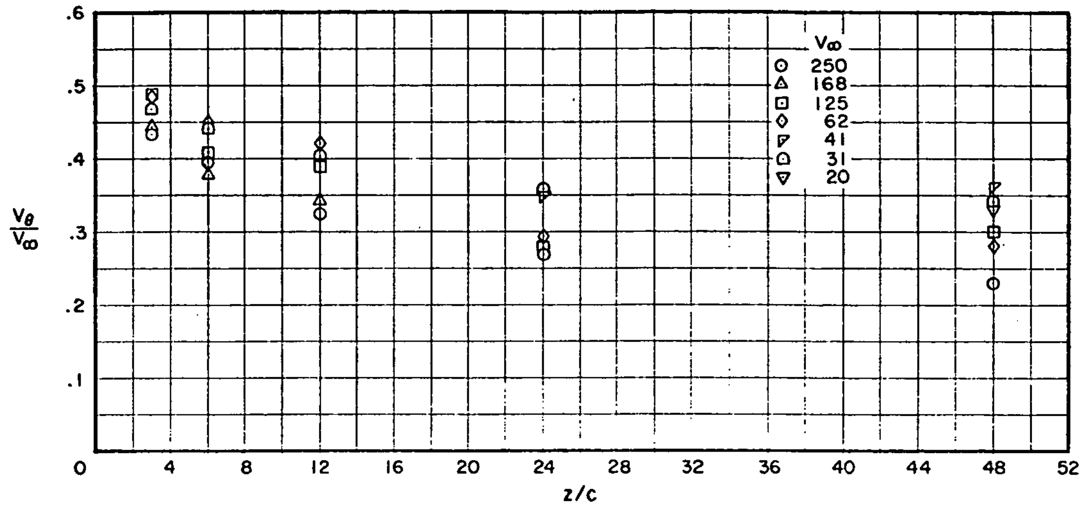

REVOLVED TIP AIRFOIL

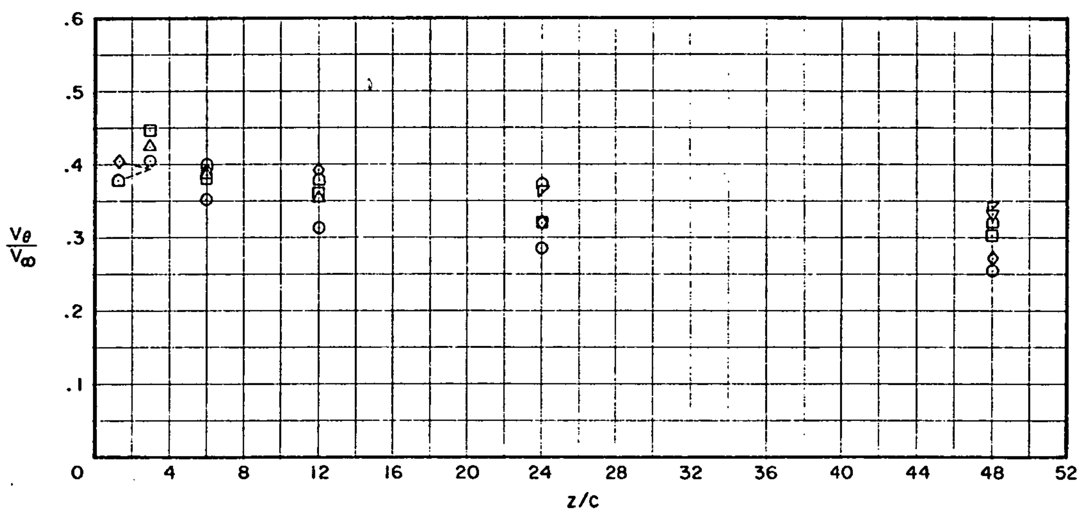

SQUARE TIP AIRFOIL

Figure 34. Tangential Velocity Ratio vs. Downstream Distance, 6^{o} Wing Angle.

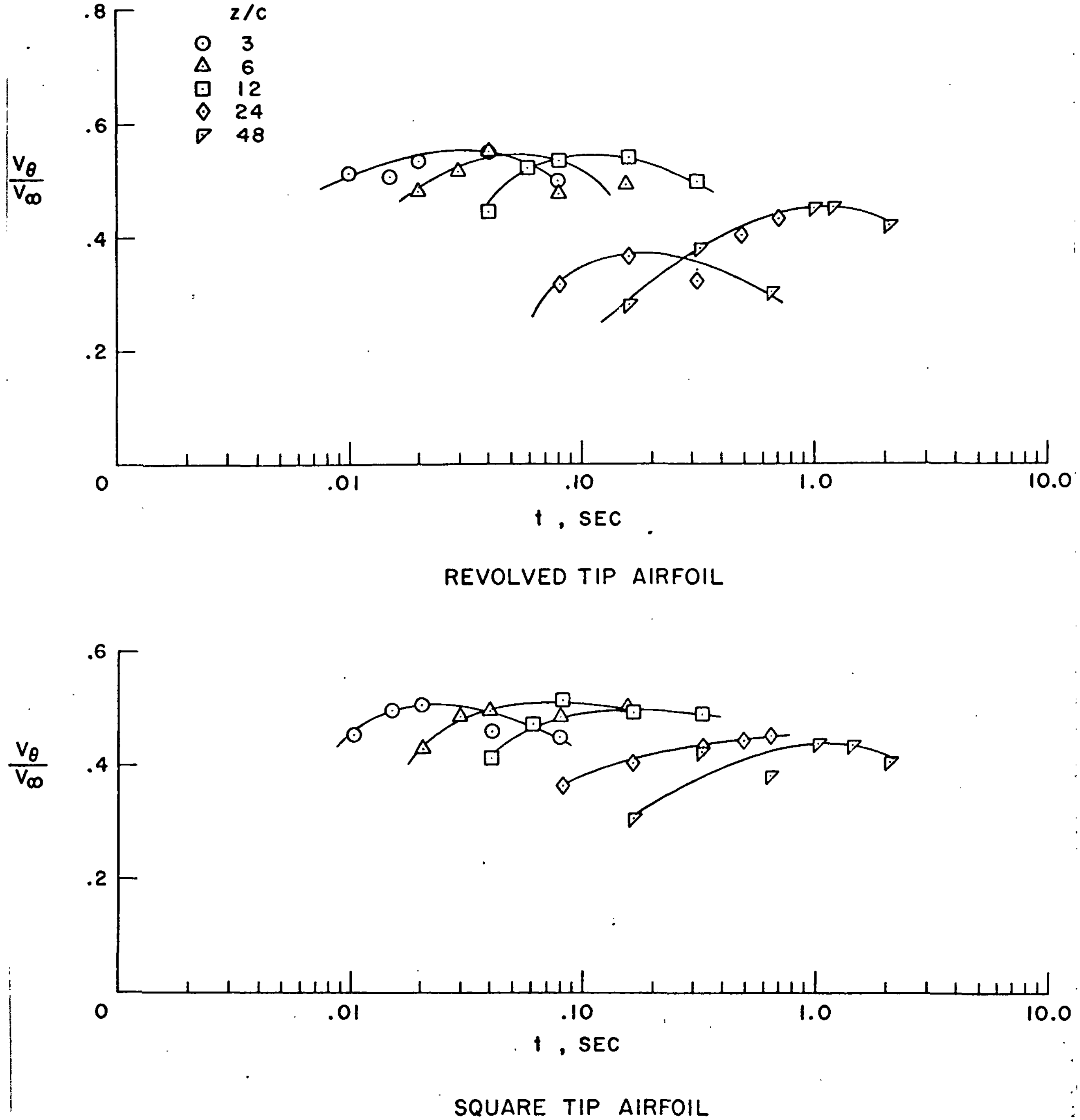

Figure 35. Tangential Velocity Ratio vs. Vortex Age, 8^{0} Wing Angle.

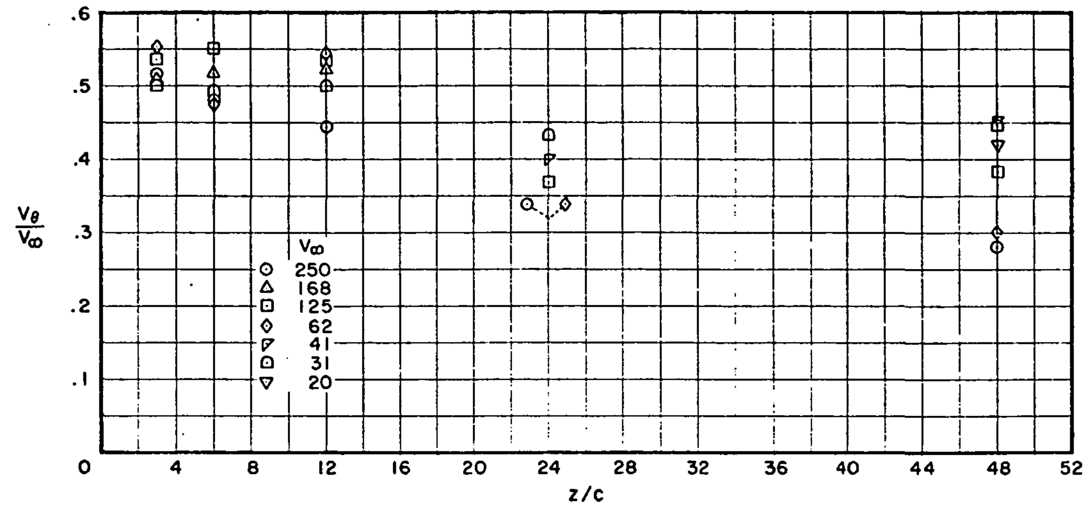

REVOLVED TIP AIRFOIL

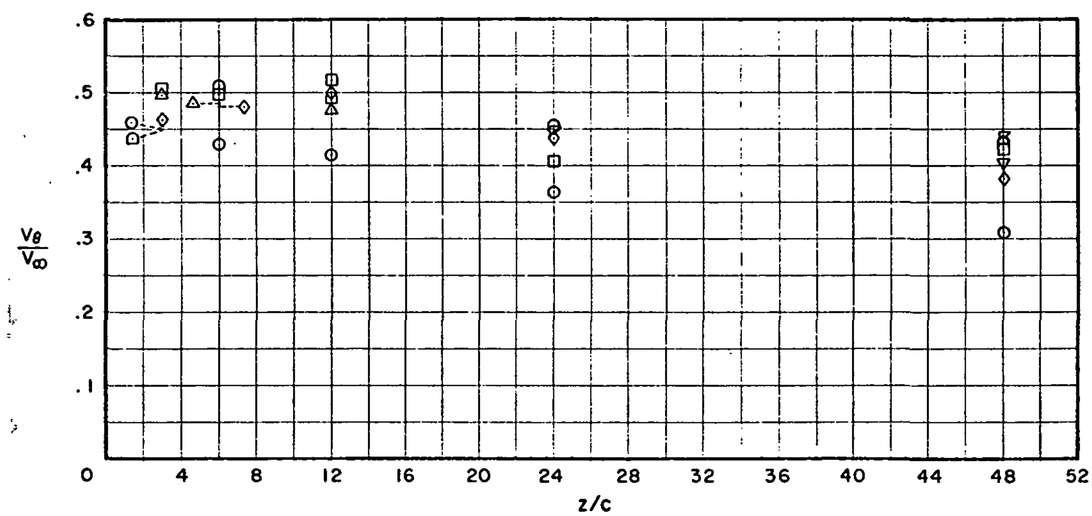

SQUARE TIP AIRFOIL

Figure 36. Tangential Velocity Ratio vs. Downstream Distance, 8^0 Wing Angle.

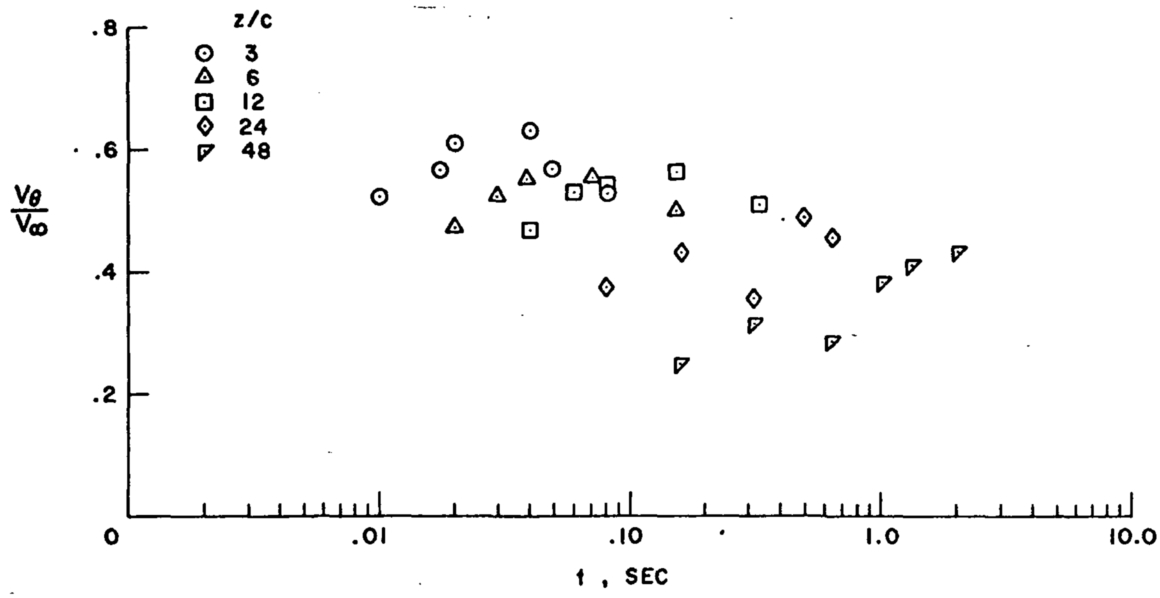

REVOLVED TIP AIRFOIL

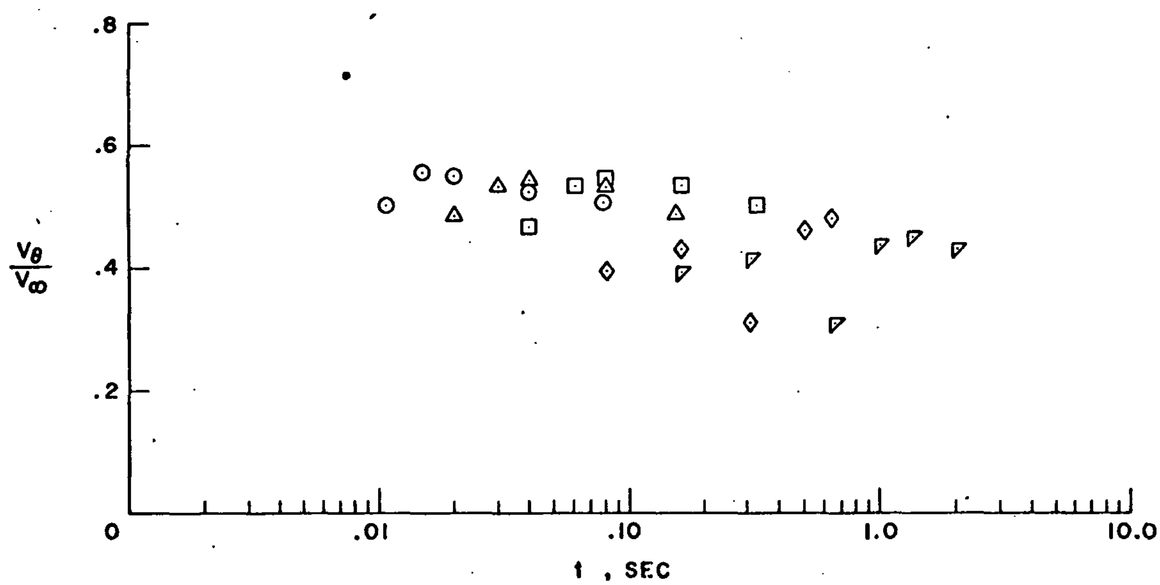

SQUARE TIP AIRFOIL

Figure 37. Tangential Velocity Ratio vs. Vortex Age, 9° Wing Angle.

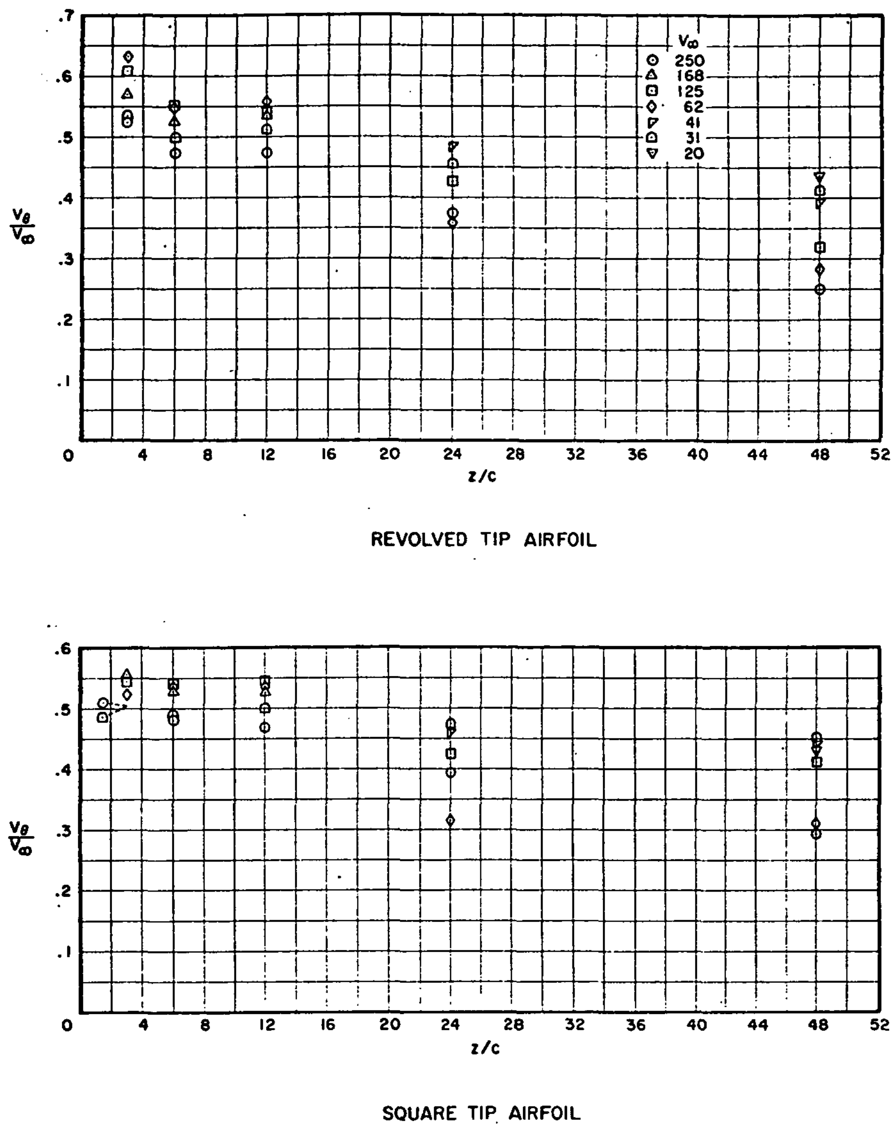

Figure 38. Tangential Velocity Ratio vs. Downstream Distance, 9^{o} Wing Angle.

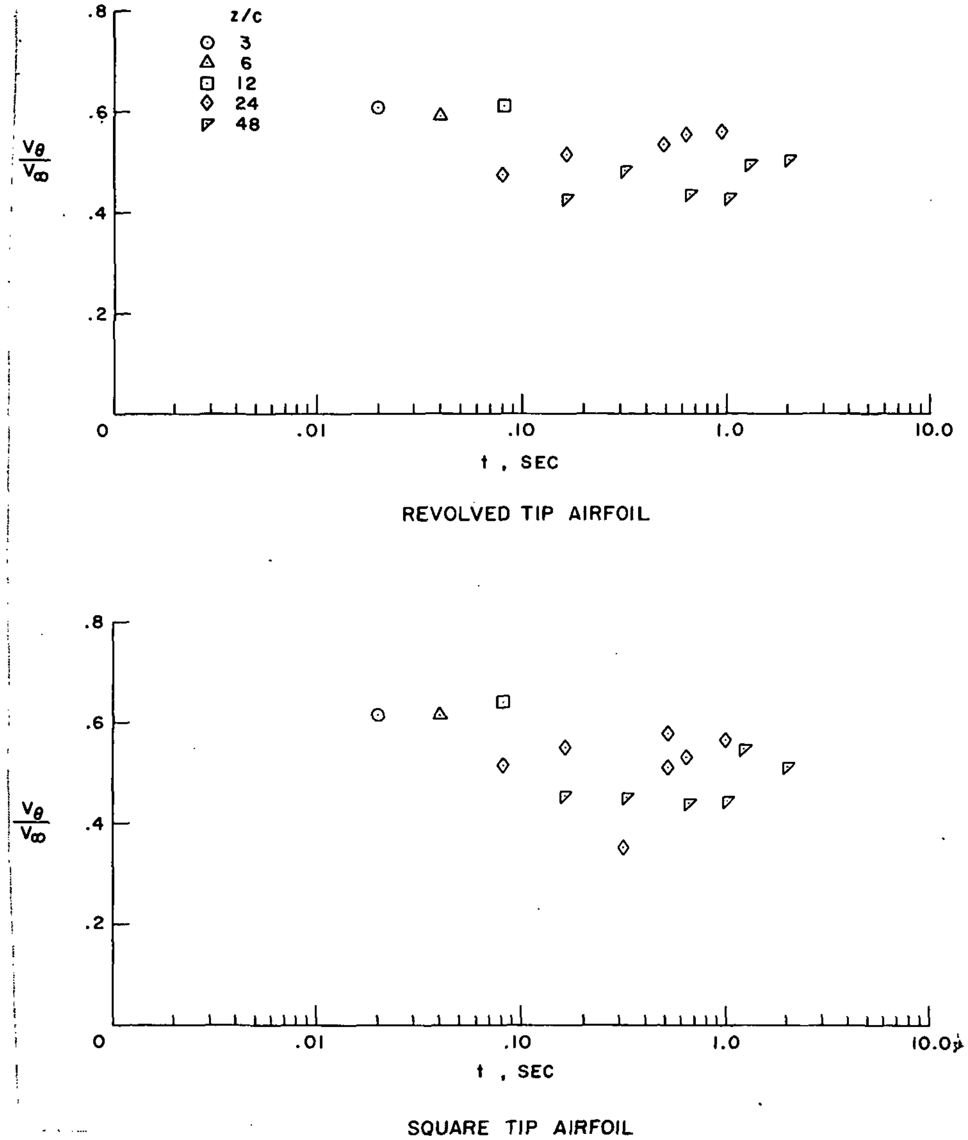

Figure 39. Tangential Velocity Ratio vs. Vortex Age, 12^{o} Wing Angle.

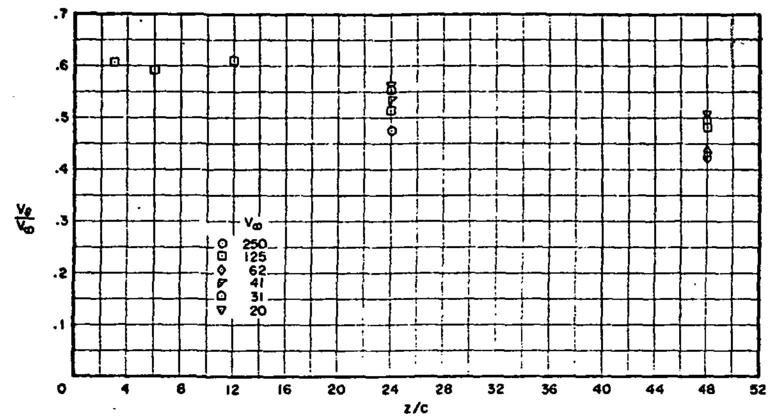

REVOLVED TIP AIRFOIL

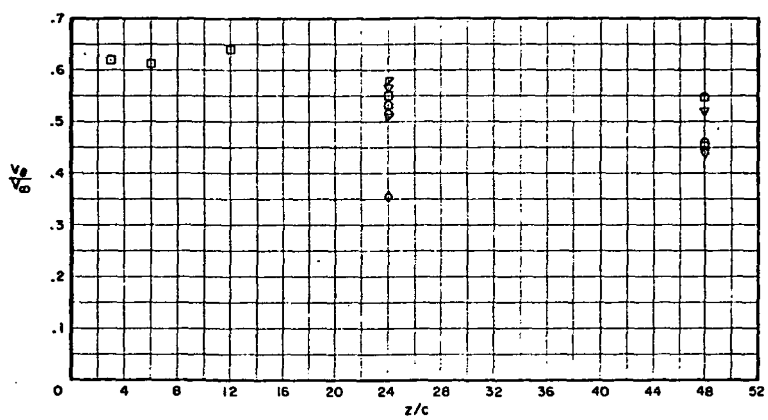

SQUARE TIP AIRFOIL

Figure 40. Tangential Velocity Ratio vs. Downstream Distance, 12^{o} Wing Angle.

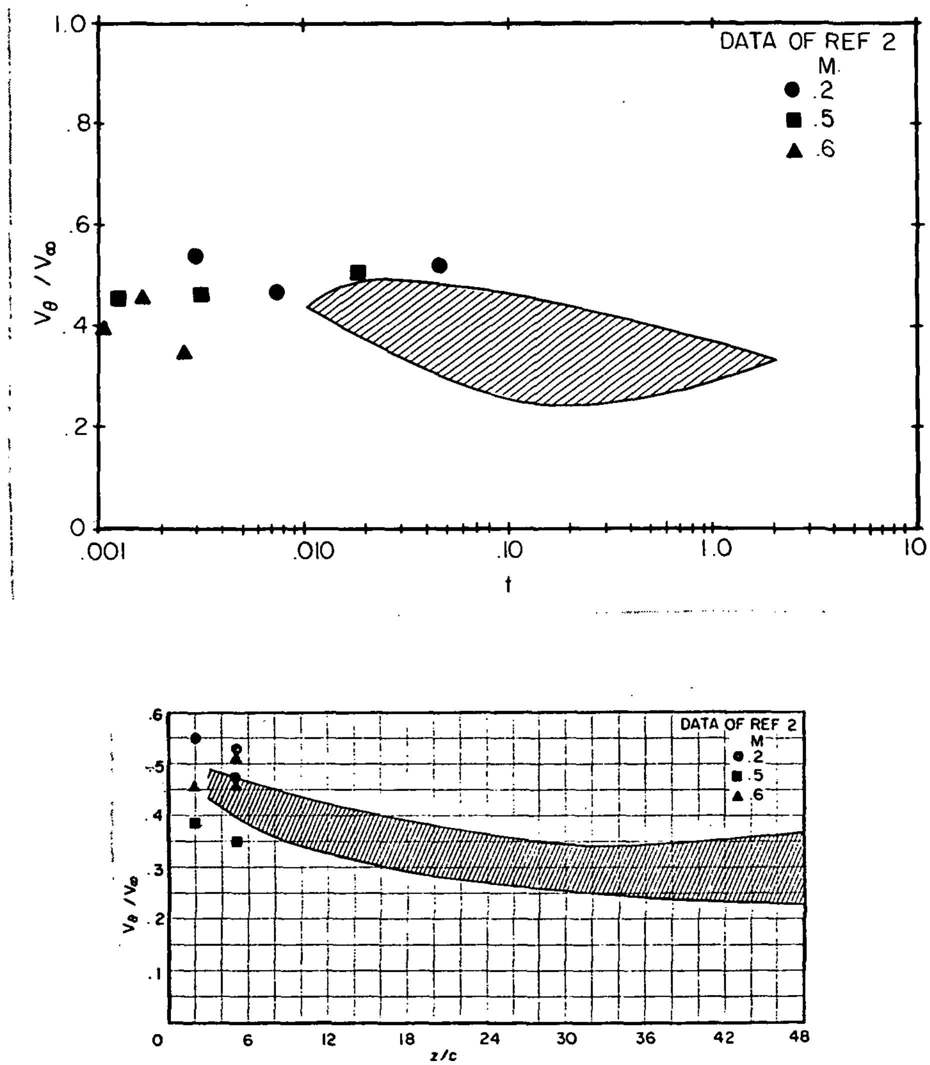

Figure 41. Tangential Velocity Ratio Comparison with Previous Results, 6^{o} Revolved Tip.

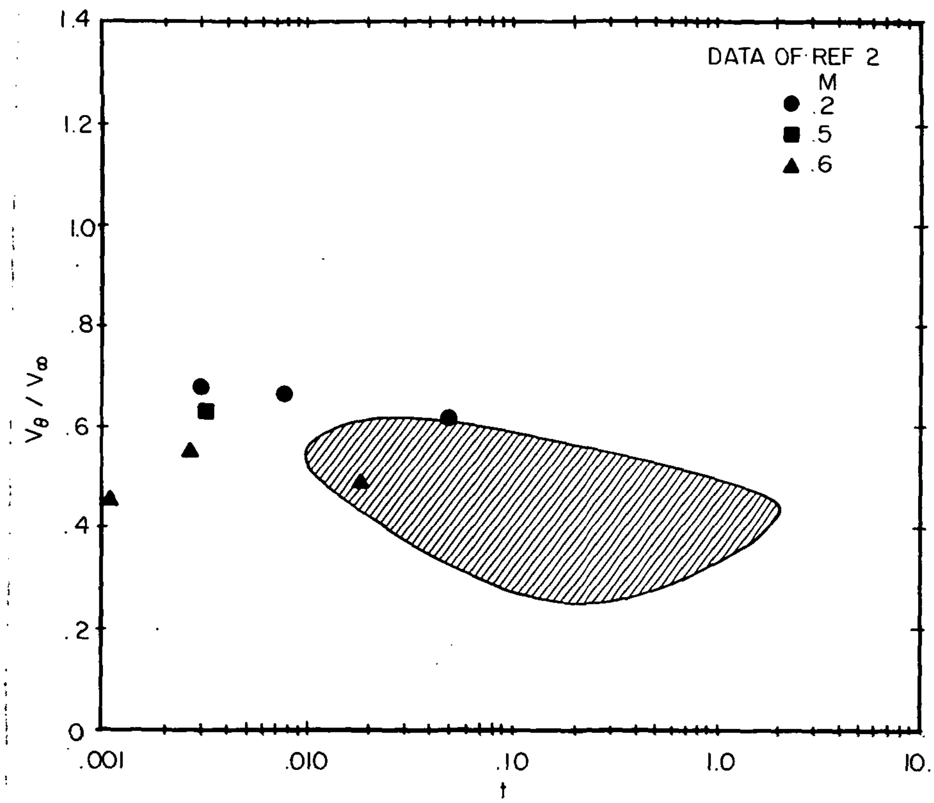

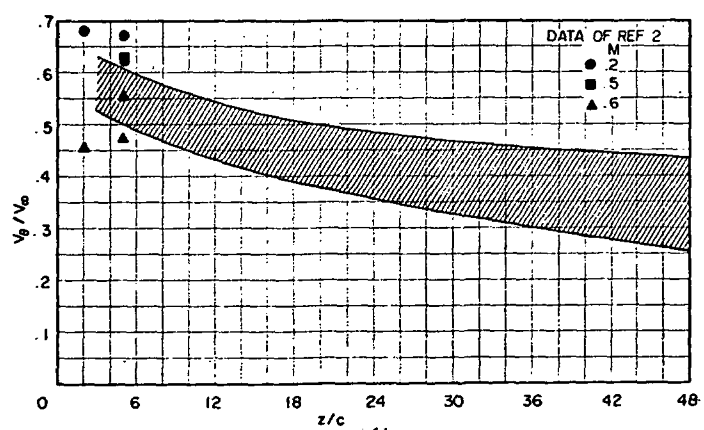

Figure 42. Tangential Velocity Ratio Comparison with Previous Results, 9° Revolved Tip.

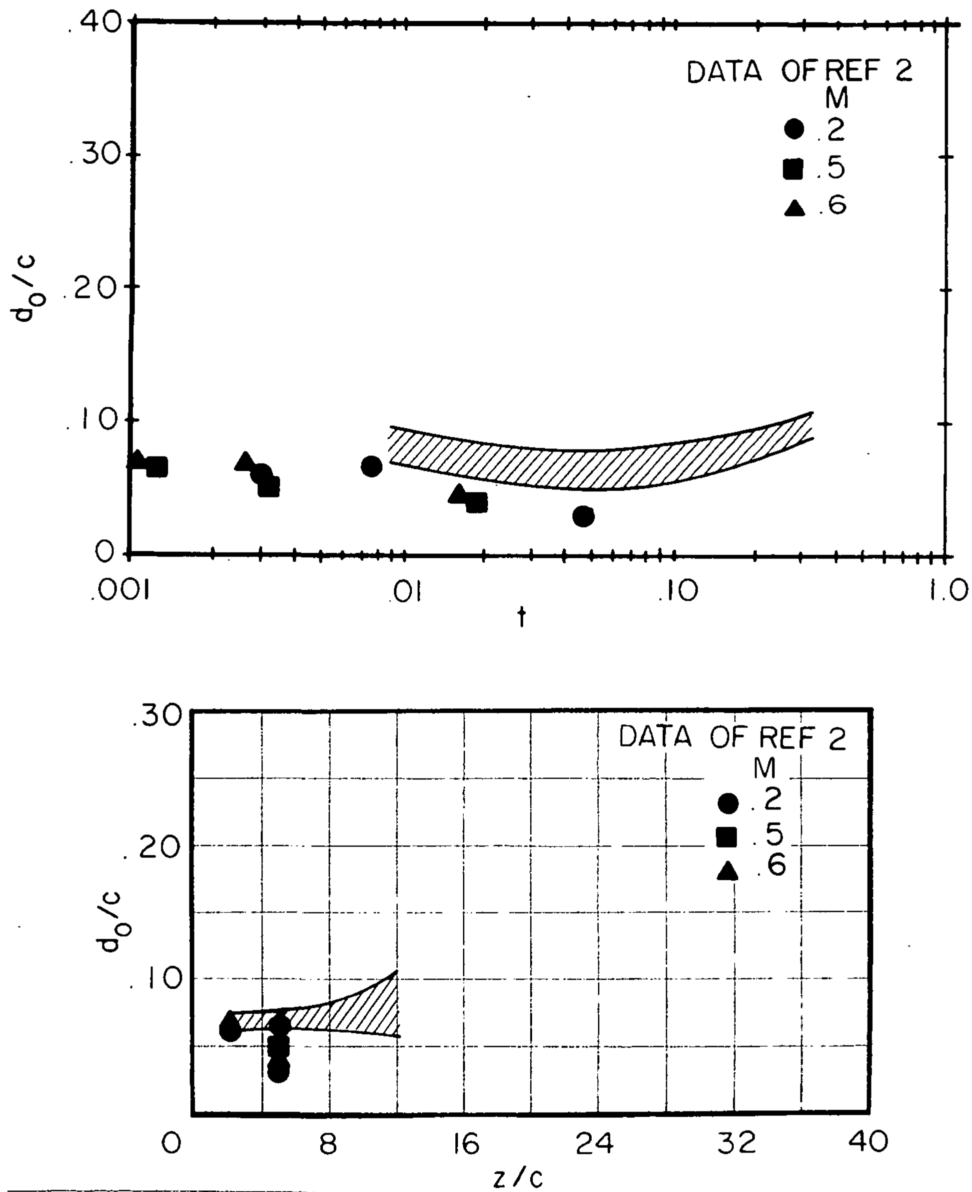

Figure 43. Vortex Core Size Comparison with Previous Results, 6° Revolved Tip.

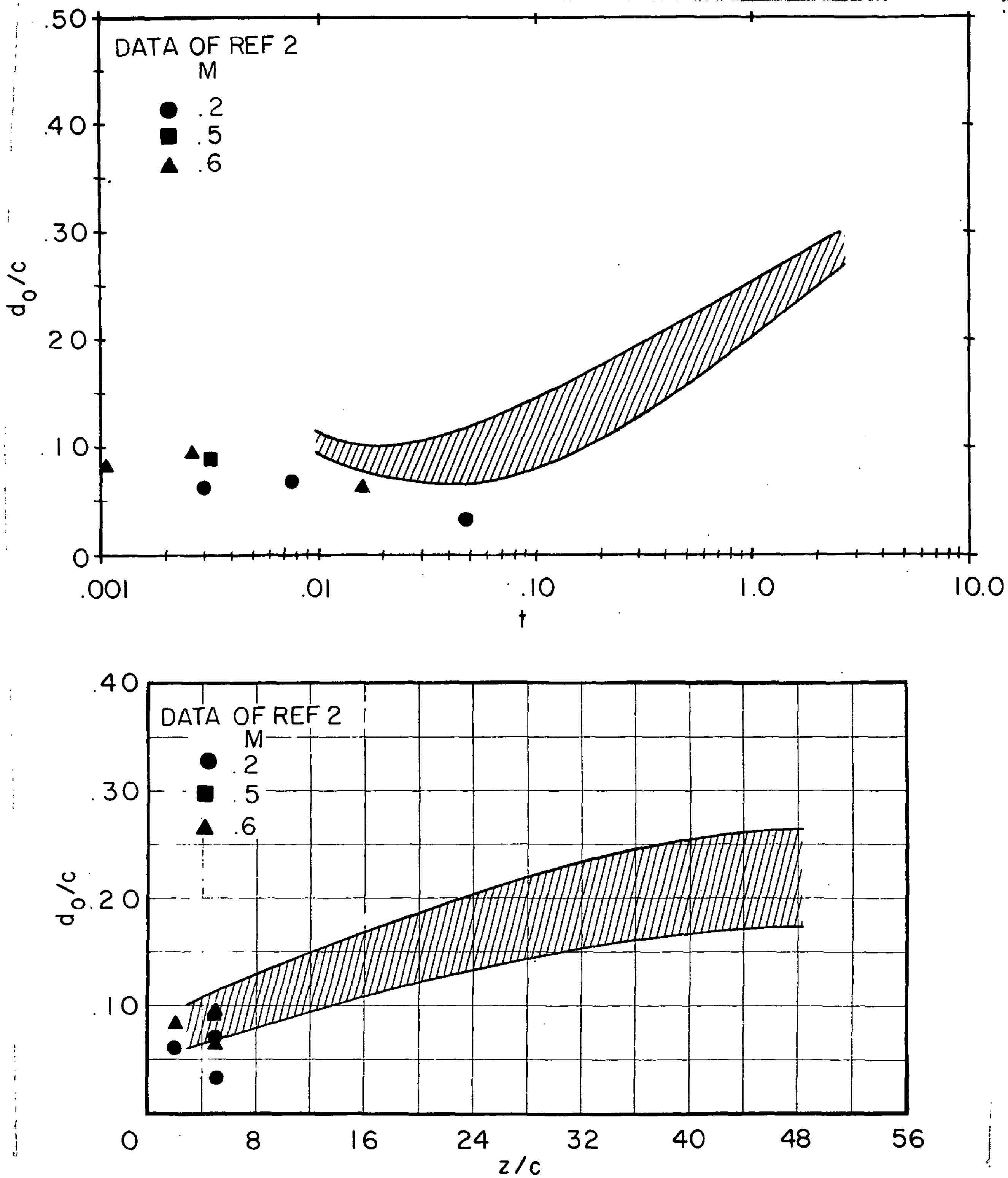

Figure 44. Vortex Core Size Comparison with Previous Results, 9^0 Revolved Tip.